Continuous Microwave Excitation of Excimer Lamps

By

Scott Bradley Hassal, B.Eng., M.Eng.

A Thesis

Submitted to the School of Graduate Studies

in Partial Fulfillment of the Requirements

for the Degree

Doctor of Philosophy

McMaster University

Continuous Microwave Excitation of Excimer Lamps

DOCTOR OF PHILOSOPHY (1991) McMASTER UNIVERSITY

(Engineering Physics) Hamilton, Ontario

TITLE: Continuous Microwave Excitation of Excimer Lamps

AUTHOR: Scott Bradley Hassal, B.Eng., M.Eng. (McMaster)

SUPERVISOR: Professor E.A. Ballik

NUMBER OF PAGES: xii, 193

Abstract

For decades, microwaves have been used to create gas discharges for many applications. This thesis deals with the use of microwaves to excite gas discharges for incoherent optical sources, with particular emphasis on excimer systems. In addition, microwave excitation of a gas laser is considered. A novel apparatus was designed and built to couple 2.45-GHz microwave radiation into a gas discharge. The microwave resonator is the essential part of this equipment, and a detailed discussion of its design and performance is given. The resonator is characterized both theoretically and experimentally in order to determine the coupling efficiency and peak electric-field strength. Specialized theory is developed in order to evaluate many parameters of a microwave-excited discharge. The phenomenon of skin effect is investigated quantitatively and expressions for the plasma frequency and electron density are developed in terms of collision frequency and observable parameters (e.g., skin depth). Expressions for peak electric-field strength, ionization coefficient and collisionless electron energy are also developed. The results of an extensive investigation of continuous-wave microwave-excited excimer fluorescence are reported. Rare-gas halide, homonuclear halogen and heteronuclear halogen systems are examined and the corresponding ultraviolet spectra are presented. Truly continuous excimer emission has been achieved (for the first time) on several transitions. For systems of particular interest (e.g. XeCl and KrCl), the effects of total pressures and gas composition on fluorescence output are investigated, and the appropriate spectra are presented. Finally, the potential operation of microwave-excited carbon dioxide and argon-ion gas lasers is investigated, and upper limits are deduced for the small-signal gain under various conditions.

Acknowledgements

Again, I express my gratitude to my supervisor, Dr. Ed Ballik, for his many helpful suggestions and ideas in the course of this research; it is truly to my benefit to have been able to work under the guidance of such a skilled experimentalist. I also am grateful to the other members of my supervisory committee, Dr. Paul Jessop and Dr. Peter Smith, for the assistance they provided.

The kind donations and loans of equipment, supplies and advice from members of the McMaster community and local tradesmen are gratefully acknowledged. The support and encouragement of my friends and relatives during the entire course of my graduate education is also appreciated.

I wish to thank the Department of Engineering Physics for the financial support it gave on my behalf in the concluding months of this research. In particular, I appreciate the efforts of Dr. Bill Garland, Mrs. Elaine Moore and Mrs. Bobbie Kartonchik in this regard.

Finally, I thank my wife, Sydney, without whose advice, assistance, companionship, compassion, counsel, encouragement, fortitude, friendship, guidance, impatience, inspiration, love, motivation, patience, resolve, support, tolerance, trust and understanding, this thesis could not have been completed.

Table of Contents

Abstract iii

Acknowledgements iv

Table of Contents v

Table of Figures vii

Table of Tables x

List of Symbols xi

Chapter 1 Introduction and Overview 1

1.1 Historical and Conceptual Overview 1

1.2 Thesis Outline 7

1.3 Thesis Objectives 10

Chapter 2 Electromagnetic and Plasma Phenomena 11

2.1 Basic Electromagnetic Theory 11

2.2 Transmission Lines 14

2.3 Waveguides 20

2.4 Microwave Resonant Cavities 24

2.5 Single Electron in a Microwave Field 30

2.6 Gaseous Breakdown at Microwave Frequencies 32

2.7 Complex Permittivity of a Plasma 34

2.8 Collisional Effects 36

Chapter 3 Experimental Apparatus 41

3.1 Practical Resonator Design 41

3.2 Cavity Q and Coupling Efficiency 46

3.3 Electrical Support Equipment 56

3.4 Vacuum and Gas-Handling System 60

3.5 General Procedure 63

Chapter 4 Characterization of a Microwave Discharge 65
4.1 Microwave Propagation in a Plasma 66
4.2 Skin Effect in a Plasma Sheath 71
4.3 Determination of Electron Density 73
4.4 Electric-Field Strength in a Plasma 74
4.5 Estimation of Electron Energy 77
4.6 Experimental 79
Chapter 5 Continuous-Wave Excimer Fluorescence 91
5.1 Introduction to Excimer Transitions 91
5.2 Experimental Overview 96
5.3 Rare-Gas Monohalide Fluorescence 100
5.4 Homonuclear Halogen Fluorescence 111
5.5 Heteronuclear Halogen Fluorescence 116
5.6 Total-Pressure Optimization 123
Chapter 6 Investigation of Gain in a Microwave Discharge 139
6.1 Microwave Resonator Design 139
6.2 Optical Resonator Design 146
6.3 The Carbon Dioxide System 151
6.4 The Argon-Ion System 152
6.5 Experimental 154
Chapter 7 Excimer Lamp Applications 163
7.1 Existing Sources of Ultraviolet Radiation 164
7.2 Medical Applications 171
7.3 Industrial Photochemistry 172
7.4 Fluorescence Diagnostics 175
7.5 Microlithography 176
Chapter 8 Conclusions and Suggestions for Further Research 181
8.1 Summary of Results 181
8.2 Suggestions for Further Research 186
References 189

Table of Figures

Figure	Description	Page
2.2-1	Equivalent circuit for lossy and lossless transmission lines.	15
2.2-2	Distributions of the magnetic (a) and electric (b) fields for a parallel-wire transmission line in a TEM mode.	19
2.2-3	Inductive (a) and short-circuit (b) terminations for a parallel-wire transmission line.	20
2.3-1	Rectangular waveguide and conventional coordinate axes with electric-field distributions.	21
2.4-1	Rectangular resonant cavity and electric-field distribution for the TE_{101} mode.	26
2.4-2	Loop (a) and probe (b) coupling of a coaxial transmission line to a resonant cavity.	28
2.4-2	Aperture coupling of a waveguide to a resonant cavity via the magnetic (c) and electric (d) fields.	29
2.4-3	Frequency response of a resonator employed as a transmission filter for various degrees of coupling.	30
2.8-1	Classical collision trajectory for an electron incident on a massive target.	38
3.1-1	Side view of the magnetron/resonator assembly constructed for the lamp investigations.	42
3.1-2	End view of the magnetron/resonator assembly.	43
3.2-1	TE_{102} resonator geometry and dimensions.	46
3.2-2	Measured two-port frequency response of the empty magnetron/resonator assembly.	49
3.2-3	Measured two-port frequency response of the magnetron/resonator assembly with a 10-mm fused-silica tube inserted.	50
3.2-4	Energy stored in a resonant cavity as a function of time.	54
3.3-1	Schematic diagram of the power supplies that are required to operate the magnetron.	58
3.4-1	Schematic diagram of the gas-handling and vacuum system for this research.	61
3.4-2	Schematic diagram of the excitation circuit that is required to operate the piezoresistive pressure transducer.	62
4.2-1	Log-log graph of plasma frequency versus collision frequency.	72
4.3-1	Log-log graph of electron density versus collision frequency.	74

4.6-1	Large-diameter discharge envelope used for microwave characterization experiments.	80
4.6-2	Microwave characterization experimental configuration.	81
4.6-3	Skin depth versus pressure for the five lightest noble gases.	82
4.6-4	Collision frequency for momentum transfer versus pressure for the five lightest noble gases.	84
4.6-5	Electron density versus pressure for the five lightest noble gases.	85
4.6-6	Ionization coefficient versus pressure for the five lightest noble gases.	86
4.6-7	Peak electric-field intensity versus pressure in the discharge.	87
4.6-8	Collisionless electron energy based on peak electric-field intensity.	88
5.1-1	Potential energy as a function of internuclear spacing.	93
5.2-1	Schematic view of the experimental apparatus used for the fluorescence investigations.	97
5.3-1	Fluorescence spectrum for a 50:50 Ar:Cl_2 mixture at a total pressure of 5 Torr.	102
5.3-2	Fluorescence spectrum for a 50:50 Ar:SF_6 mixture at a total pressure of 5 Torr.	103
5.3-3	Fluorescence spectrum for a 50:50 Kr:Br_2 mixture at a total pressure of 5 Torr.	104
5.3-4	Fluorescence spectrum for a 50:50 Kr:Cl_2 mixture at a total pressure of 5 Torr.	105
5.3-5	Fluorescence spectrum for a 50:50 Kr:SF_6 mixture at a total pressure of 5 Torr.	106
5.3-6	Fluorescence spectrum for a 50:50 Xe:I_2 mixture at a total pressure of 5 Torr.	107
5.3-7	Fluorescence spectrum for a 50:50 Xe:Br_2 mixture at a total pressure of 5 Torr.	108
5.3-8	Fluorescence spectrum for a 50:50 Xe:Cl_2 mixture at a total pressure of 5 Torr.	109
5.3-9	Fluorescence spectrum for a 50:50 Xe:SF_6 mixture at a total pressure of 5 Torr.	110
5.4-1	Fluorescence spectrum for I_2 at a total pressure of 5 Torr.	112
5.4-2	Fluorescence spectrum for Br_2 at a total pressure of 5 Torr.	113
5.4-3	Fluorescence spectrum for Cl_2 at a total pressure of 5 Torr.	114
5.4-4	Fluorescence spectrum for SF_6 at a total pressure of 5 Torr.	115
5.5-1	Fluorescence spectrum for a 50:50 I_2:Br_2 mixture at a total pressure of 5 Torr.	117

5.5-2	Fluorescence spectrum for a 50:50 I_2:Cl_2 mixture at a total pressure of 5 Torr.	118
5.5-3	Fluorescence spectrum for a 50:50 I_2:SF_6 mixture at a total pressure of 5 Torr.	119
5.5-4	Fluorescence spectrum for a 50:50 Br_2:Cl_2 mixture at a total pressure of 5 Torr.	120
5.5-5	Fluorescence spectrum for a 50:50 Br_2:SF_6 mixture at a total pressure of 5 Torr.	121
5.5-6	Fluorescence spectrum for a 50:50 Cl_2:SF_6 mixture at a total pressure of 5 Torr.	122
5.6-1	Effect of total pressure on 222-nm fluorescence intensity in a mixture of krypton and chlorine.	123
5.6-2	Fluorescence spectra for Kr:Cl_2 mixtures at their respective optimum total pressures (a) 80:20 at 50 Torr, (b) 60:40 at 30 Torr, (c) 40:60 at 10 Torr, and (d) 20:80 at 30 Torr.	125 -128
5.6-3	Effect of total pressure on 308-nm fluorescence intensity in a mixture of xenon and chlorine.	130
5.6-4	Fluorescence spectra for Xe:Cl_2 mixtures at their respective optimum total pressures (a) 80:20 at 75 Torr, (b) 60:40 at 40 Torr, (c) 40:60 at 40 Torr, and (d) 20:80 at 14 Torr.	132 -135
5.6-5	Effect of total pressure on 258-nm fluorescence intensity in chlorine.	136
5.6-6	Fluorescence spectrum for Cl_2 at a total pressure of 35 Torr.	137
6.1-1	Side view of the microwave resonator/magnetron assembly that is used for the gain investigations.	141
6.1-2	Measured two-port frequency response of the empty gain resonator/magnetron assembly.	143
6.1-3	Measured two-port frequency response of the gain resonator/magnetron assembly with a 10-mm fused silica tube inserted.	144
6.2-1	Cross-sectional view of Brewster-angle window assembly.	147
6.2-2	Schematic view of the optical resonator and TEM_{00} beam profile.	148

Table of Tables

Table	Description	Page
3.3-1	Magnetron Operational Data	6
4.6-1	Noble Gas Data	83
5.1-1	Rare Gas and Halogen Transition Wavelengths	94
5.2-1	Data for Recording Spectra	99
6.5-1	Optical Resonator Data	155
6.5-2	Beam Parameters: Carbon Dioxide System	156
6.5-3	Gain Investigation Results: Carbon Dioxide System	158
6.5-4	Beam Parameters: Argon-Ion System	160
6.5-5	Gain Investigation Results: Argon-Ion System	161

List of Symbols

A	electron displacement amplitude
a(t)	acceleration as a function of time
a	rectangular waveguide width
b	rectangular waveguide height
C	distributed capacitance per unit length, capacitance, mirror radius of curvature
c	speed of light in vacuum, microwave resonator length
D	round-trip diffraction losses
d	circular waveguide diameter
e	elementary charge
$\vec{E}(\vec{r},t)$	electric field intensity
F	scalar force
FWHM	full-width at half-maximum
G	distributed conductance per unit length,
$\vec{H}(\vec{r},t)$	magnetic field strength
j	imaginary unity ($\sqrt{-1}$)
$\vec{J}$	total current density
$\vec{J}_c$	convection current density
$\vec{J}_d$	displacement current density
k	complex wavenumber
$\vec{k}$	wavevector
k_g	imaginary wavenumber of a waveguide below cutoff
L	distributed inductance per unit length, optical resonator length
l	active discharge length
$\bar{l}$	mean free path
l_{min}	minimum resolvable feature width
m	mass
N	number particle density, complex refractive index
NA	numerical aperture
N_f	Fresnel number
P	power
p	power density
q	collision cross-section for momentum transfer
$q_\Omega(\nu,\theta)$	differential scattering cross-section
q_s	scattering cross-section

R	distributed resistance per unit length, resistance mirror reflectance (intensity)
s(t)	displacement as a function of time
U	kinetic energy
u_{ion}	ionization energy
v_p	phase velocity
v(t)	speed as a function of time
V	volume
VLSI	very large scale integration
VSWR	voltage standing wave ratio
W	stored energy in a resonator
Z_0	characteristic impedance
Z_l	load impedance
Δz	depth of focus
Γ_p	reflection coefficient at point p
ε	effective electrical permittivity
ε_0	electrical permittivity in vacuum
ε_r	relative electrical permittivity
λ	free-space (optical or microwave) wavelength
λ_{co}	cut-off wavelength
λ_g	waveguide wavelength
μ	effective magnetic permeability
μ_0	magnetic permeability in vacuum
μ_r	relative magnetic permeability
ν	collision frequency for momentum transfer
ν_s	collision frequency for scattering
η	wave impedance
η_0	wave impedance in vacuum
ρ	spatial charge density
σ	electrical conductivity
τ	time interval, energy lifetime
τ'_{00}	first root of the derivative of the zero-order Bessel function
ω	angular frequency
ω_{co}	angular cutoff frequency
ω_p	plasma frequency
$d\Omega$	differential solid angle

Chapter 1

Introduction and Overview

In this chapter, microwave discharge excitation is compared and contrasted with some of the more common methods of exciting gas discharges. In doing so, a brief discussion of the development of the existing techniques is given in order to give a conceptual overview and provide some historical perspective. This chapter concludes with a concise statement of the objectives of the author in pursuing this research.

1.1 Historical and Conceptual Overview

There are many ways of pumping (i.e., transferring energy to) an ionized gas or plasma. Chemical reactions, relativistic beams of electrons (or other charged particles), intense optical radiation and electric discharges have all been used to excite a gas discharge. Of these techniques, electric discharges are most commonly used to provide plasma excitation.

The common phenomenon in all electric discharge schemes is that energy is transferred to the gas via electronic collisions, and the electrons acquire energy from an electric field that is present within the gas. This is not entirely the case for e-beam pumping, since the electron energy is kinetic and does not arise from an internal field. Note that optical pumping should not be considered a discharge process since the photons are absorbed directly by the plasma (i.e., it is an intrinsically quantum effect).

Electrical discharges can be broadly classified (albeit imprecisely) as direct current (DC) or radio frequency (RF). A DC discharge can be continuous or pulsed. In the latter case, "DC" is often a misnomer. If the pulses are short enough, a significant portion of the energy can be in the high-frequency Fourier components that are associated with any short-duration event. As an example, a discharge-pumped excimer laser may have a current risetime faster than 5 ns, meaning that frequency components in excess of 200 MHz are produced.

The high-frequency extreme of RF pumping is termed microwave pumping. A useful conceptual difference between RF- and microwave-excited discharges is the importance of wall collisions versus collisions within the gas. As is shown in Chapter 2, a free electron in an alternating field undergoes simple harmonic motion with a displacement amplitude that varies inversely as the square of the frequency. Clearly, if the total displacement of a single electron is on the order of, or less than, the dimensions of the plasma container, the importance of electron-atom collisions in a real ionized gas is greater than that of electron-wall collisions. A discharge operating within this regime is called a microwave discharge; the term RF discharge is applied to a system in which the single-electron amplitude is significantly greater than the size of the discharge container. Under typical laboratory conditions, the threshold frequency between these two regimes occurs somewhere between a few hundred megaHertz and 1 GHz.

This frequency threshold has an immediate practical consequence. In the case of a microwave discharge, the wavelength of the applied field is on the order of the dimension of the discharge vessel. By creating a transmission-line or waveguide resonator, electric fields may be created that are large enough to excite a gas sample that is enclosed (in a dielectric envelope) within the resonator. This situation can be contrasted to a conventional RF discharge, in which the power is capacitively or inductively coupled to the gas at medium to high frequencies (i.e., from 300 kHz to 30 MHz). In the microwave case, the plasma forms a distributed load within the resonant cavity. In the RF case, the applied wavelength is much longer than the discharge tube, and the components of the apparatus (i.e., discharge, work coil or capacitor plates, etc.) form a lumped-element resonant circuit.

The excitation of gas discharges using microwaves dates back to the invention of radar in World War II. Transmit-receive (TR) tubes were filled with a low-pressure inert gas and positioned between the receiver and the rest of the radar system. The high-power transmitted pulse created a highly reflective discharge within the tube, protecting the delicate receiver. After the discharge extinguished, the receiver was automatically reconnected to the antenna to intercept the return pulse. This method allows a radar unit to be operated with a single antenna.

In the years following World War II, microwave-excited gas discharges were used as incoherent optical sources for both discrete atomic lines and continuous broadband radiation. Intense broadband emission in the ultraviolet and vacuum ultraviolet from krypton and xenon microwave discharges was reported by Wilkinson and Tanaka (1955) and by Wilkinson (1955), respectively.

Shortly after the first operation of a gas laser, the flurry of research activity included a few investigations into using microwave-excited gas discharges to obtain optical gain and oscillation. The first successful operation of a microwave-pumped gas laser was reported

by Ahmed and Kocher (1964). These investigators successfully operated a microwave-excited helium-neon laser. The use of an externally applied DC magnetic field to create cyclotron resonance was an integral part of their technique. Shortly after these reports, microwave discharges were used by various investigators (Goldsborough, 1966; Paik and Creedon, 1968) to pump argon-ion lasers. These first studies were soon abandoned in favour of simpler excitation techniques, notably the use of DC discharges. As laser research progressed over the following three decades, microwave excitation was pursued only sporadically. The practical complexities and expense of a microwave source and the precautions that are required to control microwave leakage were all significant disadvantages.

The broad motivation for this research was to develop viable methods of exciting gas lasers using microwaves. The use of microwaves offers many theoretical and practical advantages over other excitation techniques. The most important of these is the lack of electrodes inside the plasma tube. In fact, the use of microwave excitation allows all reactive materials to be located away from direct contact with the plasma, alleviating problems such as gas clean-up and contamination. Other problems inherent to a DC discharge include electrophoresis and cataphoresis. The former effect results in a pressure gradient between the cathode and anode due to the pumping of ions by the electric field. The latter effect is the separation of the different gas species within the discharge. Both effects interfere with efficient operation of a mixed-gas laser. Electrophoresis and cataphoresis do not occur in RF or microwave discharges because the periodic reversal of the electric field prevents significant pressure or concentration gradients from forming.

In addition to the systems already mentioned, several other laser systems have been operated recently, both continuous wave (CW) and pulsed, using a microwave-excited discharge as the active medium. Specifically, a fast axial-flow CW CO_2 laser with 1-kW output power has been recently demonstrated by Freisinger *et al* (1989), and Christensen and Waynant have investigated various pulsed rare-gas halide excimer lasers (1982, 1985),

as have Wisoff and Young (1982, 1984). In addition, extremely intense microwave pumping from relativistic magnetrons has produced laser action in many different gas and vapour mixtures (Brandelik and Smith, 1980; Kravchenko *et al*, 1984; Vaulin *et al*, 1988, 1989).

Quite recently, a new class of lamp was reported in the literature by Kumagai and Obara (June, July and October 1989). This type of lamp emitted intense radiation via quasi-CW rare-gas halide fluorescence from a microwave discharge. The initial reports cited pulse durations in excess of 8 ms and efficiencies of several percent, using ArF and KrF systems. Because of the exciting implications and prospects of these systems, the emphasis of this research was focussed to expand upon these developments.

Even before these reports of quasi-CW excimer fluorescence, microwave-excitation techniques enjoyed limited use in electrodeless discharge lamp (EDL) systems. Investigators have used EDLs as sources of visible, ultraviolet (UV) and vacuum-ultraviolet (VUV) radiation for chemical and physical studies for some time (Dagnall and West, 1968; Kikuchi, 1971; Busch and Vickers, 1973; Haarsma *et al*, 1974). As is the case for gas lasers, microwave excitation also offers several advantages over DC and low-frequency RF techniques for gas-discharge devices in general. Higher average electron energies and a greater degree of ionization and dissociation are attainable in microwave discharges, allowing efficient excitation of highly energetic transitions. In addition, uniform CW volume discharges can be supported at much higher pressures than with other techniques. However, the principle advantage of microwave techniques over conventional techniques is still the elimination of internal metal electrodes from the discharge environment. In conventional gas-discharge devices, chemical and physical processes involving the gas fill and the electrodes degrade both long- and short-term performance. Of course there are disadvantages associated with microwave excitation, but the benefits outweigh these disadvantages for many applications.

High cost, the principle disadvantage that plagued the early popularity of microwave-excitation techniques, has largely been eliminated by the emergence of the household microwave oven. Microwave oscillators used to be prohibitively expensive and complex, but this is certainly no longer the case. For this research, the author purchased a 2.45-GHz oscillator and power supply, which was capable of delivering nearly 2-kW peak power in 8-ms pulses, with an average power in excess of 500 W. The oscillator is a robust, air-cooled magnetron that operates satisfactorily with the crude power source that was supplied. The retail cost of this equipment was less than CDN$ 100.

The problems of microwave leakage can be controlled by sensible design of the microwave components of the system. It is usually most efficient to make all resonant and transmission structures closed so that there is no need for external EMI shielding. In particular, extensive use of waveguides operating below cutoff can allow visual and physical access to internal regions of the apparatus. In situations where only visual access is required, perforated walls permit a clear view with no significant leakage.

The first rare-gas halide lasers were reported in 1975 (Searles and Hart; Brau and Ewing; Ault *et al*; Ewing and Brau; Mangano and Jacob) and since that time there has been a tremendous effort to investigate and understand the dynamics of these complicated systems. Much of this effort was as a result of the interest in developing high-power pulsed UV lasers for use in inertial confinement fusion research, and the fact that there are not many other known laser systems that operate "efficiently" in the UV. Until recently, however, there had been no report of CW laser action or even CW fluorescence of any of these species, in spite of the considerable attention that this problem has received. The principle reason for this is that the rare-gas halide lasers operate at total pressures of several atmospheres, and electrical discharges are unstable at these pressures.

This instability confines such lasers to operation in a pulsed regime, since at high pressures a filament or streamer discharge can replace volume discharge within nanoseconds of breakdown. Such a streamer results in grossly non-uniform excitation of the gas, preventing the laser from oscillating. Qualitatively, streamer formation occurs more readily at higher gas pressures. This is due to the shorter mean free path for the electrons within the discharge. As the mean free path is decreased, the electrons are effectively confined to a channel, which extends approximately parallel to the electric field. One complication in this simple description is the emission of high-energy photons by the streamer that ionize the gas in front of the developing channel. The effect of this ionization is the production of a jagged filament that is typical of such a discharge (e.g., atmospheric lightening). Such a filament is useless for creating a uniform population inversion within the mode volume of the laser, thus this operation regime must be avoided.

The author has demonstrated CW excimer fluorescence on many transitions in rare-gas halide and homonuclear halogen systems at relatively low pressures (i.e., from 1 Torr to 400 Torr). At the higher pressures in this range, the volume discharge is replaced by a filamentary discharge. Unlike the case of a laser, operation in this regime is not critical for an incoherent source, such as a lamp. In addition to providing valuable information about excimer dynamics, these systems potentially have many practical applications as efficient and narrow-band sources UV and VUV radiation.

1.2 Thesis Outline

A concise treatment of the pertinent theory follows this introductory chapter. Chapter 2 deals with fundamental concepts that are relevant to electromagnetic theory and plasma physics. In order to provide perspective to the reader, theory is developed from first principles wherever possible. In doing so, special cases are examined to allow the reader

to develop an intuitive feeling for the material. Starting with a review of basic electromagnetic theory, the author provides a brief overview of passive microwave components (i.e., transmission lines, waveguides and resonators). A qualitative discussion of microwave breakdown of gases is given. The complex permittivity of a plasma is derived. The chapter concludes with a brief discussion of collisional effects in a gas discharge.

Chapter 3 is primarily a description of the experimental apparatus that was designed and constructed to perform this research. The microwave resonator is the most important part of this equipment, and a detailed discussion of its design and performance is given. The resonator is characterized both theoretically and experimentally in order to determine the coupling efficiency and peak electric-field strength. A description of the electrical support equipment (e.g., power supplies) is given; particular emphasis is given to the description of equipment that was designed and constructed by the author. The gas-handling and vacuum system is also described. The chapter concludes with an overview of the general procedure for each of the three types of experiments performed: discharge characterization, recording spectra and the investigation of gain.

In Chapter 4, the results of the previous chapters are used to develop specialized theory to allow the characterization of many parameters of a microwave discharge. Microwave propagation through an isotropic, linear, homogeneous plasma is examined. An expression for the complex wavenumber of the plasma is derived. Using this expression, cutoff conditions are examined for a number of different conditions. The phenomenon of skin effect is investigated quantitatively and an expression for the plasma frequency is developed in terms of the collision frequency for momentum transfer and observable parameters (i.e., skin depth). An expression for electron density is also found using the same parameters. These calculations are extended to find an expression for the peak electric-field strength within the plasma that is in terms of quantities that are either known

or can be reasonably estimated. Furthermore, the difficulties associated with making a rigorous calculation of electron energies are shown, and an estimate of these energies is made.

Chapter 5 introduces some fundamental concepts for excimer (i.e., excited dimer or excited complex) chemistry and physics. The results of an extensive investigation of continuous-wave microwave-excited excimer fluorescence are reported. Rare-gas halide, homonuclear halogen and heteronuclear halogen systems are examined. The effects of total pressures and gas composition on fluorescence output are investigated for the more promising systems, and the appropriate spectra are presented.

Chapter 6 describes investigations of the operation of a gas laser using a microwave-excited discharge as the gain medium. These investigations required a different resonator from the lamp studies. In order to achieve sufficient round-trip gain for laser oscillation, it is necessary to uniformly excite a long volume of gas. Although laser operation was not achieved, upper limits are deduced for the small-signal gain under various conditions. This aspect of the research still holds great promise for future developments.

Chapter 7 describes a few of the potential applications for microwave-pumped excimer lamps. An overview of existing sources of ultraviolet and vacuum-ultraviolet radiation is given, with an emphasis on those that are currently most commonly used. Next, the applications of UV and VUV radiation are discussed for a number of diverse fields. Medical applications (e.g., phototherapy and photochemotherapy) are outlined, as are industrial applications. Fluorescence diagnostic applications are also discussed, emphasizing possible forensic uses. Finally, the potential of the microwave-pumped excimer lamp for use in deep-UV microlithography is assessed.

Chapter 8 summarizes this research and draws some general conclusions. In addition, suggestions for improvements and extensions to this research are made.

1.3 Thesis Objectives

This research has four main objectives:

1) *To investigate and develop novel ways of coupling microwave power to a gas discharge so as to produce extractable optical power.*

Closed resonant structures are of the most interest in order to control microwave leakage. Characterization of the final design(s) is also required.

2) *To characterize a microwave-excited gas discharge in terms of observable parameters.*

In order to be of practical use, characterization must be in terms of parameters that are either directly observable or readily calculable. In cases in which these conditions are not fulfilled but a reasonable estimate can be made, the characterization may be made based on the estimated parameters.

3) *To investigate continuous-wave excimer fluorescence from microwave-excited gas mixtures that contain halogens and rare gases.*

Three distinct types of excimer transitions are of interest: rare-gas halide, homonuclear halogen, and heteronuclear halogen.

4) *To investigate the possibility of pumping a gas laser with microwaves.* Although laser operation was not reproducibly demonstrated during this research, experiments into the creation of a microwave-pumped gas laser allow upper limits on gain in a microwave discharge to be deduced. The carbon dioxide and argon-ion systems are of particular interest.

Chapter 2

Electromagnetic and Plasma Phenomena

This chapter presents some of the concepts that are required to explain the electromagnetic and plasma-physics aspects of this research. Basic relationships are derived for the convenience of the reader, and an overview of fundamental ideas is given. Where appropriate, specific theory (which is often difficult or impossible to find elsewhere) is developed. The coverage provided by this chapter is necessarily brief. Where possible, references that give a clear and comprehensive treatment of these subjects are given. In particular, the texts by Brown *et al* (1973) and Reintjes and Coate (1952) are good references for microwave engineering. It should be noted that the discussion of transmission lines given here is similar to that given previously by the author (Hassal, 1988).

2.1 Basic Electromagnetic Theory

The mathematical description of the propagation of microwaves is identical to that of an electromagnetic disturbance of any frequency. In the following development, it is

assumed that the medium is homogeneous, linear and isotropic. For a concise treatment of basic electromagnetic theory, see Edminster (1979).

The magnetic- and electric-field distributions must satisfy Maxwell's equations, namely

$$\nabla \cdot \vec{D} = \rho, \qquad (2.1-1a)$$

$$\nabla \cdot \vec{B} = 0, \qquad (2.1-1b)$$

$$\nabla \times \vec{E} = -\frac{\partial \vec{B}}{\partial t}, \qquad (2.1-1c)$$

$$\nabla \times \vec{H} = \frac{\partial \vec{D}}{\partial t} + \vec{J}_c, \qquad (2.1-1d)$$

with the constitutive equations

$$\vec{D} = \varepsilon_0 \varepsilon_r \vec{E}, \qquad (2.1-2a)$$

$$\vec{B} = \mu_0 \mu_r \vec{H}, \qquad (2.1-2b)$$

and

$$\vec{J}_c = \sigma \vec{E}. \qquad (2.1-2c)$$

As usual, $\vec{E}(\vec{r},t)$ is the electric-field intensity,

$\vec{H}(\vec{r},t)$ is the magnetic-field strength,

ρ is the spatial charge density,

$\vec{J}_c$ is the conduction current density,

σ is the conductivity,

ε_0, μ_0 are the permittivity and permeability in vacuum,

ε_r, μ_r are the relative permittivity and permeability.

For convenience, the electric permittivity and magnetic permeability are defined by $\varepsilon = \varepsilon_0 \varepsilon_r, \mu = \mu_0 \mu_r$.

In charge-free, current-free space, Maxwell's equations are simplified because $\rho = 0$ and $\sigma = 0 \Rightarrow \vec{J}_c = \vec{0}$. In addition, $\varepsilon_r = \mu_r = 1$ in vacuum.

Now assume only that the conduction current is zero. By manipulating Eqs. 2.1-1c and 2.1-1d one obtains

$$\nabla^2 \vec{E} - \varepsilon\mu \frac{\partial^2 \vec{E}}{\partial t^2} = 0, \qquad (2.1-3a)$$

and

$$\nabla^2 \vec{H} - \varepsilon\mu \frac{\partial^2 \vec{H}}{\partial t^2} = 0, \qquad (2.1-3b)$$

which are the wave equations for the electric and magnetic fields. Thus field distributions of the form

$$\vec{E}(\vec{r}, t) = f\left(t \pm \frac{\vec{k} \cdot \vec{r}}{\omega}\right), \qquad (2.1-4a)$$

and

$$\vec{H}(\vec{r}, t) = g\left(t \pm \frac{\vec{k} \cdot \vec{r}}{\omega}\right), \qquad (2.1-4b)$$

with $f()$, $g()$ as arbitrary functions,

$\vec{k}$ as the wavevector, and

ω as the angular frequency,

are solutions corresponding to plane waves. In general, any solution to the wave equations can be expressed as a linear superposition of plane waves. This approach can be particularly useful in analyzing low-order TE modes in rectangular waveguides or rectangular resonant cavities.

Using the above relationships, one can show that the phase velocity of the wave is given by

$$v_p = \frac{\omega}{k} = \frac{1}{\sqrt{\varepsilon\mu}} = \frac{c}{\sqrt{\varepsilon_r \mu_r}}, \qquad (2.1-5)$$

where $c = \frac{1}{\sqrt{\mu_0 \varepsilon_0}} = 3.00 \cdot 10^8 m/s$ is the speed of light in vacuum, and $k \equiv |\vec{k}|$.

Also, one can define the wave impedance by

$$\eta = \frac{|\vec{E}|}{|\vec{H}|} = \sqrt{\frac{\mu}{\varepsilon}} = \sqrt{\frac{\mu_r}{\varepsilon_r}}\eta_0, \qquad (2.1-6)$$

where the value

$$\eta_0 = \left(\frac{\mu_0}{\varepsilon_0}\right)^{\frac{1}{2}} = 377\Omega \qquad (2.1-7)$$

is the wave impedance in vacuum. Note that although the wave impedance is directly analogous to the usual concept of impedance from circuit theory and has units of Ohms, it is not a ratio of voltage to current.

2.2 Transmission Lines

If the wavelength of an electrical signal is much larger than the dimensions of the circuit through which it propagates, then it is possible to analyze that circuit by modeling it as a collection of discrete (or lumped-element) components that are interconnected by perfect conducting paths. Such an approximation is valid even at relatively high frequencies. For example, an FM radio broadcast has a nominal carrier frequency of 100 MHz, which corresponds to a 30-m wavelength. Of course, the assembled circuitry for a receiver is usually no larger than 0.1 m, and so the use of this elementary theory is well justified.

As the operating frequency of a circuit increases, the wavelength of the signal will begin to approach the size of the components themselves. For example, at a frequency of 2.45 GHz, the vacuum wavelength is only 12.2 cm. If the components are of comparable size, the lumped-element circuit model will predict erroneous results, and a more general approach is required. A proper application of Maxwell's equations will solve any circuit, regardless of frequency. However, in cases where a few specific assumptions are valid, transmission-line theory is a valuable compromise as it allows an accurate, concise analysis to be made. Interestingly enough, this powerful theory is most easily derived from the localized-component circuit theory it is intended to supplement.

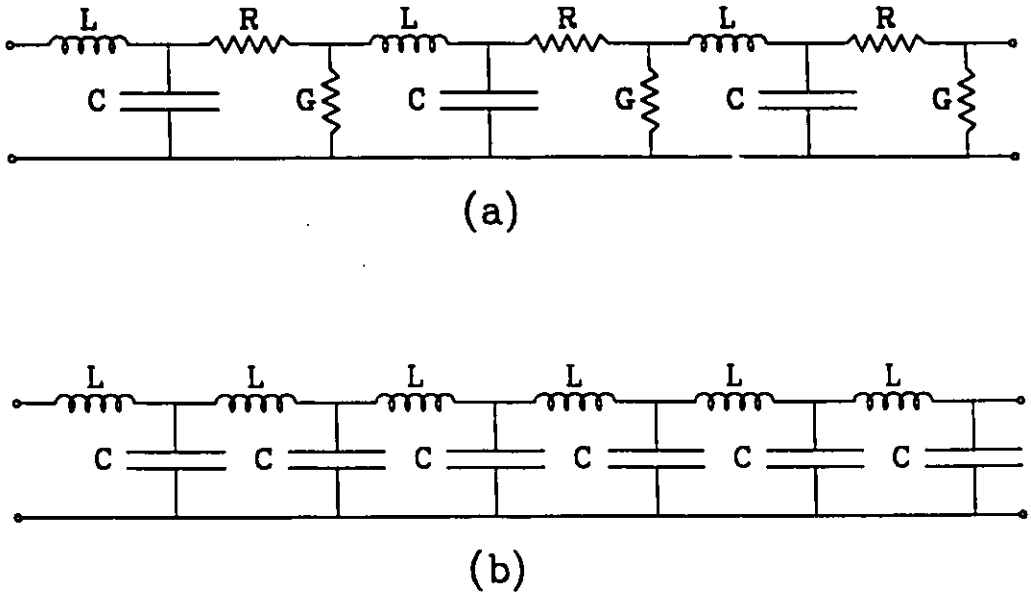

Figure 2.2-1 Equivalent circuit for lossy (a) and lossless (b) transmission lines. The parameters indicate the distributed values for shunt capacitance (C), series inductance (L), shunt conductance (G), and series resistance (R). The units for these are F/m, H/m, S/m, and Ω/m, respectively.

An ideal transmission line consists of two or more infinitely long conductors, arranged such that the cross-section of the configuration does not vary along its length. In practice, it is sufficient that the length of the line is much greater than the spacing of the conductors. A transmission line is lossless if it is incapable of converting electric power to heat (i.e., composed of zero-loss dielectric, and zero-resistance conductors). In many practical situations, these criteria are well approximated.

Figure 2.2-1 shows an equivalent-circuit representation of a short portion of both a lossy and lossless transmission line. The circuit components in this figure are not localized, but represent values that are distributed uniformly along the length of the line; therefore all of the parameters have units that are explicitly per unit length. Consider the specific example of two parallel wires. If the transmission line is lossless, there is a distributed shunt capacitance (C) between the two wires and a distributed series inductance (L) along their length. In the lossy case, the heat dissipation along the line is accounted for by the shunt conductance (G) and the distributed series resistance (R). A further criterion for an ideal line is that each of these parameters remain independent of frequency. For the present, the lines will be considered to be lossless (i.e., R = 0 and G = 0), since including the parasitic resistances and leakage conductances in an analysis constitutes an unjustified complication at this point.

By considering an infinitesimal length of the line, it can be shown that a signal on that line propagates with speed v, with a voltage V and corresponding current I, having a constant ratio Z_0 along the line. The parameters v and Z_0 are given by

$$v = \frac{1}{\sqrt{LC}} \qquad (2.2-1)$$

and

$$Z_0 \equiv \frac{V}{I} = \left(\frac{L}{C}\right)^{\frac{1}{2}}. \qquad (2.2-2)$$

Here, Z_0 is termed the characteristic impedance of the line (for the lossless case, a characteristic resistance R_0 is sometimes used). The physical meaning of this parameter is similar to what one might expect based on lumped-element theory. There is no phase shift between V and I, yet the line is lossless and so Z_0 cannot be resistive in nature. To resolve this apparent dilemma, it is necessary to recall that the line is considered to be infinite. The power flow into the line is real, and the energy is stored (as a propagating wave) in the line. In practice, a low-loss line can appear to be infinite only if it is terminated with a matched load to suppress reflections. If a line of finite length is terminated with a purely inductive or capacitive load, then the voltage and current for the line will be out of phase in the steady-state case. It is helpful to introduce another parameter, the voltage reflection coefficient at an arbitrary point p,

$$\Gamma_p \equiv \frac{V_{reflected}}{V_{incident}}. \qquad (2.2-3)$$

If a line is connected to a component (i.e., load) with an impedance Z_l, it can be shown that

$$\Gamma_p \equiv \Gamma_l = \frac{(Z_l - Z_0)}{(Z_l + Z_0)}. \qquad (2.2-4)$$

Note that, $-1 \leq |\Gamma_p| \leq 1$ and that the equalities hold when Z_l is zero or infinite, respectively.

A useful empirical parameter is the voltage standing wave ratio, or VSWR, which is defined as the ratio of the maximum peak voltage on a line to the peak voltage a quarter-wavelength away. It is elementary to show that this quantity is related to the reflection coefficient by

$$VSWR = \frac{1 + |\Gamma|}{1 - |\Gamma|}. \qquad (2.2-5)$$

The VSWR can be measured conveniently using a slotted section of transmission line. By equipping a movable carriage with a small probe, a signal that is proportional to voltage can be obtained as a function of position. Using this technique, the ratio of incident to reflected power can be calculated. The amount of power absorbed by the load can then be found easily. It is usually reasonable to neglect the losses in the slotted section of line, and to assume that the probe provides insignificant loading.

As a final note, it is possible to analyze a transmission line from a field perspective. Referring to Fig. 2.2-2, it is clear that both the electric and magnetic fields are transverse to the direction of propagation. Such a propagation mode is termed TEM. Performing a quantitative analysis is unjustified here, but it should be noted that the field approach is intrinsically more complete than the transmission-line theory set out above. As an example, consider a parallel-wire transmission line that is terminated with what appears to be a dead short (Fig. 2.2-3a). Experiments (and field theory) would demonstrate that this short is actually inductive. A true short circuit on this line would have to be formed with a transverse conducting plane, as shown in Fig. 2.2-3b. Considering that a transmission line operates in a TEM regime, it is intuitively apparent from field theory that high-frequency plane waves would be better reflected by the indicated plane, and that the simple bar would be inductive. This example is especially important for a practical coaxial transmission line. With the outer conductor completely containing the fields (assuming infinite conductivity), an annular plane forms a perfect short circuit. In the case of the parallel-wire transmission line, the conducting plane would have to be infinite in order to achieve the same effect.

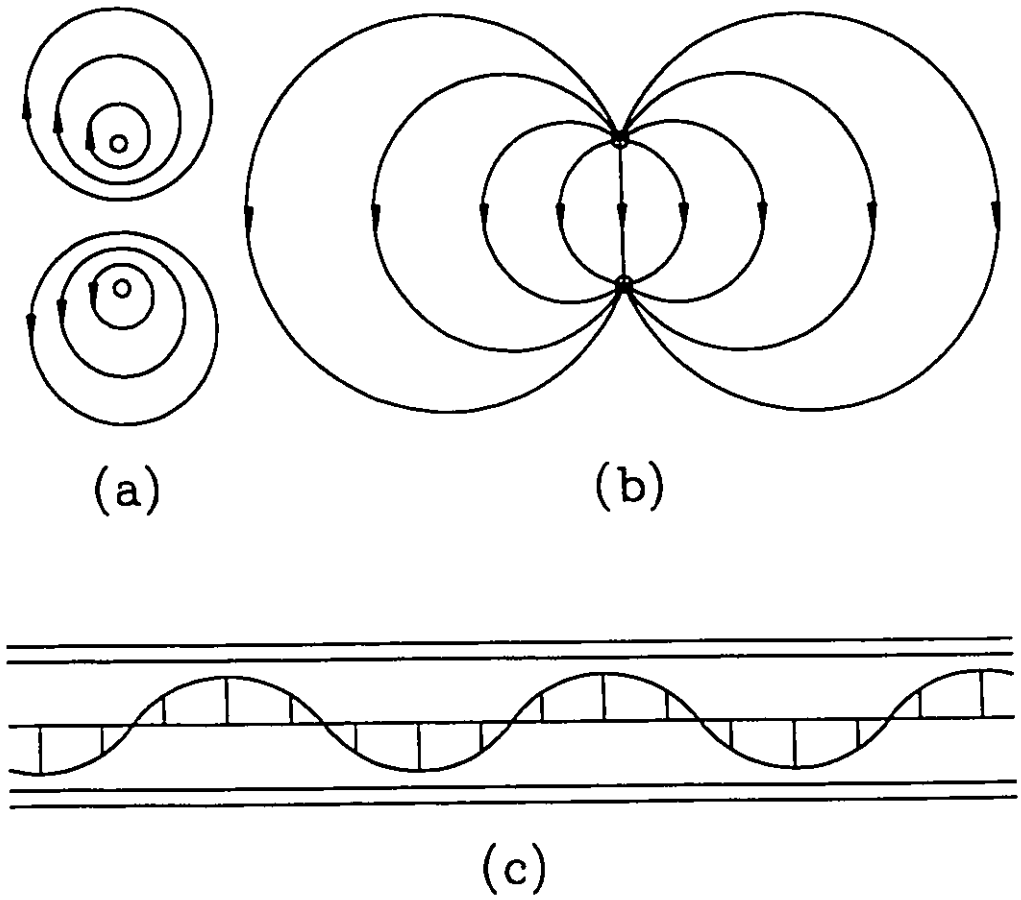

Figure 2.2-2 Distributions of the magnetic (a) and electric (b) field for a parallel-wire transmission line in a TEM mode. Note that the fields and propagation direction are all mutually perpendicular. The variation of field strength along the length of the line is also indicated (c).

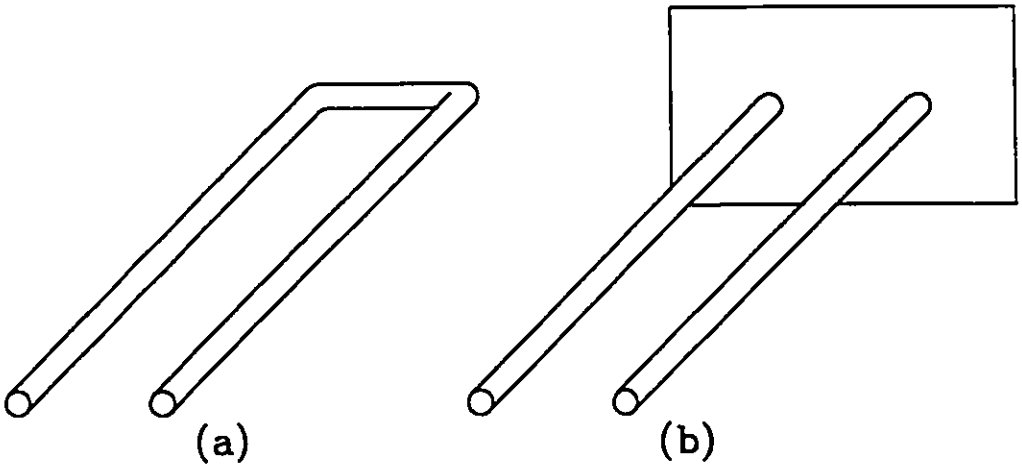

Figure 2.2-3 Inductive (a) and short-circuit (b) terminations for a parallel-wire transmission line. Although a casual application of simple circuit theory might suggest that (a) is also a short for all frequencies, it is obvious from wave theory that this is not so.

2.3 Waveguides

An ideal waveguide consists of a (usually) single hollow conductor of constant cross section. The hollow portion of the waveguide is filled with a lossless dielectric. The cross section can be of arbitrary shape, but in practice it is most often circular or rectangular. The analysis for either is quite involved, and so the method of solution will only be summarized in order to emphasize the salient points, and only the needed results will be stated here. For a good general analysis of waveguides, the reader is referred to the text by Brown *et al* (1973) or that by Reintjes and Coate (1952).

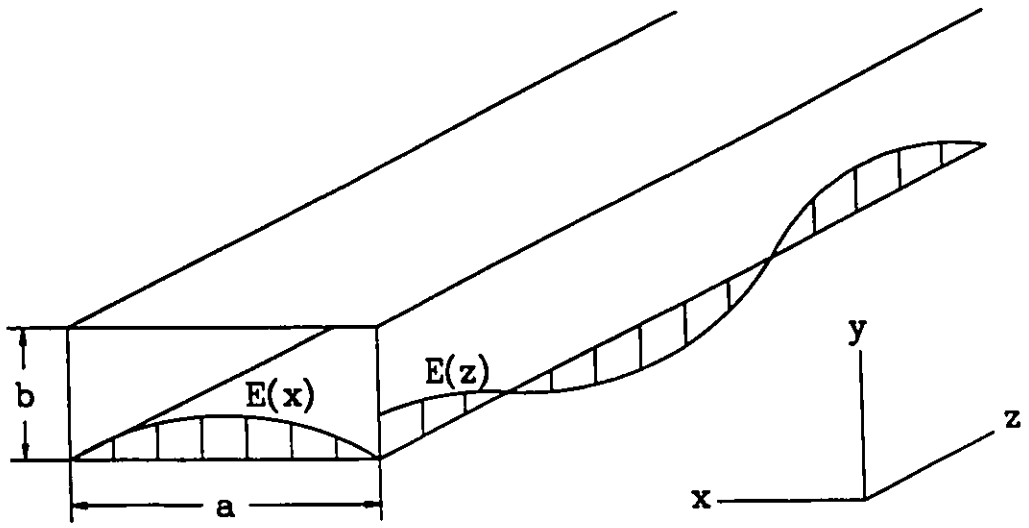

Figure 2.3-1 Rectangular waveguide and conventional coordinate axes with electric-field distributions. Although in the figure the distribution E(z) is indicated as a projection on the side wall, its position is really on the centerline that is parallel to the z axis.

Figure 2.3-1 shows a rectangular waveguide of width a and height b along with the conventional coordinate axes. The usual method for analyzing a waveguide is to assume a sinusoidal solution along the z axis, and then to solve Maxwell's equations using the resulting boundary conditions. These boundary conditions require that the electric field must be normal to the conductor, and that the magnetic lines of flux must not penetrate the conductor. The first condition is necessary if infinite currents in the conductor are to be prevented, the second results from the required continuity of the magnetic flux lines. In the cases of plane waves in free space or waves on transmission lines, both the electric and magnetic fields are perpendicular to the direction of propagation. This propagation mode is termed TEM (Transverse Electric Magnetic). However in the case of guided waves, either

the electric field or the magnetic field must have a non-zero component in the z direction, in order to satisfy these conditions and the equations. These modes are termed TM and TE, respectively.

Unlike the TEM case, TE and TM waves cannot propagate below a certain frequency (called the cutoff frequency), which is a function of the shape and electrical size of the waveguide cross-section. The lowest-order or dominant mode is that having the lowest cutoff frequency. Waveguides are usually designed so that the only method of wave propagation is via the dominant mode. For a rectangular waveguide of width a, the dominant mode is TE_{10}. The indices refer to the number of half-cycle variations in the electric field from wall to wall in the x and y directions, respectively. The electric field distribution for this case is also shown in Fig. 2.3-1. In the following, λ_g refers to the effective wavelength within the waveguide (i.e., in the direction of propagation), a parameter which is always greater than the TEM "free-space" wavelength λ (i.e., the wavelength of a plane wave propagating through the dielectric that fills the waveguide). For a rectangular waveguide, the cutoff condition is given by

$$\lambda < \lambda_{co} \equiv 2a, \tag{2.3-1}$$

where λ_{co} is called the cutoff wavelength.

The waveguide wavelength can be expressed as

$$\lambda_g = \frac{v_p}{f} = \frac{\lambda}{\sqrt{1-(\omega_{co}/\omega)^2}}, \tag{2.3-2}$$

where the angular cutoff frequency is given by

$$\omega_{co} = c\frac{\pi}{a} = 2\pi\frac{c}{\lambda_{co}}. \tag{2.3-3}$$

A very useful equation can be obtained by rearranging the above expressions to give

$$\frac{1}{\lambda_g^2}=\frac{1}{\lambda^2}-\frac{1}{\lambda_{co}^2}. \qquad (2.3-4)$$

In this last relationship, note that the cutoff and waveguide wavelengths are interchangeable.

For the TE_{10} mode in a rectangular waveguide, the electric and magnetic field distributions are given by

$$\vec{E}(x,y,z,t)=E_0\sin\left(\frac{\pi x}{a}\right)\hat{y}\exp j(\omega t-k_g z) \qquad (2.3-5a)$$

and

$$\vec{H}(x,y,z,t)=H_0\left(\sin\left(\frac{\pi z}{a}\right)\hat{x}+\cos\left(\frac{\pi x}{a}\right)\hat{z}\right)\exp j(\omega t-k_g z), \qquad (2.3-5b)$$

where $k_g \equiv 2\pi/\lambda_g$. Note that there is no dependence on the waveguide height, b, in any of these expressions. In most practical cases the height is close to half the width. Increasing the height relaxes the cutoff conditions for the unwanted higher-order modes, whereas decreasing the height lowers the power-handling capability of the waveguide because the cross-sectional area is reduced.

The relationship between the electric- and magnetic-field amplitudes is given by the characteristic impedance of the waveguide. For TE modes,

$$Z_0 \equiv \left|\frac{E_0}{H_0}\right| = \frac{\eta}{\sqrt{1-(\omega_{co}/\omega)^2}}. \qquad (2.3-6)$$

The case of a circular waveguide is even more complex. Suffice it to say that the dominant mode is analogous to the TE_{10} mode of the rectangular waveguide, and the electric-field distribution in the circular waveguide is a distorted version of that in the rectangular case. The dominant mode for the circular waveguide of diameter d is termed TE_{11} (the indices are defined in cylindrical coordinates). All of the expressions for wavelength in a rectangular waveguide are still valid if the cutoff wavelength is redefined as

$$\lambda_{co} = \frac{2\pi}{\tau'_{00}} \frac{d}{2} = \frac{\pi}{\tau'_{00}} d = 1.71d, \qquad (2.3-7)$$

where τ'_{00} is the first root of the derivative of the zero-order Bessel function. Note that a circular waveguide has a shorter cutoff wavelength than a rectangular waveguide of the same width. This is not surprising because, unlike the rectangular waveguide, the "effective" width of the circular waveguide is less than its physical diameter.

The case in which $\lambda_0 > \lambda_{co}$ is termed "operation below cutoff" with respect to frequency. In this case the waveguide wavelength becomes purely imaginary, and there are no propagating solutions. However, it is apparent from the expressions for the field distributions (Eqs. 2.4-4a,b) that the wave does not stop abruptly; rather it undergoes a "bulk" reflection and is exponentially attenuated. Quantitatively, the variation of the electric field in the z direction is given by

$$E(z,t) = E_0 \exp j(\omega t - k_g z), \qquad (2.3-8)$$

where

$$k_g = \frac{2\pi}{\lambda_g} = 2\pi \sqrt{\frac{1}{\lambda^2} - \frac{1}{\lambda_{co}^2}} = -j \frac{2\pi}{\lambda \lambda_{co}} \sqrt{\lambda^2 - \lambda_{co}^2} \qquad (2.3-9)$$

is the imaginary wavenumber. In the case of perfectly conducting walls, there is no power loss, and an infinitely long waveguide below cutoff acts as a perfect reflector.

2.4 Microwave Resonant Cavities

A microwave resonator can be created by terminating a transmission line or waveguide at both ends with unmatched loads. In the case of open (e.g., parallel wire) transmission lines, such a device is called a resonant line. In this research, however, all of the transmission lines are closed to minimize leakage, and so it is appropriate to discuss resonant cavities exclusively.

A lossless resonator can support passive oscillations at one or more distinct frequencies. These frequencies are termed the natural or resonant frequencies of the resonator. The field patterns (or voltage and current distributions) corresponding to a given natural frequency are termed a resonant mode. If two or more field patterns share a resonant frequency, then those modes are said to be degenerate. In the case of resonant cavities, the two unmatched terminations are separated by an electrical distance that results in phase shift of 2π for a round trip. Most often, the terminations are short circuits. This requires that the resonant cavity be an integral number of half-wavelengths long in order to satisfy the round-trip phase requirement. For transmission-line or waveguide resonators, there are therefore an infinite number of resonant modes. Cavity resonators are usually designed to operate in the lowest-frequency (i.e., dominant) mode.

A rectangular waveguide resonator is shown in Fig. 2.4-1. The dominant mode in this case termed TE_{101}, where the indices are an extension of those described for the rectangular waveguide. The electric field pattern is indicated as well. Recall Eq. 2.3-4.

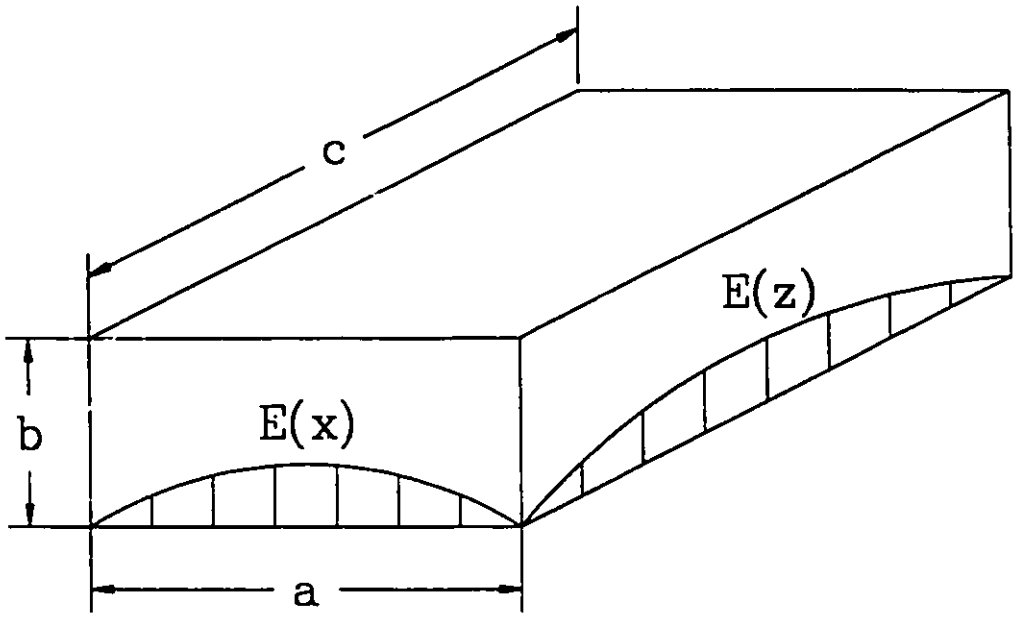

Figure 2.4-1 Rectangular resonant cavity and electric-field distribution for the TE_{101} mode. For convenience, the two distributions are shown as projections on the end and side walls. Actually, these distributions occur along centerlines that are parallel to the x and z axes.

$$\frac{1}{\lambda_g^2} = \frac{1}{\lambda^2} - \frac{1}{\lambda_{co}^2}. \qquad (2.3-4)$$

As before, $\lambda_{co} = 2a$ for a rectangular waveguide. Phase matching at resonance requires that $\lambda_g = 2c$,

$$\lambda = 2\frac{ac}{\sqrt{a^2 + c^2}}, \qquad (2.4-1)$$

for the resonant wavelength of the fundamental mode for the given geometry. As expected, the results are identical whether one considers the resonator a waveguide of width a with

shorting planes separated by c or a waveguide of width c with shorting planes separated by a. For the special case of a "square" resonator (i.e., $a = c$), Eq. 2.4-1 becomes

$$\lambda = \sqrt{2}a. \tag{2.4-2}$$

For a given height and resonant frequency, the square resonator has the smallest volume and largest dimensional tolerances of all rectangular resonators.

To this point, the effect of losses has been neglected. In a real resonant cavity, losses can result from Joule heating of the walls, absorption by materials within the cavity, and leakage from the cavity. The quality factor of a resonator is defined as

$$Q \equiv \omega \frac{(energy\,stored)}{(average\,power\,dissipated)}. \tag{2.4-3}$$

This factor can be shown to be related to the frequency response of a resonator by

$$Q = \frac{\omega_r}{\Delta\omega} = \frac{f_r}{\Delta f}, \tag{2.4-4}$$

where $\Delta\omega$ and Δf are the angular-frequency and cyclic-frequency band widths (as measured from the half-power points), respectively.

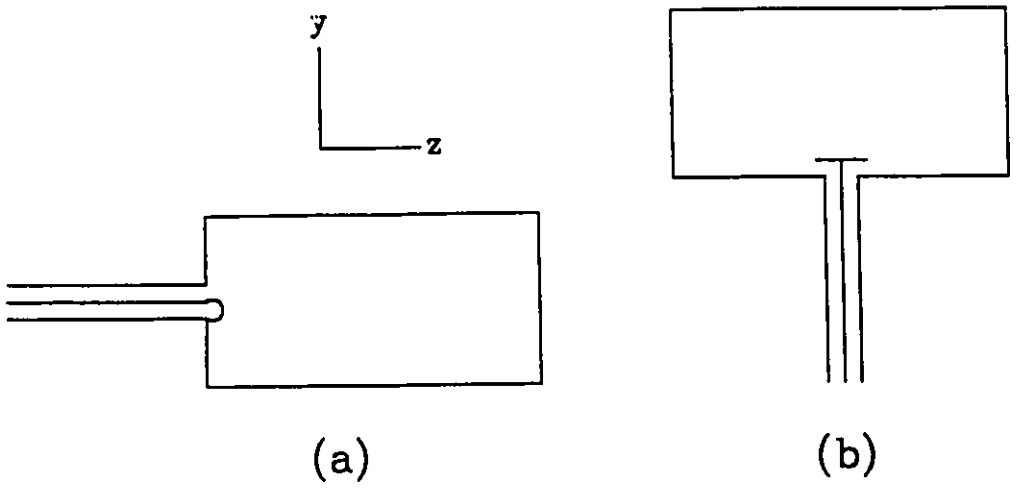

Figure 2.4-2 Loop (a) and probe (b) coupling of a coaxial transmission line to a resonant cavity. Both figures are drawn as cross-sections.

In order for a resonator to be incorporated into a practical system, a method for allowing the transfer of energy into and out of the cavity is required. Coupling to a resonant cavity can be accomplished in at least four distinct ways. For example, if the inner conductor of a coaxial line is formed into a loop that projects into the cavity so that the loop intersects some magnetic flux of a resonant mode, a time-varying voltage on the line will induce a disturbance in the resonator, or *vice versa*. Such a situation is termed "loop coupling"; an example is shown (in cross-section) in Fig. 2.4-2a. Alternatively, the inner conductor can project straight into the cavity so that it couples with the electric field (Fig. 2.4-2b), in which case the term "probe coupling" applies. The coupling probe can be a simple piece of wire, or can be terminated in a disk or more complicated shape in order to provide a better match between the electric fields. Waveguide connections are made using "aperture coupling", in which a hole in a common wall allows some communication between the fields on each

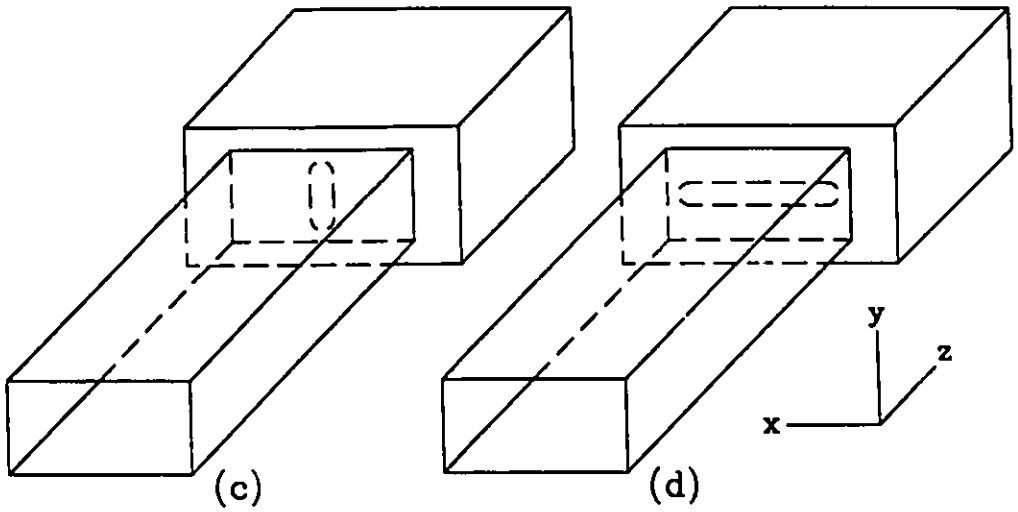

Figure 2.4-2 Aperture coupling of a waveguide to a resonant cavity via the magnetic (c) and electric (d) fields. Although both fields are always present, aperture coupling is usually designed so that one type of field predominates.

side. In aperture coupling, usually one of the magnetic or electric fields is of predominant importance. Examples of magnetic- and electric-field aperture coupling are shown in Figs. 2.4-2c and 2.4-2d, respectively.

It is easy to show that the quality factor of a resonator coupled to a matched line ("loaded Q") must be half of the quality factor of an isolated resonator ("unloaded Q"). When the frequency response of a resonator is measured in practice, the amount of coupling must be minimized by using small probes, loops or holes. A family of frequency response curves for a hypothetical resonator is shown in Fig. 2.4-3. In the case of the top curves, there is so much coupling that the quality factor is much less than the loaded value. As the amount of coupling is reduced, the response falls off, but the quality factor tends towards

its limiting value (i.e., the unloaded Q) asymptotically. In a real resonator, the center frequency would have shifted slightly as the amount of coupling was varied, but in this example this effect has been omitted for simplicity.

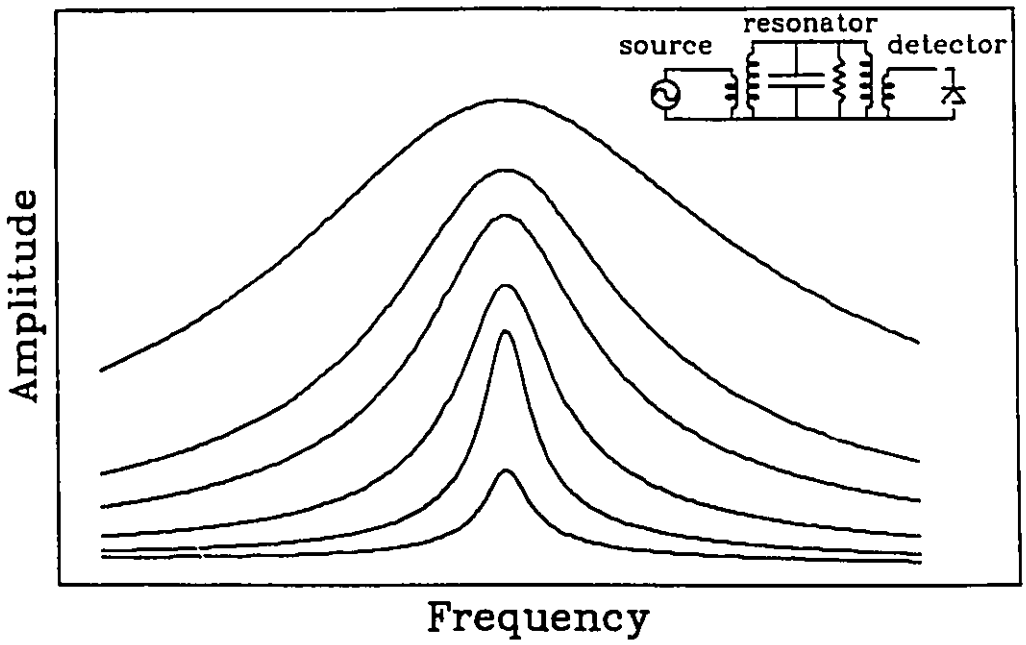

Figure 2.4-3 Frequency response of a resonator employed as a transmission filter for various degrees of coupling. As the degree of coupling is decreased, the Q of the cavity increases asymptotically towards its unloaded value while the transmission decreases towards zero.

2.5 Single Electron in a Microwave Field

A great deal of useful information may be gleaned by considering the case of an isolated electron moving in a temporally-sinusoidal electric field. In such a case, simple

harmonic motion will result. Thus the displacement of the electron as a function of time is given by

$$s(t) = A\sin(\omega t). \qquad (2.5-1)$$

Differentiating with respect to time, one obtains the velocity

$$v(t) = \frac{ds}{dt} = -A\omega\cos(\omega t). \qquad (2.5-2)$$

Differentiating a second time yields the acceleration

$$a(t) = \frac{dv}{dt} = -A\omega^2\sin(\omega t). \qquad (2.5-3)$$

But the acceleration of an electron can also be expressed by

$$a(t) = \frac{F(t)}{m} = -\frac{E(t)e}{m} = -\frac{E_0 e}{m}\sin(\omega t), \qquad (2.5-4)$$

where m is the mass of the electron,

e is the elementary charge,

F is the electric force on the electron, and

$E = E_0\sin(\omega t)$ is the applied field having angular frequency ω.

By comparing Eq. 2.5-3 and Eq. 2.5-4, one obtains an expression for the maximum displacement of an electron in terms of its mass, charge, the applied peak field (E_0) and the applied angular frequency. That is

$$A = \frac{E_0 e}{m\omega^2}, \qquad (2.5-5)$$

where $m = 9.1\times10^{-31}kg$, and $e = 1.6\times10^{-19}C$. The dielectric strength of dry air is $3\times10^{6}V/m$, which represents a useful upper limit for E_0. For $\omega = 2\pi\cdot 2.45GHz$ (a convenient microwave frequency), the maximum travel (2A) for a single electron is only 4.5 mm. Of course, under most circumstances the value of E_0 will be orders of magnitude lower, and the value of A will be reduced still further by electronic collisions. For example, if E_0 is

now taken as $3 \times 10^4 V/m$ (which is easily attainable in a practical microwave resonator), then the maximum travel is reduced to $45 \mu m$. Examination of Eq. 2.5-5 indicates that wall collisions are of sharply increasing importance as the frequency is decreased, and of little importance at microwave frequencies.

In steady state, the total energy that an electron carries alternates between kinetic and potential energy. The total energy is easily found by calculating the kinetic energy of an electron when its speed is at a maximum, namely

$$U = \frac{1}{2} m v_{max}^2 = \frac{1}{2} m (A\omega)^2 = \frac{E_0^2 e^2}{2m\omega^2}. \qquad (2.5-6)$$

Under the conditions given immediately above, the energy of an electron is $5.3 \times 10^{-20} J$ or 0.33 eV. This is a relatively low energy for an electron, and it cannot increase beyond this value under these conditions. Looking at the equations for velocity and acceleration, it is clear that there is a 90° phase shift between them. Therefore, there can be no transfer of energy between the electron and the electromagnetic field. Collisions are required to "de-phase" the electron if it is to acquire more energy.

2.6 Gaseous Breakdown at Microwave Frequencies

Application of a microwave field to a gas will cause an acceleration of all charged particles in the sample. Because the mass of an electron is several orders of magnitude less than that of an ion, the electrons will reach much higher speeds, and the kinetic energy of the ions will be insignificant relative to that of the electrons.

In any practical gas, the presence of at least one electron is assured due to natural effects. Interactions with ionizing radiation, highly energetic collisions between particles in the high energy "tail" of the Maxwellian velocity distribution, and photoelectric emission from nearby surfaces are all mechanisms that can produce free electrons in a gas sample at

room temperature. Under the influence of an applied sinusoidal field, the electrons will acquire some energy from the field and (neglecting collisions) enter into simple harmonic motion. As discussed in the preceding section, the energy carried by each electron is limited if collisions do not occur. Given that ionization potentials are of the order of several electron volts, collisions are required to allow the electrons to become sufficiently energetic to ionize species and produce more free electrons. There are also mechanisms by which free electrons are lost; they may recombine with positive ions, become attached to neutral species forming negative ions, or diffuse out of the region of interest (usually to the walls). If the applied field is strong enough, the electrons will multiply through ionization reactions faster than they are eliminated by recombination, attachment and diffusion. Under such circumstances, the number of charged particles within the volume will increase, and the gas becomes a plasma.

A plasma is often defined as a collection of charged and neutral particles in which electromagnetic interactions between particles dominate. The charged particles can be electrons, positive ions and negative ions. The neutral particles can be atoms or molecules. A plasma is globally neutral because the electrostatic forces are so strong that macroscopic charge separation is prevented. The ionization coefficient is defined as the fraction of particles that carry charge. An ionization coefficient of 5% for a gas at room temperature is usually sufficient to allow the sample to exhibit plasma behavior (Weast, 1986). Some authors (e.g., McDaniel, 1989) make a rigorous distinction between a plasma and an ionized gas. For this thesis, however, such a distinction is not made. In this work, the terms "plasma", "ionized gas", "gaseous discharge" and "microwave discharge" are used largely interchangeably. In addition, the practical definition of the existence of a plasma is taken to be the presence of a luminous arc or volume within the gas sample, even in cases where the ionization coefficient is considerably less that 5%.

The transition from an ordinary gas to a plasma is extremely fast, and is known as gaseous breakdown. At microwave frequencies, the electric field required for breakdown is a function of four other variables: the ionization potential of the gas (u_{ion}), the mean free path of the electrons ($\bar{l}_e$), the diffusion length of the gas vessel, and the free-space wavelength of the applied microwaves (λ). A great deal of theoretical and experimental work has been done on microwave breakdown, and it is possible to make extremely accurate predictions based on this theory. The text by MacDonald (1966) is the definitive work on this subject. As the main concern of this thesis involves the continuous-wave operation of microwave-excited discharges, a detailed discussion of the full breakdown theory is beyond the scope of this work.

2.7 Complex Permittivity of a Plasma

Now consider an electron that is exposed to an electromagnetic field within a plasma. Balancing the forces on the electron (including those due to collisions), one obtains

$$\vec{F} = m\vec{a} = m\frac{d\vec{v}}{dt} = -e\vec{E} - m\nu\vec{v}, \qquad (2.7-1)$$

where ν is the collision frequency for momentum transfer. Assuming that the applied field has an $e^{j\omega t}$ functional form,

$$(j\omega m + m\nu)\vec{v} = -e\vec{E}, \qquad (2.7-2)$$

where phasor notation has been used.

By rearranging and rationalizing, the velocity is

$$\vec{v} = \frac{-e\vec{E}}{j\omega m + m\nu} = \frac{-e\vec{E}}{\omega m\left(j+\frac{\nu}{\omega}\right)}\frac{\left(j-\frac{\nu}{\omega}\right)}{\left(j-\frac{\nu}{\omega}\right)} = \frac{-e\vec{E}\omega(\nu - j\omega)}{m(\omega^2+\nu^2)}. \qquad (2.7-3a)$$

It is sometimes convenient to express this relationship as

$$\vec{v} = \frac{-e\vec{E}}{j\omega m\left(1 - j\frac{\nu}{\omega}\right)}. \qquad (2.7-3b)$$

Hence an expression for the convection current density due to a volume density of N electrons can be written as

$$\vec{j}_c = -Ne\vec{v} = \frac{Ne^2\vec{E}}{j\omega m\left(1 - j\frac{\nu}{\omega}\right)}. \qquad (2.7-4)$$

Furthermore, the displacement current density is

$$\vec{j}_d = \frac{d\vec{D}}{dt} = j\omega\varepsilon_0\vec{E}. \qquad (2.7-5)$$

Therefore, if the ionic contribution is neglected, the total current density is

$$\vec{j} = \vec{j}_d + \vec{j}_c = j\omega\varepsilon_0\left(1 - \frac{Ne^2}{m\varepsilon_0\omega^2\left(1 - j\frac{\nu}{\omega}\right)}\right)\vec{E}. \qquad (2.7-6)$$

Hence the relative permittivity of the plasma can be identified as

$$\varepsilon_r = \left(1 - \frac{Ne^2}{m\varepsilon_0\omega^2\left(1 - j\frac{\nu}{\omega}\right)}\right). \qquad (2.7-7)$$

Defining a plasma frequency by

$$\omega_p^2 \equiv \frac{Ne^2}{m\varepsilon_0}, \qquad (2.7-8)$$

the relative permittivity of the plasma is conveniently expressed as

$$\varepsilon_r = \left(1 - \frac{\omega_p^2}{\omega^2 + \nu^2}\right) - j\left(\frac{\omega_p^2\left(\frac{\nu}{\omega}\right)}{\omega^2 + \nu^2}\right). \qquad (2.7-9)$$

It is evident from the foregoing that the conductivity of the plasma is given by

$$\sigma = \frac{\vec{j}_c}{\vec{E}} = \varepsilon_0\omega_p^2\frac{\nu - j\omega}{\omega^2 + \nu^2}. \qquad (2.7-10)$$

It is instructive to look at a limiting case for these expressions. If collisions are insignificant, (i.e., as $\nu \to 0$) the relative permittivity (Eq. 2.7-9) becomes purely real.

$$\varepsilon_r = 1 - \frac{\omega_p^2}{\omega^2}, \qquad (2.7-11)$$

and the conductivity (Eq. 2.7-10) becomes purely imaginary,

$$\sigma = -j\varepsilon_0 \frac{\omega_p^2}{\omega}. \qquad (2.7-12)$$

As required, these relationships physically correspond to a lossless medium. A real permittivity will induce a phase shift with no power absorption, while a negative imaginary conductivity corresponds to a positive imaginary resistivity and indicates an effective load that behaves as a pure inductor. This is consistent with the fact that the only mechanism for dissipating power is momentum transfer via collisions.

2.8 Collisional Effects

To this point, ν has been implicitly treated as a constant, the so-called collision frequency for momentum transfer. This parameter was introduced to take into account collisional effects and balance the force equation for an electron in a plasma with an applied field. This identification can be justified by considering the effect of a collision on the electron. The change in the electron momentum must be balanced by an impulse, that is

$$\Delta m\vec{v} = -\vec{F}_{coll}\tau, \qquad (2.8-1)$$

where τ is the duration of the collision. If there are many collisions, then the collision frequency for momentum transfer may be defined as the reciprocal of this duration, and the collisional component of the force in Eq. 2.7-1 is

$$F_{coll} = -\frac{\Delta m\vec{v}}{\tau} = -\Delta m\nu\vec{v}. \qquad (2.8-2)$$

Note that this collision frequency is defined for a single electron, and therefore there is no direct dependence on the electron density, N.

Accurate calculation of the collision frequency for practical gases from first principles is exceedingly difficult. A discussion of some specific aspects of non-relativistic collisional processes is appropriate here, but a comprehensive treatment of this subject is far beyond the scope of this thesis. For a good general treatment of this subject, the reader is referred to the text by McDaniel (1989). A more concise treatment can be found in the text by Heald and Wharton (1965).

In general, there are two reference frames that are commonly used in the analysis of collisions: the laboratory frame and the center-of-mass (CM) frame. In the former, particle motion is examined using a co-ordinate system in which the observer is stationary. In a two-body collision, one of the particles (usually the lighter) is termed the incident particle, while the other is termed the target particle. In the laboratory frame, it is often appropriate to consider the target particle as being stationary before the collision. In contrast, the center of mass is taken to be stationary before the collision in the CM frame. Because momentum is conserved, this requires that the center of mass is always stationary in the CM frame. This fact considerably simplifies the analysis. If the collisions under consideration are between electrons and ions or neutral particles, then there is no significant difference between these two coordinate systems.

In the case of elastic collisions (with no external forces acting on the particles), total kinetic energy must be conserved, and in all cases the momentum (both angular and linear) of an isolated system is constant as well. A typical collision trajectory for an electron incident on a massive target is shown in Fig. 2.8-1.

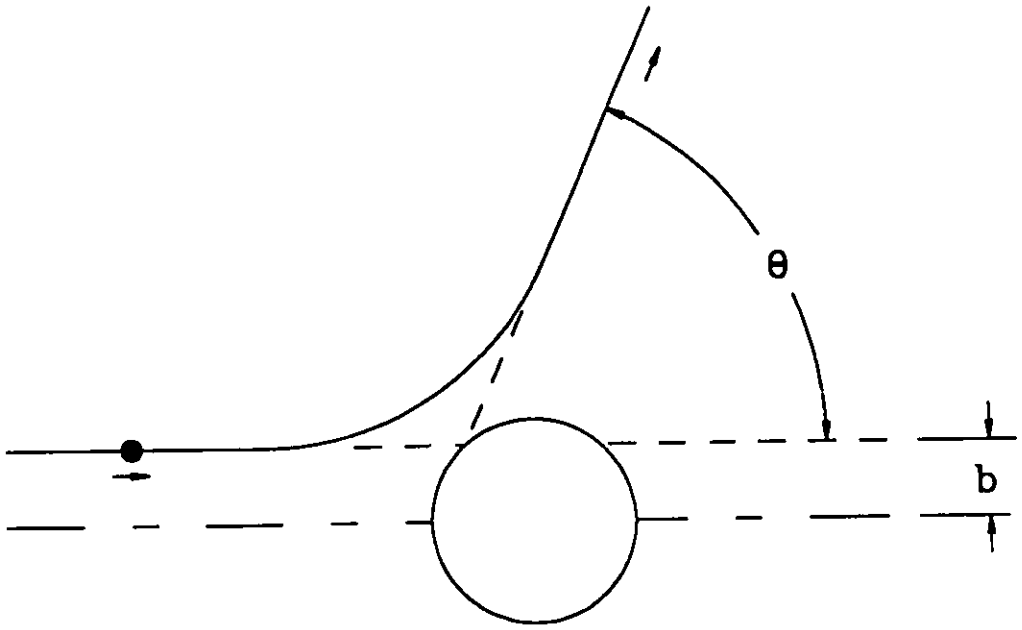

Figure 2.8-1 Classical collision trajectory for an electron incident on a massive target. The dashed lines indicate the trajectory asymptotes. The scattering angle θ is the angle between the two asymptotes. The impact parameter b is shortest distance between the initial asymptote and the target. Note that since the electron is much lighter than the target, this diagram is the same in both the laboratory and CM frames.

Taking N to be the number density of target particles, the probability per unit time (i.e., frequency) of an electron being scattered through θ is given by

$$dP_\theta = N v q_\Omega(v,\theta) d\Omega, \qquad (2.8-3)$$

where the differential solid angle is $d\Omega = 2\pi \sin\theta d\theta$, and $q_\Omega(v,\theta)$ is called the differential scattering cross-section. Integration over 4π steradians gives the total scattering cross-section,

$$q_t(v) = 2\pi \int_0^\pi q_\Omega(v,\theta) \sin\theta d\theta. \qquad (2.8-4)$$

The frequency with which an electron enters into any scattering collision is now given by

$$\nu_s = N q_s v. \tag{2.8-5}$$

The average distance through which an electron travels is called the mean free path, and is related to the scattering collision frequency by

$$\bar{l} \equiv \frac{v}{\nu_s} = \frac{1}{N q_s}. \tag{2.8-6}$$

So far, the transfer of momentum and energy between the particles has not been considered. If the incident particles (electrons) have mass m, and the target particles have mass M, then the condition m << M is satisfied, and the change in energy and forward momentum for the electron can be written as

$$\Delta U = -\frac{2m}{M}(1-\cos\theta)U \tag{2.8-7a}$$

and

$$\Delta(mv) = -(1-\cos\theta)mv. \tag{2.8-7b}$$

The expectation value for the forward momentum change is defined as

$$\langle 1-\cos\theta\rangle \equiv \frac{\int q_\Omega(v,\theta)(1-\cos\theta)d\Omega}{\int q_\Omega(v,\theta)d\Omega}. \tag{2.8-8}$$

Thus the cross-section for momentum transfer can be written as

$$q = \int q_\Omega(v,\theta)(1-\cos\theta)d\Omega = \langle 1-\cos\theta\rangle q. \tag{2.8-9}$$

Therefore, the collision frequency for momentum transfer can be expressed as

$$\nu = N q v = N q_s v \langle 1-\cos\theta\rangle. \tag{2.8-11}$$

Again, it is emphasized that all of these expressions are developed on a per electron basis, and that here N refers to the number density of target particles.

The simplest model for electron-atom collisions is the "hard-sphere" model, in which the target atom is treated as a solid sphere of radius r, and the electron is a point particle. Clearly the closest the centers can come is also given by r. In this case, it can be shown that

$$q = q_s = \pi r^2. \qquad (2.8-12)$$

As simple as this model is, it can yield reasonable results over surprisingly wide ranges.

In an ionized gas or plasma, coulomb scattering and inelastic collisions are the source of the major deviations from the predictions of the hard-sphere model. The former effect is particularly difficult to analyze, as the Coulomb potential gives rise to a long-range force. The long-range potential function causes the integral given in Eq. 2.8-4 to diverge logarithmically unless the limits of integration are restricted in some way. This is not unrealistic, as the forgoing analysis completely ignored the possibility of charge-screening effects, such as Debye shielding. Other difficulties with the hard-sphere model are caused by quantum effects, such as resonances that can occur when the DeBroglie wavelength of the electron is of the same order as the cross-section. These effects are not usually of significance if the electron energy is near or less than 1 eV, meaning that the scattering cross-section is approximately equal to the cross-section for momentum transfer under these conditions (Heald and Wharton, 1965).

Chapter 3

Experimental Apparatus

This chapter describes most of the equipment that was used to perform the experimental research for this thesis. Much of this equipment (e.g., resonators, power supplies) was designed and constructed by the author. The major part of the apparatus is the microwave resonator, which is required not only to couple the microwave energy into the gas discharge efficiently, but to simultaneously allow diagnostic access to the discharge and to minimize microwave leakage. Such leakage can interfere with the proper operation of the support equipment (e.g., oscilloscopes, X-Y recorder, etc.), and can cause physiological damage to the researcher (e.g., eyes, gonads, pancreas, etc.). In addition to equipment, the general procedure is also described in this chapter; any specific amendments are given along with the experimental results that are affected.

3.1 Practical Resonator Design

A practical resonator differs considerably from the simple resonators that are discussed in Section 2.4, in that a means must be provided for coupling microwave radiation

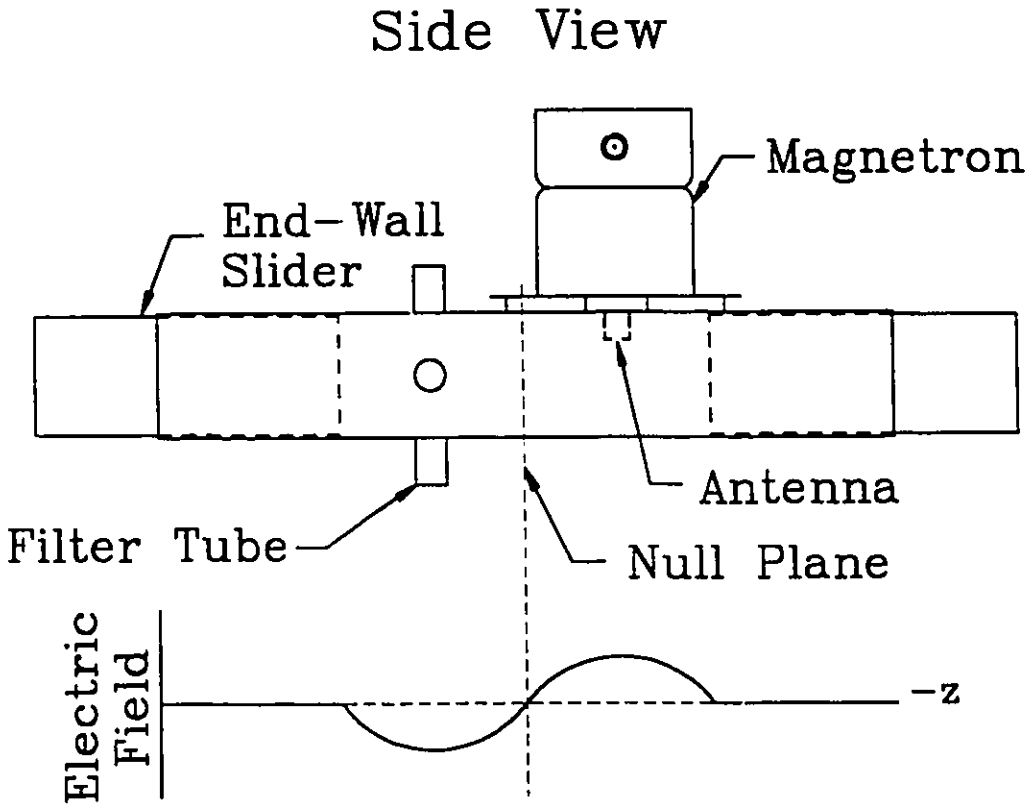

Figure 3.1-1 Side view of the magnetron/resonator assembly constructed for the lamp investigations. For clarity, the clamps described in the text are not shown. The resonator operates in the TE_{102} mode. Tuning of the resonant frequency is accomplished by adjusting the position of the end-wall sliders. The electric-field distribution (in the absence of a discharge) is indicated below the sketch.

into the resonator (e.g., an antenna), and for allowing only optical radiation out (e.g., a metal screen). In addition, a method of adjusting the resonant frequency of the resonator (i.e., tuning) is required when the microwave source has a fixed frequency. For this research, a waveguide resonator that satisfies these requirements was designed and built. Furthermore, the author's design allows the position of the side walls to be changed in order to adjust the resonator width.

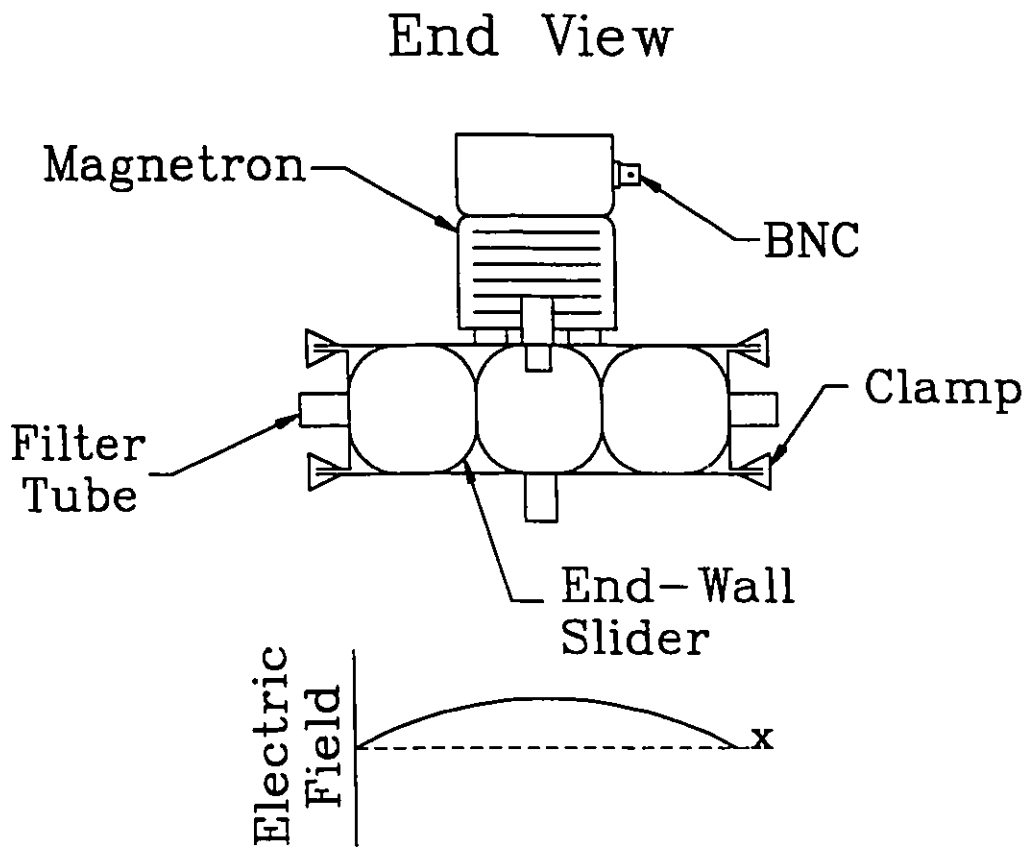

Figure 3.1-2 End view of the magnetron/resonator assembly. Physical and optical access to the cavity is provided through the end-wall sliders or through the filter tubes. A female BNC RF connector allows probe coupling to the cathode assembly of the magnetron, and is used to perform measurements of the cavity Q.

A schematic of the resonator design is indicated in Fig. 3.1-1 (side view) and Fig. 3.1-2 (end view). For all experiments, the resonator is operated in the TE_{102} mode with its width set at 97 mm. The microwave source is a magnetron (Goldstar 2M223), which is mounted on the top surface of the waveguide. The magnetron antenna projects into the cavity to provide coupling to the resonator. Metal filter tubes, which operate far below

cutoff, are attached to the resonator in order to allow the insertion of the discharge tube.

The top and bottom walls are secured to the side walls using 32 spring-steel clips. Because the components are constructed from 1/16" brass stock, they are flexible enough to allow good electrical contact to be made along the length of the resonator using this technique.

Tuning of the resonator is accomplished by adjusting the position of the end-wall sliders. The sliders are made from brass shim-stock and operate as waveguides below cutoff, thereby behaving as resonator walls. The resonant frequency of the cavity is determined by the effective distance between the sliders; the input impedance of the cavity is determined by the distance between the magnetron antenna and the adjacent slider. This design allows a clear view of the discharge tube and the possible use of forced-air cooling.

The use of filter tubes and sliders provides optical and physical access to the interior of the cavity. A discharge envelope, usually a fused-silica tube, can be inserted through the filter tubes. Radiation from the discharge can propagate down the axis of the tube and through a window. Alternatively, the radiation can be collected through the sliders after it passes through the wall of the discharge tube.

Microwave leakage is reduced to acceptable levels using this design. To understand how the sliders and filter tubes work, recall the discussion of waveguides that was given in Section 2.3. In particular, the expressions for the cutoff wavelengths for rectangular and circular waveguides are given as

$$\lambda_{co} = 2a \qquad (2.3-1)$$

and

$$\lambda_{co} \approx 1.71d, \qquad (2.3-7)$$

respectively. Waveguides below cutoff will cause exponential attenuation in the wave. The coefficient for this attenuation is given by Eq. 2.3-9. Twice the product of the length L of the slider or tube and this coefficient expresses the attenuation in Nepers. In decibels,

$$Total\,Power\,Attenuation = 8.686\frac{4\pi L}{\lambda\lambda_{co}}\sqrt{\lambda^2-\lambda_{co}^2}\quad dB. \qquad (3.1-1)$$

The effective diameter of the end-wall sliders is 30 mm, and the inside diameter of the filter tubes is 12 mm. The lengths are 150 mm and 15 mm, respectively. From Eq. 3.1-1, the attenuation for the sliders is 290 dB, and that for the filter tubes is 78 dB. In these calculations, the effect of impedance mismatches has not been included, and so these figures represent minimum attenuation levels.

In order to provide a rough estimate of the total leakage power, we consider an estimate of the power "incident" on the filter tubes and sliders. The total surface area of the side and end walls of the resonator is 14,400 mm^2. The top and bottom surfaces should not be included because Poynting's vector is everywhere parallel to the horizontal plane. Assuming a (very high) power level of 1000 W, the average intensity is 70 mW/mm^2. The total cross-sectional area of the sliders is 5430 mm^2, and that for the filter tubes is 450 mm^2. Thus the power incident on each of these structures is 380 W and 31.5 W, respectively. Using the attenuation levels found above, the leakage from the sliders is completely insignificant ($< 10^{-26}$ W), and that from the filter tubes is less than 10^{-6} W. In reality, if any leakage is detected, it is almost always from the junction between the end-wall sliders and the waveguide. When the resonator is properly tuned and the sliders are well seated, no leakage is observed.

3.2 Cavity Q and Coupling Efficiency

In order to better understand the electrical performance of this resonator, it is useful to calculate the Q for an ideal TE_{102} waveguide resonator and then compare this value to measured values.

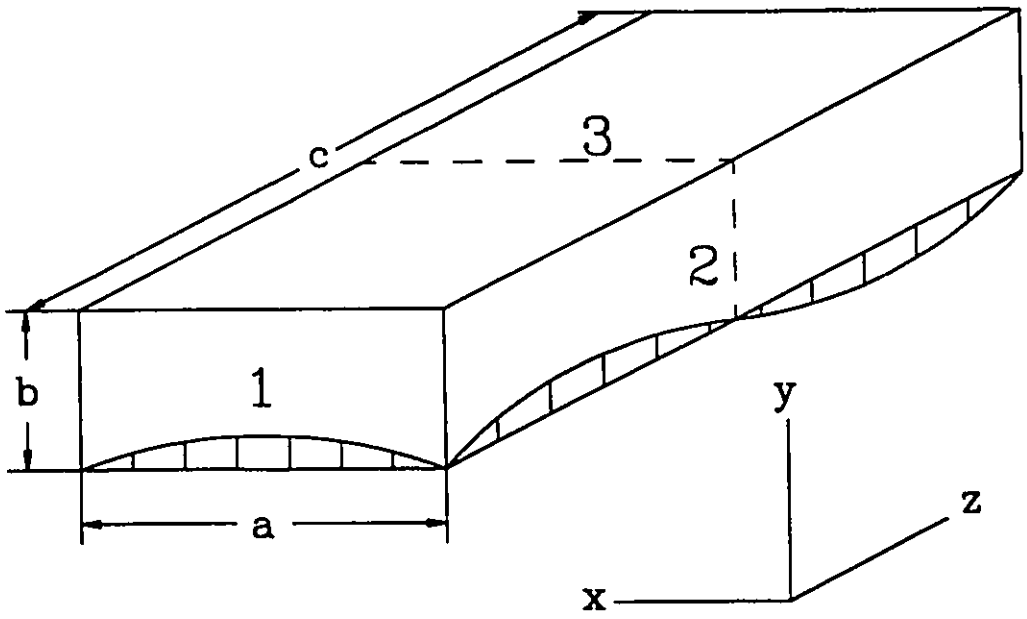

Figure 3.2-1 TE_{102} resonator geometry and dimensions. The standard coordinate axes are also shown. The labelling of the pairs of walls that is used in the calculations is indicated, as is the electric-field distribution. The dashed line corresponds to the position of the null plane.

For convenience, define a surface resistance as the resistance of a square section of wall material having dimensions of $l \times l \times \delta$ (Brown *et al*, 1973, p. 207). Thus

$$R_s = \frac{l}{\sigma l \delta} = \sqrt{\frac{\omega\mu}{2\sigma}}. \qquad (3.2-1)$$

where σ is the material conductivity. Figure 3.2-1 shows the resonator geometry, the coordinate axes and the labelling of the pairs of walls for these calculations. As follows from Eqs. 2.3-5a and 2.3-5b, the phasor component amplitudes can be written as

$$E_y = E_0 \sin\left(\frac{\pi x}{a}\right)\sin\left(\frac{2\pi z}{c}\right) \qquad (3.2-2a)$$

$$H_x = -j\frac{E_0}{Z_0}\sin\left(\frac{\pi x}{a}\right)\cos\left(\frac{2\pi z}{c}\right) \qquad (3.2-2b)$$

$$H_z = j\frac{E_0}{Z_0}\cos\left(\frac{\pi x}{a}\right)\sin\left(\frac{2\pi z}{c}\right). \qquad (3.2-2c)$$

As usual, E_0 is the peak electric-field amplitude and Z_0 is the waveguide impedance, which is given by

$$Z_0 = \frac{\eta}{\sqrt{1-(\omega_{co}/\omega)^2}}. \qquad (2.3-6)$$

Since the mode is TE, $E_x, E_z, H_y \equiv 0$. Integrating the electric field over the volume of the cavity gives the total stored energy

$$W = \frac{1}{2}\int\int\int_V \vec{D}\cdot\vec{E}\,dV = \frac{\varepsilon}{2}\int\int\int_V |E|^2 dV = \frac{1}{8}\varepsilon_0 |E_0|^2 abc. \qquad (3.2-3)$$

Now the power that is dissipated in the six surfaces of the resonator must be found. First, consider a single end wall (e.g., wall 1). The power is found by integrating the Joule-heating losses over the surface of the wall, giving

$$P_1 = \int_0^a \frac{1}{2}|J_s|^2 R_{s1}\,b\,dx$$

$$P_1 = \frac{R_{s1}b|E_0|^2}{2Z_0^2}\int_0^a \sin^2\left(\frac{\pi z}{a}\right)dx$$

$$P_1 = \frac{R_{s1}b|E_0|^2}{4Z_0^2}, \qquad (3.2-4a)$$

where J_s is the sheet current density. Note that the possibility of different wall materials is considered by the subscript on the surface resistance.

Similarly for the other walls,

$$P_2 = \frac{R_{s2} bc |E_0|^2}{4Z_0^2}, \qquad (3.2-4b)$$

$$P_3 = \frac{R_{s3} ac |E_0|^2}{4Z_0^2}. \qquad (3.2-4c)$$

Therefore the total power dissipated is twice the sum of these components, or

$$P_{tot} = \frac{|E_0|^2}{2Z_0^2}(R_{s1}ab + R_{s2}bc + R_{s3}ac). \qquad (3.2-5)$$

The final expression for the quality factor is

$$Q = \omega_r \frac{W}{P_{tot}} = \frac{\omega_r \varepsilon_0 Z_0^2}{4}\left(\frac{abc}{R_{s1}ab + R_{s2}bc + R_{s3}ac}\right) \qquad (3.2-6)$$

The resonator described in the previous section has the following dimensions: a = 97 mm, b = 28 mm and c = 161 mm. The conductivity of brass is $\sigma = 1.57 \times 10^7 S/m$, and the applied angular frequency is $2\pi \cdot 2.45GHz$. It follows that the impedance $Z_0 = 485\Omega$, and that the surface resistance $R_s = .025\Omega$ for each wall. Substituting these data into Eq. 3.2-6 gives $Q \approx 6100$. This value represents an upper limit because the losses due to the construction of the end wall, the access holes in the side and top surfaces and dielectrics within the resonator have been neglected. Furthermore, the magnetron is tightly coupled to the resonator, which will also lower the Q.

In order to determine the quality factor experimentally, a scalar network analyzer (Hewlett-Packard 70100A) was used to measure the two-port frequency response of the resonator/magnetron assembly. A small loop inserted through the end-wall slider and a small probe mounted adjacent to the filament assembly of the magnetron provided coupling.

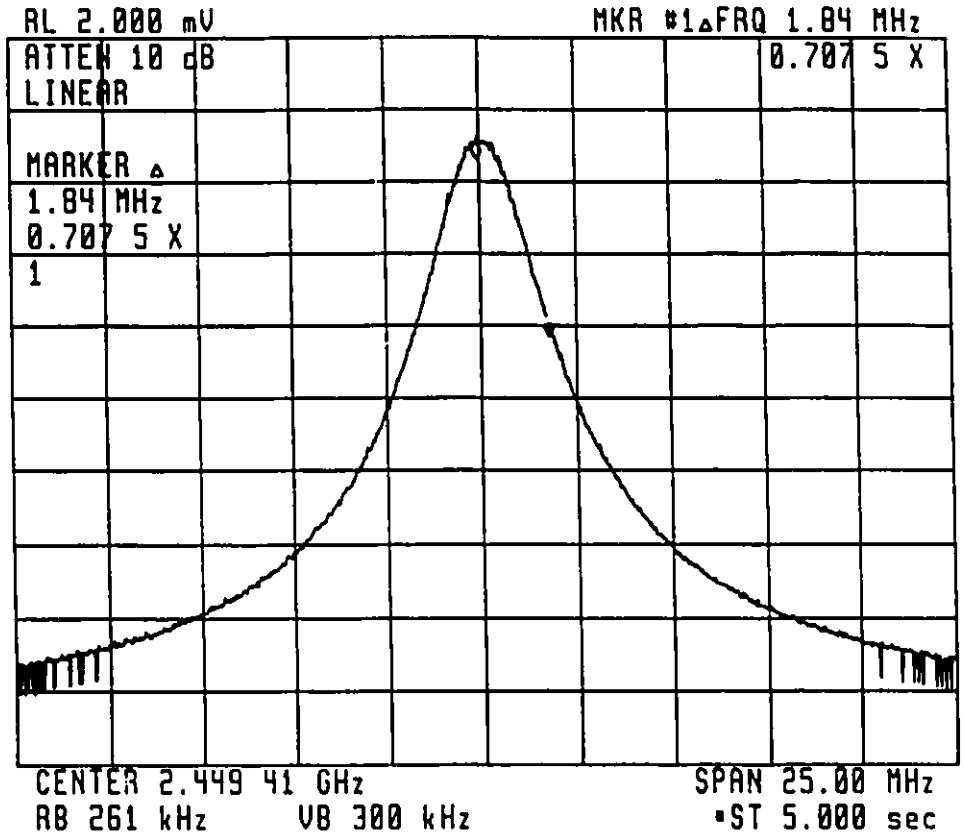

Figure 3.2-2 Two-port frequency response of the "empty" magnetron/resonator assembly as measured on a scalar network analyzer. The frequency range is 25 MHz, yielding a transmission bandwidth of 3.68 MHz, which corresponds to a Q of 665.

The amount of coupling was adjusted to be a minimum while still providing a practical signal-to-noise ratio. The response is measured over a frequency range of 25 MHz centered near 2.45 GHz, and is shown in Fig. 3.2-2. It is evident that the bandwidth is 3.68 MHz, which corresponds to a quality factor of approximately 665. The fact that this is an order of magnitude lower than the value predicted above is not surprising because of the sources of error that have been discussed already.

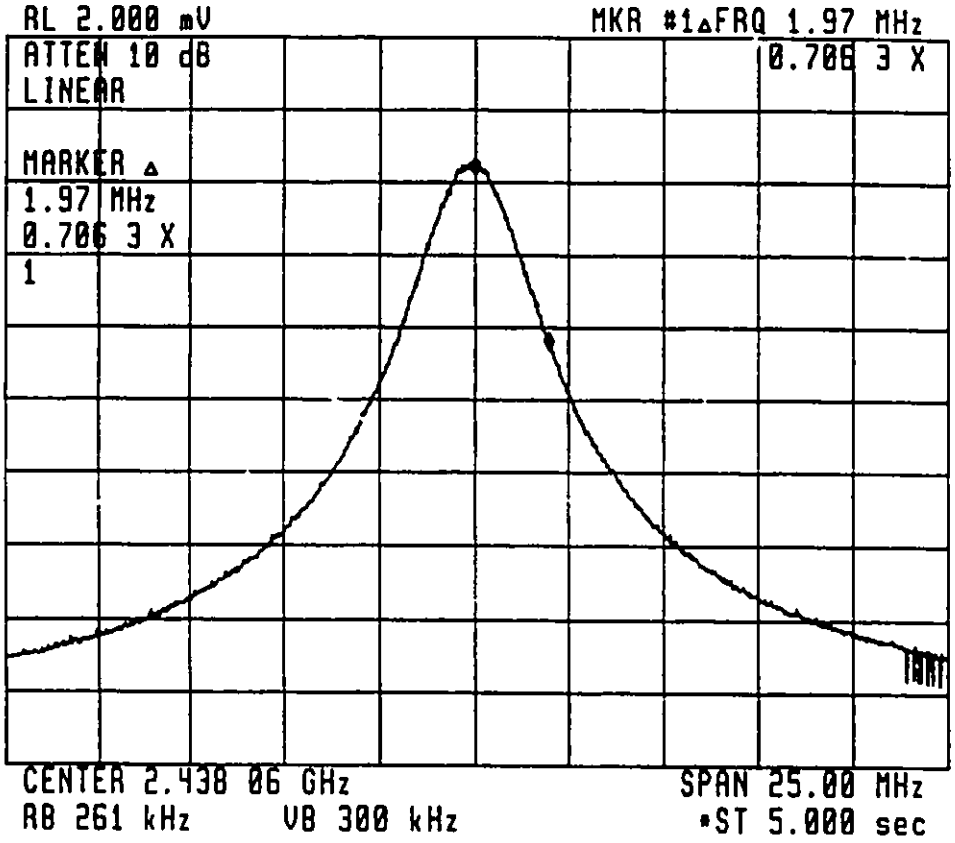

Figure 3.2-3 Two-port frequency response of the magnetron/resonator assembly with a 10-mm diameter fused-silica tube inserted horizontally through the filter tubes. The transmission bandwidth is now 3.94 MHz, which corresponds to a Q of 620. Note the slight shift in the center frequency.

These measurements were repeated with a 10-mm fused-silica tube positioned horizontally through the access holes in the side walls. The corresponding response is shown in Fig. 3.2-3. Note that with the discharge tube in place, the quality factor falls to 620 (i.e., the bandwidth is 3.94 MHz). This indicates that approximately 7% of the microwave power "incident" upon the discharge is absorbed by the tube wall. The presence of the tube also

causes the resonant frequency to decrease slightly (by ~0.5%), as is clear from Fig 3.2-3. This frequency shift can be understood by noting that the relative permittivity of silica is greater than unity. Therefore, the electrical width of the waveguide is increased slightly by the inclusion of the tube, thereby lowering the resonant frequency.

The measurements reported above are precise and reproducible; the uncertainty of the values of Q given is only 2%. However, the scalar network analyzer could not be used in the presence of the high power levels that occur when the magnetron is operating. For this reason, other methods of estimating the Q with a discharge present must be used.

The resonator is tuned by adjusting the position of the end-wall sliders. By measuring the displacement of the slider required to reduce the intensity of the discharge by a factor of 2, the bandwidth of the resonator can be found. This displacement varies with gas composition and pressure, but it is always greater than 3 mm. This indicates that the bandwidth is at least 3.7% of the optimum resonant frequency, corresponding to a quality factor of 26. This value should only be considered an estimate because of many sources of error that are attendant to this procedure. These sources of error include the non-linear response of the discharge to variations in input power levels (i.e., detuning), and the uncertainty associated with the contact between the end-wall sliders and the resonator. Even with these sources of error, this uncertainty is no more than 50%, meaning that the Q of the resonator is always less than 40 when a discharge is present.

The present task is to use this information to provide a measure of coupling efficiency in order to estimate the power that is absorbed by the discharge. Defining Q_1 as the quality factor of the resonator including the empty discharge tube (but no discharge), and Q_2 as the quality factor of the resonator with a discharge present, the quality factor due only to the power absorbed by the discharge can be written as

$$Q_{discharge} = \frac{Q_1 Q_2}{Q_1 - Q_2}. \qquad (3.2-7)$$

It is important to note that this quantity cannot be measured directly, as such a measurement implies that there is no resonator to contain or support the discharge.

Now we can define the coupling efficiency as the ratio of power absorbed by the discharge to the total microwave power available, that is,

$$\frac{P_{discharge}}{P_{2.45GHz}} = \frac{Q_2}{Q_{discharge}} = \frac{Q_1 - Q_2}{Q_1} = 1 - \frac{Q_2}{Q_1}. \qquad (3.2-8)$$

This expression is consistent in the two limiting cases. If $Q_1 = Q_2$, then the discharge does not absorb any energy at all, and the coupling efficiency is zero; if $Q_1 >> Q_2$ then the discharge absorbs virtually all the power and the coupling efficiency is unity.

Taking Q_1 to be 620, and Q_2 to be 40, the coupling efficiency given by Eq. 3.2-8 is found to be 93.5%. Again, this represents a lower limit, since all of measurements that have been used are chosen to provide the most conservative estimate of this value. Also, the value of Q_1 includes the losses due to the fused-silica discharge tube itself. Taking a magnetron efficiency of 70%, the DC coupling efficiency is approximately 65%.

The calculations of this section can be used to find the peak value of the electric field, E_0, in the absence of the discharge. Recall that

$$W = \frac{1}{8}\varepsilon_0 |E_0|^2 abc, \qquad (3.2-3)$$

and that

$$Q = \omega_r \frac{W}{P_{tot}}. \qquad (3.2-6)$$

These two equations can be rearranged to give

$$E_0^2 = \frac{8Q}{\varepsilon_0 \omega_r V} P_{2.45GHz}, \qquad (3.2-9)$$

where V is the volume of the cavity (i.e., V = abc). Again taking Q = 620, substituting the known values into Eq. 3.2-9, and then taking the square root gives the following relationship:

$$E_0 = 9.1 \times 10^3 \sqrt{P_{2.45GHz}} \quad \frac{V}{m}, \tag{3.2-10}$$

where the power is expressed in Watts. As an example, at a microwave power level of 500 W, the peak electric field intensity is $2 \times 10^5 V/m$.

These techniques cannot be easily extended to the cases in which a discharge is present. One immediate difficulty is that the sinusoidal field distribution is drastically altered; another is that the complex permittivity for a plasma must be used in place of the permittivity of free space (see Section 2.7). It is because of these difficulties that the estimation of the electric field within the plasma must be left until Section 4.4 of the next chapter.

Before leaving this topic, a discussion of the importance of energy storage to microwave-excited pulsed discharges is appropriate. The above definitions of Q_1 and Q_2 still hold. Using Eq. 3.2-6, it is convenient to define an energy lifetime by

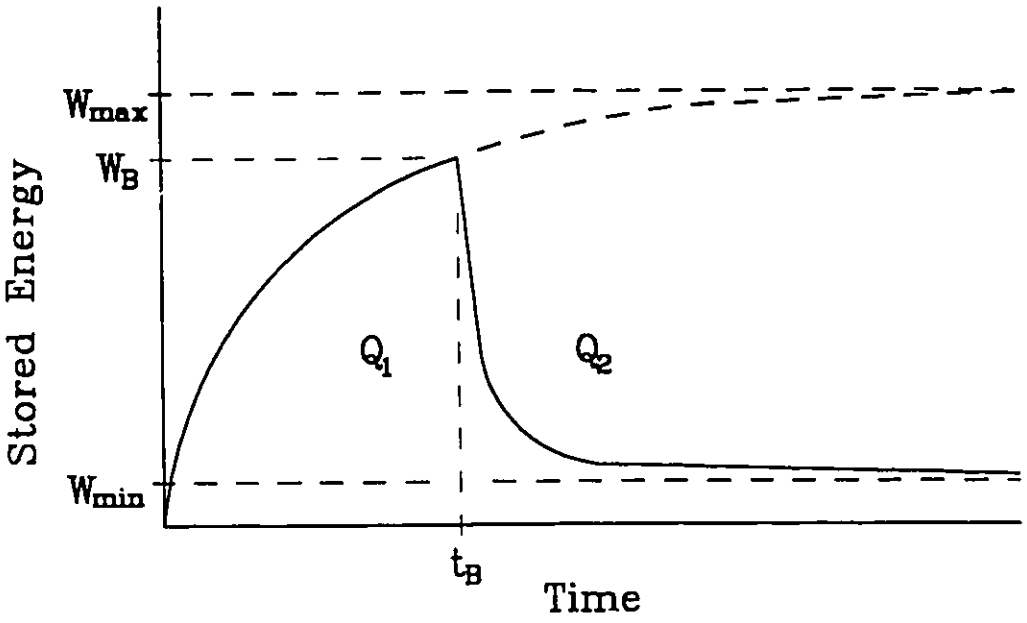

Figure 3.2-4 Energy stored in a resonant cavity as a function of time. Input power, P is constant. Cavity Q is initially Q_1, but instantaneously drops to Q_2 upon discharge formation. The asymptotes W_{max} and W_{min} are steady-state energy values assuming for Q_1 and Q_2, respectively.

$$\tau \equiv \frac{Q}{\omega} = \frac{W}{P}, \qquad (3.2-11)$$

where P is the input power and W is the energy stored in the resonator. If the input power is constant, then W will be a function that increases with time for a given value of Q. Of course, the peak electric-field strength is related quadratically to the stored energy (i.e., $W \sim |E_0|^2$). At some critical electric-field strength (say E_B) the gas will break down, and a discharge will form. For simplicity, assume the breakdown is instantaneous and occurs at time t_B. The stored energy at that instant (denoted W_B) is the maximum that the energy can

ever be for that breakdown condition. Now define τ_1 and τ_2 as the energy lifetimes before and after discharge ignition, that is

$$\tau = \tau_1 = \frac{Q_1}{\omega}, \quad 0 \le t \le t_B$$

$$\tau = \tau_2 = \frac{Q_2}{\omega}, \quad t_B \le t \le \infty \qquad (3.2-12)$$

Clearly, $Q_1 > Q_2$ for an energy-absorbing discharge, as is $\tau_1 > \tau_2$. The variation of the stored energy with time obeys the following differential equation:

$$\frac{dE}{dt} + \frac{E}{\tau} = P = const. \qquad (3.2-13)$$

Taking $W(t=0) \equiv 0$, the solution is

$$W(t) = P\tau_1(1 - \exp(-t/\tau_1)), \quad 0 \le t \le t_B$$

$$W(t) = (W_B - P\tau_2)\exp(-(t - t_B)/\tau_2) + P\tau_2, \quad t_B \le t < \infty \qquad (3.2-14)$$

where the stored energy at breakdown is

$$W_B \equiv W(t_B) = P\tau_1(1 - \exp(-t_B/\tau_1)). \qquad (3.2-15)$$

The variation in energy with time is shown in Fig. 3.2-4. Note that W_{max} is the steady-state value for the stored energy, and is given by

$$W_{max} \equiv P\tau_1. \qquad (3.2-16)$$

Similarly, the steady-state stored energy with a discharge present is

$$W_{min} \equiv P\tau_2. \qquad (3.2-17)$$

These relationships are useful for calculating the power that is transferred to the discharge upon and following breakdown. This power is found by differentiating Eq. 3.2-14 with respect to time to get

$$P_{discharge}(t) \equiv \frac{dW(t)}{dt} = -\left(\frac{W_B}{\tau_2} - P\right)\exp(-(t - t_B)/\tau_2), \qquad (3.2-18)$$

which is only valid for $t \geq t_B$. Note that the negative sign in Eq. 3.2-18 indicates that the discharge is absorbing power from the cavity fields. As a numerical example, consider the experimental values of Q (i.e., $Q_1 = 620$ and $Q_2 = 30$). For $\omega = 2\pi \cdot 2.45GHz$, the corresponding lifetimes are $\tau_1 \approx 40ns$ and $\tau_2 \approx 2ns$. Equation 3.2-15 is not of much practical use for calculating W_B. Instead, Eq. 3.2-3 should be evaluated for the specific resonator employed. In this research, $E_B = 2 \times 10^5 V/m$ is a typical breakdown field. Substituting this value into Eq. 3.2-3 yields a stored energy of 20 μJ. From this energy, it is clear that the power produced by the decay of the field is much greater than the input power. Accordingly, the discharge power at breakdown can be approximated by

$$P_{discharge}(t = t_B) \approx \frac{W_B}{\tau_2}. \qquad (3.2-19)$$

Substituting these values into Eq. 3.2-19 shows that the discharge power at the time of breakdown is 10 kW. The minimum input power required to cause breakdown (i.e., to ensure that $E_{max} > E_B$) is 470 W. It is easy to show that the minimum input power for a desired discharge power at breakdown is given by

$$P_{min} = \frac{Q_2}{Q_1} P_{discharge}(t = \tau_B). \qquad (3.2-20)$$

With optimized geometry, fixed walls and better conductors, it is possible to build resonators having values of Q of up to 30000. Such a resonator used for pulsed microwave excitation could provide discharge powers in excess of 1 MW with input powers of only 1000 W. In light of the values for the energy lifetimes, it is clear that the input power can be pulsed itself, if the duration of the input pulse is much longer than τ_1 (i.e., > 40 ns in this case).

3.3 Electrical Support Equipment

For all of this research, the microwave radiation is generated by a magnetron (Goldstar or Hitachi 2M223). While a full discussion of its operating principles is beyond

the scope of this thesis, some comments on magnetron operation are required. For a comprehensive treatment of this complicated subject, see Reintjes and Coate (1952). A magnetron is essentially a high-power vacuum-tube diode that is operated in forward bias. Because of this, the I-V curve has a very steep slope, and stable DC operation is difficult to achieve. The 2M223 magnetron was designed to be powered by a half-wave voltage doubler circuit, as is usually found in a microwave oven. In this capacity, the power is applied in a train of pulses at a rate of 60 Hz, and thus stabilization is not an issue. However, in this research, a stable microwave power level was needed to make a qualitative analysis of many of the discharge parameters. In addition, DC operation eases the collection and analysis of all kinds of data, such as spectra.

As is the case with almost all high-power vacuum tubes, magnetron operation requires a hot cathode in order to allow electrons to be ejected easily via thermionic emission. For this purpose, a low-voltage (2.5-V) high-current (10-A) AC power supply is provided to heat the cathode filament. The main power supply is a high-power DC supply, and is capable of providing a maximum current of 0.5 A at a maximum voltage of 5000 VDC. As suggested above, small changes in the applied voltage lead to large changes in the current drawn by the magnetron, and therefore also in the instantaneous input power. For this reason, a well-filtered supply is required. In addition, a large ballast resistance is necessary to control fluctuations in the microwave power level.

The schematic diagram of the two supplies that are required to operate the magnetron are given in Fig. 3.3-1. The supply at the top of the figure provides AC power to the magnetron filament. The filament requires between 10 A and 12 A of current to allow the magnetron to operate reliably. This is provided (at a nominal 2.5 V) by a Variac/transformer combination. The secondary winding of the transformer is insulated for safe operation at DC voltages in excess of 5000 V. The negative high voltage from the main supply is connected to the center tap of the filament transformer secondary winding.

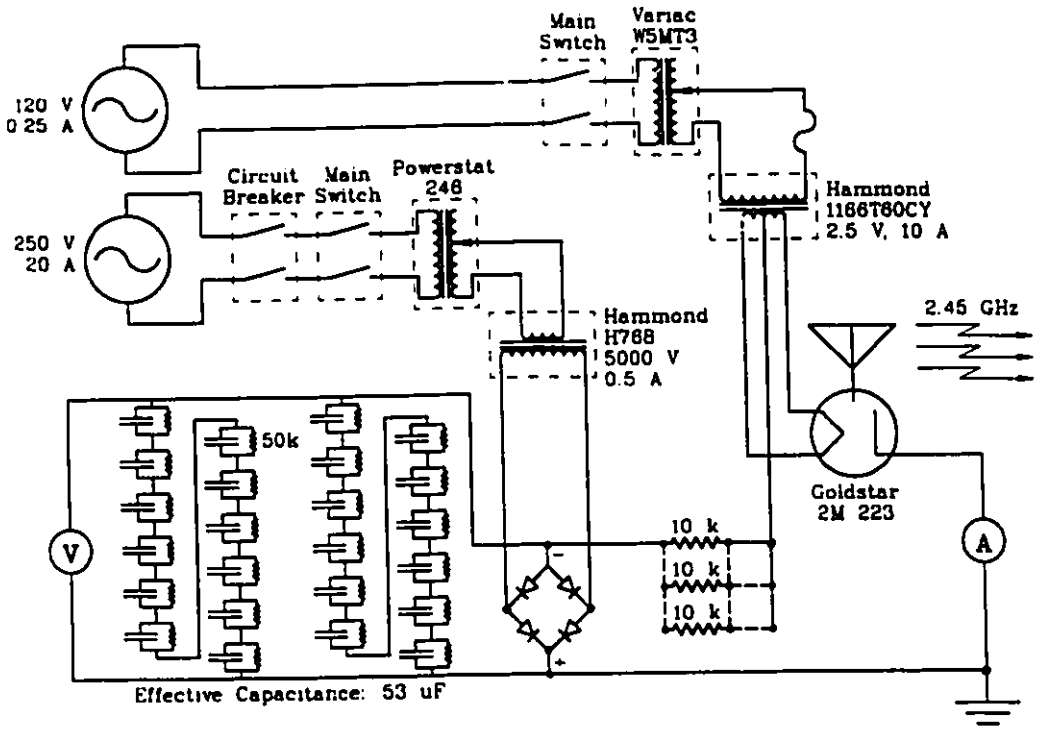

Figure 3.3-1 Schematic diagram of the power supplies that are required to operate the magnetron. All resistance values are in Ohms. The upper supply provides AC power to the magnetron filament. The lower supply provides DC power (at the kilowatt level) that is converted into 2.45-GHz microwave radiation. The wiring of the three 10-kΩ power resistors can be adjusted to provide ballast resistance between 3.3 kΩ and 30 kΩ.

The main supply (shown in the bottom left of Fig. 3.3-1) provides the DC power that is converted into 2.45-GHz microwave radiation by the magnetron. The arrays of capacitors and resistors indicated in the figure furnish passive filtering for the supply. There are two banks, each consisting of twelve electrolytic capacitors (Mallory CGS321T450DD1). Each capacitor has a value of 320 μF and is rated for a maximum DC voltage of 450 V. In the given configuration, the total capacitance of the two banks is 53.3 μF. In order to equalize the voltage across each capacitor, twenty-four resistors (Ohmite

48073) are connected as indicated in the figure. Each resistor has a value of 50 kΩ, rated for a maximum power of 11 W. At a DC voltage of 5000 V, the power dissipation for the entire array is 83.3 W, which corresponds to 3.5 W per resistor.

Ballast resistance is provided by a combination of up to three 10-kΩ power resistors (Marvelohm) that are rated at 200 W each. By adjusting the wiring of these resistors, six different effective resistance values (30 kΩ, 20 kΩ, 15 kΩ, 10 kΩ, 5 kΩ and 3.3 kΩ) can be created. The first four of these configurations have a current limit of 140 mA, the fifth a limit of 285 mA, and the sixth a limit of 425 mA.

The variation of magnetron input power with magnetron voltage (i.e., between cathode and anode) and corresponding anode current is shown in Table 3.3-1 for various ballast resistances. An examination of the ratio of magnetron voltage to anode current confirms that the magnetron operates with a negative differential resistance. The total voltage (i.e., across both the magnetron and the ballast) is also given in the table.

Magnetron Operational Data

Ballast Resistance (kΩ)	Total Voltage (kV)	Magnetron Voltage (kV)	Anode Current (mA)	Power (W)
30.0	2.23	2.20	1.0	2
30.0	3.30	3.15	5.0	16
30.0	3.51	3.21	10.0	32
30.0	3.75	3.30	15.0	50
30.0	4.08	3.32	25.4	84
30.0	4.73	3.22	50.3	162
20.0	4.62	3.22	70.0	225
15.0	4.41	3.21	80.0	257
10.0	4.10	3.20	90.0	288
10.0	4.20	3.20	100.0	320
10.0	4.38	3.18	120.0	382
10.0	4.58	3.18	140.0	445
5.0	3.90	3.15	150.0	472
5.0	4.06	3.18	175.0	557
5.0	4.15	3.15	200.0	630
5.0	4.25	3.00	250.	750
5.0	4.50	3.00	300.	900
5.0	4.75	3.00	350.	1050
3.3	4.37	3.05	400.	1220
3.3	4.75	3.10	500.	1550

Table 3.3-1

3.4 Vacuum and Gas-Handling System

The gas-handling system, which is common to all the experimental work undertaken in this thesis, is shown schematically in Fig. 3.4-1. The gas mixture could be any combination of up to three of the following gases and vapours: He, Ne, Ar, Kr, Xe, SF_6, Cl_2, Br_2, and I_2. In the case of the gases, a two-stage regulator is employed to reduce the pressure to workable values (~10 PSIG). Bromine vapour is obtained from the liquid in a sealed container. Similarly, iodine vapour is obtained directly from iodine crystals in a sealed

container. At room temperature, the maximum partial pressure of I_2 is limited to approximately 12 Torr. Heating the iodine crystals to increase this partial pressure is not advisable because of the contamination problems that would result from significant amounts of iodine precipitating on the inside surfaces ot gas-handling components. Similar contamination is common with bromine, and so steps must be taken to clean the gas handling system after using either of these substances.

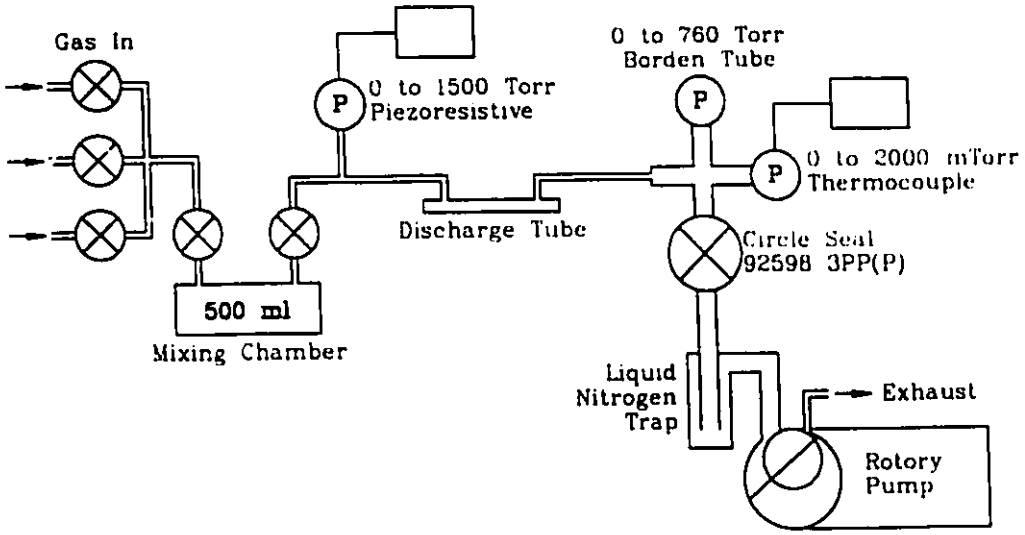

Figure 3.4-1 Schematic diagram of the gas-handling and vacuum system for this research. The gas mixtures are combinations of up to three of the following gases and vapours: He, Ne, Ar, Kr, Xe, SF_6, Cl_2, Br_2, and I_2. The 500 ml chamber ensures complete mixing before the discharge tube is filled.

The vacuum is provided by a rotary pump (Edwards E2M5). A liquid-nitrogen trap is employed to prevent corrosive gases and vapours from entering the pump. In experiments involving fluorine-bearing mixtures, a soda-lime fluorine scrubber is also employed. The vacuum system can provide an ultimate vacuum of less than 50 mTorr.

Two types of tubing are used in the gas-handling system. The vacuum manifold is made from large diameter (> 1/2") copper tubing that is soft soldered to brass and copper fittings. High-vacuum rubber hosing is used to connect the manifold to the liquid nitrogen trap and thence to the pump. Polyethylene tubing (1/4") is used for the other connections.

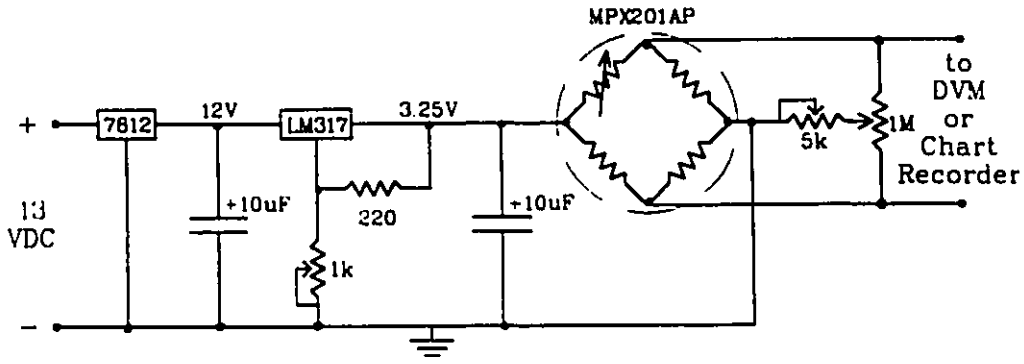

Figure 3.4-2 Schematic diagram of the excitation circuit that is required to operate the piezoresistive pressure transducer. All resistance values are given in Ohms. The 13 VDC input is supplied by a commercially available AC adapter. The circuit output, which is proportional to pressure, is monitored with either a digital voltmeter or an X-Y recorder.

Pressure is measured using three different devices. A simple Borden-tube gauge is used to provide rough measurements over the range of 0 Torr to 760 Torr. A thermocouple gauge (Varian 0531 transducer and 801 millitorr display) is used to check the ultimate vacuum and monitor evacuation over the range 0 mTorr to 2000 mTorr. To prevent damage, the thermocouple gauge is not used in the presence of corrosive gases or vapours. The pressure inside the discharge tube is measured with a piezoresistive pressure transducer (Motorola MPX201AP). This pressure transducer consists of a silicon diaphragm that incorporates a piezoresistive strain gauge into a Wheatstone bridge integrated within the package. One side of the diaphragm is exposed to the pressure to be measured, the other

side is part of a sealed vacuum chamber. The transducer requires an excitation voltage to operate. A circuit was designed and built for this purpose, and is shown schematically in Fig. 3.4-2. A commercially available AC adapter is used to provide the 13 VDC for the excitation circuit. This voltage is first regulated to 12 V and then to a stable value that is adjustable between 2.5 V and 7 V. The potentiometers are used to calibrate and zero the system. The output is fed directly into a digital voltmeter (Hewlett-Packard E2373A Multimeter) or into the X-Y recorder (Hewlett-Packard 2F3). This pressure measuring system was calibrated against a mercury manometer. With an excitation voltage of 3.25 V, an output of 0.1 mV represents 1 Torr of applied pressure.

3.5 General Procedure

There are three distinct types of experiments that are described in this thesis: discharge characterization, spectral measurements and gain investigations. The first two use the same resonator/magnetron combination, and all three use the same gas-handling and support equipment. There are also procedural similarities among these experiments.

Much of the electrical support equipment (e.g., oscilloscope, X-Y recorder, pressure-transducer excitation circuit, etc.) requires a one-hour warm-up period. Accordingly, this equipment is turned on well in advance of taking any measurements.

In cases in which gas mixtures are required, a special procedure is followed in order to control gas composition and ensure complete mixing. To prepare a mixture, the main vacuum valve is closed and the constituent gases are introduced to the 500-ml mixing vessel sequentially. The gas ratio is calculated from partial pressure measurements, which are made using the piezoresistive transducer. Because the volume of the discharge envelope and tubing is much less than that of the mixing vessel, the total pressure of the mixture need

only be slightly higher than the maximum required total pressure of the discharge. After filling, the mixing vessel is isolated and the discharge envelope is evacuated and prepared as described below.

A different discharge envelope is used for each type of experiment, and more design information is given in the appropriate sections. In all cases, the discharge envelope is evacuated to below 100 mTorr and filled with the desired gas or gas mixture several times (to reduce impurity gases) before establishing the discharge. To initiate the discharge, the pressure is adjusted to a few Torr and power is applied to the magnetron. The discharge usually starts immediately; if not, the electric field is concentrated by inserting a sharp metal object (e.g., wire or screwdriver) into the resonator adjacent to the discharge envelope in order to force breakdown to occur. With the discharge established, the total pressure can be adjusted as required. For many gases, discharges can be maintained at many hundreds of Torr total pressure. Except where otherwise noted, the magnetron anode current is set to 100 mA, which corresponds to an input power of 320 W. Given a DC coupling efficiency of 65%, the available microwave power is 210 W for a typical experiment.

A fan is used to blow air across the cooling fins of the magnetron while it is operating. In addition, the discharge characterization and lamp envelopes are cooled using a separate fan, which forces air down the end-wall sliders and across the envelope surface. Without forced-air cooling, it is possible to melt the fused-silica envelope if the discharge is maintained for several minutes at the power levels given above. Due to the intermittent operation of the discharge in the gain investigations, separate cooling of the plasma tube is not required.

Chapter 4

Characterization of a Microwave Discharge

Preliminary steps to characterize a microwave discharge involve examining the propagation of microwaves through a plasma. For this development, an isotropic, linear, homogeneous plasma is assumed. Under the experimental conditions of interest (i.e., no DC magnetic fields, relatively low pressures), the first two plasma properties are always well met, and the last property is a justifiable assumption. An expression for the complex wavenumber k is derived from first principles for such a plasma. The examination of this expression leads to a discussion of the cutoff condition for plasmas with and without electronic collisions.

After investigating microwave propagation in these general terms, the specific case of skin effect is examined. A relationship between plasma frequency and the collision frequency for momentum transfer is developed for a given applied frequency and imaginary wavenumber. A similar relationship for the electron density as a function of collision frequency is also established with applied frequency and skin depth as parameters. An

expression for the electric field within the plasma is developed from previous considerations. The difficulties associated with calculating electron energies by an electromagnetic and collision analysis are discussed. Finally, an analysis of the experimental data for the five lightest noble gases is made using the characterization techniques that are developed in this chapter.

4.1 Microwave Propagation in a Plasma

Again, two of Maxwell's equations are

$$\nabla \times \vec{E} = -\frac{\partial \vec{B}}{\partial t} = -\mu \frac{\partial \vec{H}}{\partial t} \qquad (2.1-1c)$$

and

$$\nabla \times \vec{H} = \frac{\partial \vec{D}}{\partial t} + \vec{J}_c = \varepsilon \frac{\partial \vec{E}}{\partial t} + \sigma \vec{E}. \qquad (2.1-1d)$$

Taking the curl of Eq. 2.1-1c gives

$$\vec{\nabla} \times (\vec{\nabla} \times \vec{E}) = -\mu \frac{\partial}{\partial t} (\vec{\nabla} \times \vec{H}), \qquad (4.1-1)$$

where the curl has been moved inside the differentiation by time.

But

$$\vec{\nabla} \times (\vec{\nabla} \times \vec{E}) = \vec{\nabla}(\vec{\nabla} \cdot \vec{E}) - \nabla^2 \vec{E} \qquad (4.1-2)$$

is a vector identity. Furthermore, the first term on the right goes to zero because there is no net charge in a macroscopic region of the plasma. Comparing Eqs. 4.1-1 and 4.1-2 gives

$$\nabla^2 \vec{E} - \mu\sigma \frac{\partial \vec{E}}{\partial t} - \varepsilon\mu \frac{\partial^2 \vec{E}}{\partial t^2}. \qquad (4.1-3)$$

Now assume a solution of the form

$$\vec{E} = \vec{E}_0 e^{j(\omega t - kz)} \qquad (4.1-4)$$

and substitute it into Eq. 4.1-3. For the non-trivial case, this yields

$$k^2 = \varepsilon\mu\omega^2\left(1 - \frac{j\sigma}{\varepsilon\omega}\right) = \varepsilon\mu\omega^2 - j\mu\sigma\omega. \qquad (4.1-5)$$

In most plasmas at microwave frequencies, the magnetic effects are slight. Therefore letting $\mu_r \to 1$ is justified, and from now on we will take $\mu = \mu_0$. Accordingly, we will also take $\varepsilon_0\mu = 1/c^2$.

From Section 2.7,

$$\varepsilon_r = \left(1 - \frac{\omega_p^2}{\omega^2 + \nu^2}\right) - j\left(\frac{\omega_p^2\left(\frac{\nu}{\omega}\right)}{\omega^2 + \nu^2}\right) \qquad (2.7-9)$$

and

$$\sigma = \frac{\vec{j}_c}{\vec{E}} = \varepsilon_0\omega_p^2\frac{\nu - j\omega}{\omega^2 + \nu^2}. \qquad (2.7-10)$$

It is tempting to substitute both of these expressions into Eq. 4.1-5 simultaneously, but this approach is incorrect. Recall that the expressions for complex conductivity and complex permittivity are derived from the same current-density expressions. The substitution of both Eqs. 2.7-9 and 2.7-10 into the Eq. 4.1-5 includes the same factor twice, and thus leads to an erroneous result. The correct approach is either to substitute the conductivity into Eq. 4.1-5 with unity relative permittivity, or to identify the complex relative permittivity as N^2, where N is the complex index of refraction and its relationship to k^2 is

$$k^2 = \frac{\omega^2}{c^2}\varepsilon_r = \frac{\omega^2}{c^2}N^2. \qquad (4.1-6)$$

Either of these methods lead to

$$k^2 = \frac{\omega^2}{c^2(\omega^2+\nu^2)}\left((\omega^2+\nu^2-\omega_p^2) - j\left(\omega_p^2\frac{\nu}{\omega}\right)\right), \qquad (4.1-7)$$

which is a complex quantity, as expected.

Now consider a complex number, z, expressed in rectanguiar and polar form as

$$z = x + jy = re^{j\theta}, \qquad (4.1-8)$$

with $r = \sqrt{x^2+y^2}$ and $\theta = arctan(y/x)$. The square roots of z are given by

$$z^{\frac{1}{2}} = \pm\sqrt{r}\,e^{j\frac{\theta}{2}} = \pm\sqrt{r}\left(\cos\frac{\theta}{2} + j\sin\frac{\theta}{2}\right). \qquad (4.1-9)$$

But the half-angle formulae are

$$\cos^2\frac{\theta}{2} = \frac{1+\cos\theta}{2} \qquad (4.1-10a)$$

and

$$\sin^2\frac{\theta}{2} = \frac{1-\cos\theta}{2}. \qquad (4.1-10b)$$

In addition, $\cos\theta = x/r$, so that the roots of z can be expressed (in rectangular form) by

$$z^{\frac{1}{2}} = \pm\left(\sqrt{\frac{r+x}{2}} + j\sqrt{\frac{r-x}{2}}\right). \qquad (4.1-11)$$

In the case of $z = k^2$,

$$x \equiv \frac{\omega^2}{c^2(\omega^2+\nu^2)}(\omega^2+\nu^2-\omega_p^2) \qquad (4.1-12a)$$

and

$$y \equiv \frac{\omega^2}{c^2(\omega^2+\nu^2)}\left(-\omega_p^2\frac{\nu}{\omega}\right). \qquad (4.1-12b)$$

Now considering only the "positive" root, split k into its real and imaginary parts, which are

$$k' \equiv Re(k) = \sqrt{\frac{\sqrt{x^2 + y^2} + x}{2}} \qquad (4.1-13a)$$

and

$$k'' \equiv Im(k) = \sqrt{\frac{\sqrt{x^2 + y^2} - x}{2}}. \qquad (4.1-13b)$$

After making the appropriate substitutions, the final expressions are

$$k' = \frac{\omega}{c\sqrt{\omega^2 + \nu^2}} \sqrt{\frac{\sqrt{(\omega^2 + \nu^2 - \omega_p^2)^2 + \left(\omega_p^2 \frac{\nu}{\omega}\right)^2} + (\omega^2 + \nu^2 - \omega_p^2)}{2}} \qquad (4.1-14a)$$

and

$$k'' = \frac{\omega}{c\sqrt{\omega^2 + \nu^2}} \sqrt{\frac{\sqrt{(\omega^2 + \nu^2 - \omega_p^2)^2 + \left(\omega_p^2 \frac{\nu}{\omega}\right)^2} - (\omega^2 + \nu^2 - \omega_p^2)}{2}}. \qquad (4.1-14b)$$

Recognizing that k is complex, we can rewrite Eq. 4.1-4 as

$$\vec{E} = \vec{E}_0 e^{j(\omega t - kz)} = \vec{E}_0 e^{j(\omega t - k'z)} e^{-k''z}. \qquad (4.1-15)$$

The parameter k" determines the attenuation of the electromagnetic wave in the plasma. From the above discussion, it is clear that k" can never be negative. It is appropriate to explain the physical significance of these relationships by making reference to four special cases.

1) No collisions, below cutoff:

Mathematically, this corresponds to $\nu = 0$ and $\omega < \omega_p$. Under these conditions, $k'' > 0$, and there is exponential attenuation. However, this situation is analogous to a perfectly con-

ducting waveguide operating below cutoff. There is no power dissipated in the plasma, and all of the attenuation is accounted for by bulk reflection within the plasma. Such reflection is distinct from reflections at the plasma boundary.

2) No collisions, above cutoff:

Again, $\nu = 0$, but here $\omega > \omega_p$. This means that $k'' \equiv 0$. The electromagnetic wave experiences no losses and so the plasma acts like a perfect dielectric.

3) With collisions, below cutoff:

Now $\nu > 0$ and the cutoff condition must be modified. "Below cutoff" specifies that $\omega^2 + \nu^2 < \omega_p^2$. Under these conditions, $k'' > 0$, and there is exponential attenuation for the wave as it propagates through the plasma. In this case, the attenuation is partially attributable to bulk reflection by the plasma, and partially attributable to power absorption via collisional gas heating.

4) With collisions, above cutoff:

Again $\nu > 0$ and $\omega^2 + \nu^2 > \omega_p^2$. Now it is still true that $k'' > 0$, and there is exponential attenuation of the wave in the plasma, but now all of the attenuation is due to collisional processes, and there is no bulk reflection from the plasma.

Because collisions do occur, it is the last two situations that are of practical importance in this thesis. Furthermore, it is possible to derive an expression for the power that is absorbed from the wave by the plasma. The most direct way to do this is to look at the power density, defined by

$$p \equiv \vec{j}_c \cdot \vec{E} = Re(\sigma |E^2|) = \frac{\varepsilon_0 E_0^2 \omega_p^2 \nu}{\omega^2 + \nu^2} e^{-2k''z}. \qquad (4.1-16)$$

4.2 Skin Effect in a Plasma Sheath

It is useful to rearrange Eq. 4.1-14b in order to formulate an expression for the plasma frequency in terms of the collision frequency for momentum transfer, the applied angular frequency and the imaginary wavenumber. After considerable algebra and an application of the quadratic formula, one obtains

$$\omega_p^2 = \sqrt{\frac{\omega^4}{\nu^4}d^4 + \frac{\omega^2}{\nu^2}d^4 + 2\frac{\omega^2}{\nu^2}(\omega^2+\nu^2)d^2} - \frac{\omega^2}{\nu^2}d^2, \qquad (4.2-1)$$

where, for convenience, the parameter d^2 is defined by

$$d^2 \equiv 2\frac{c^2(\omega^2+\nu^2)}{\omega^2}(k'')^2. \qquad (4.2-2)$$

Assuming that the plasma is nearly homogeneous on a microscopic scale, k" is simply the reciprocal of the skin depth, that is

$$\delta \equiv \frac{1}{k''}. \qquad (4.2-3)$$

From Eq. 4.1-15, it is apparent that the skin depth is the thickness of plasma that causes the electric field to be attenuated by a factor of e. Because the intensity of the wave is proportional to the square of the electric field, over 85% of the power that is absorbed by the plasma will be dissipated within a skin depth of the plasma boundary. This expression is of particular use because it corresponds to an observable situation. If the optical emission intensity from the plasma is assumed to be proportional to the power deposited by the wave, then Eq. 4.2-1 can be used to determine k" and thence to help characterize the discharge. Figure 4.2-1 shows a log-log graph of a family of curves given by Eq. 4.2-1, for various values of k", at a frequency of 2.45 GHz. From these curves, it is clear that, for skin depths less than 10 mm (i.e., k" > 100), the plasma frequency is constant until it increases monotonically from this asymptotic minimum value. For skin depths greater than this value, a

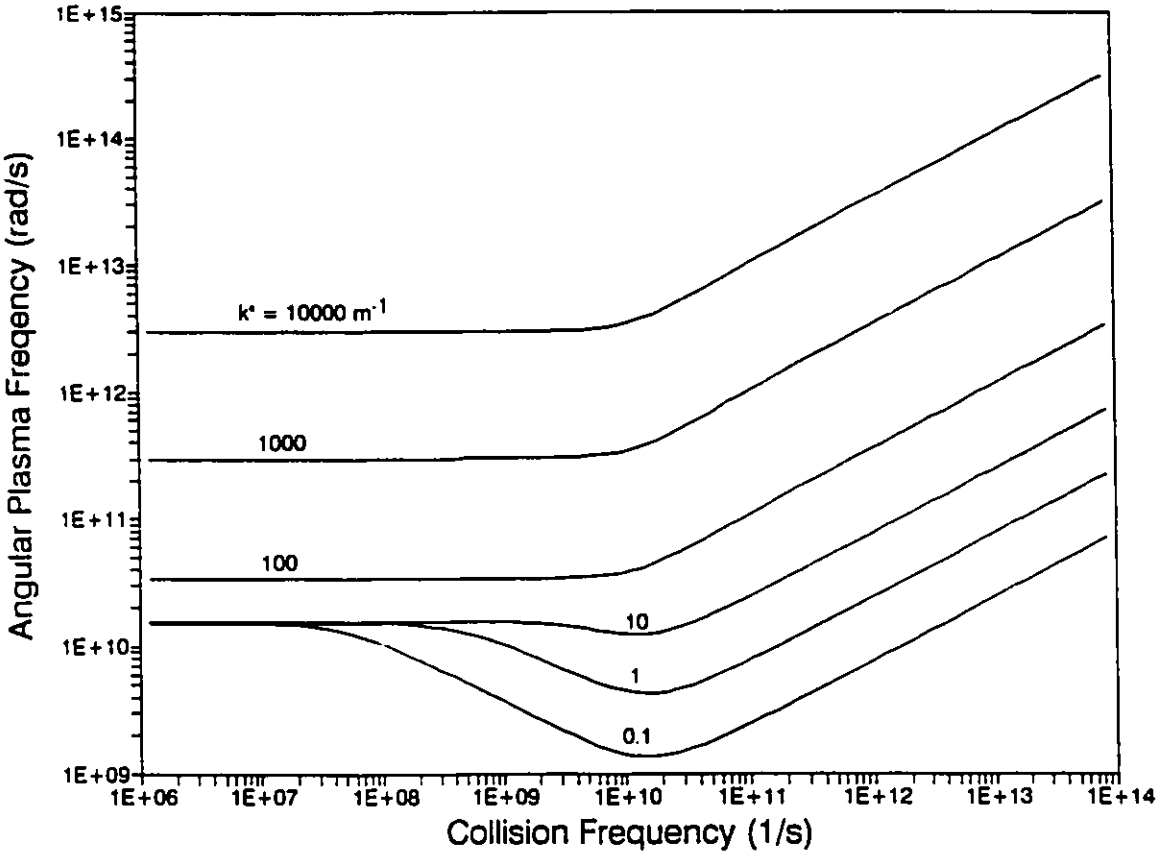

Figure 4.2-1 Log-log graph of a family of curves relating plasma frequency to the collision frequency for momentum transfer for several values of the imaginary part of the wavenumber, k". The parameter k" is the reciprocal of skin depth, and the applied frequency is 2.45 GHz.

local minimum is seen to develop for collision frequencies near 10^{10} #/s. In either case, Fig. 4.2-1 shows that there is a minimum value for the plasma frequency for a given skin depth, and that the plasma frequency is not significantly dependant on collision frequency over a wide range of values.

4.3 Determination of Electron Density

From Section 2.7, the plasma frequency is defined as

$$\omega_p^2 \equiv \frac{Ne^2}{m\varepsilon_0}. \tag{2.7-8}$$

which can be rearranged as

$$N = \frac{m\varepsilon_0}{e^2}\omega_p^2. \tag{4.3-1}$$

Substituting Eq. 4.2-1 into Eq. 4.3-1 yields the extremely useful relationship

$$N = \frac{m\varepsilon_0}{e^2}\left(\sqrt{\frac{\omega^4}{\nu^4}d^4 + \frac{\omega^2}{\nu^2}d^4 + 2\frac{\omega^2}{\nu^2}(\omega^2+\nu^2)d^2} - \frac{\omega^2}{\nu^2}d^2\right), \tag{4.3-2}$$

where Eqs. 4.2-2 and 4.2-3 are combined to express d^2 as a function of skin depth:

$$d^2 \equiv 2\frac{c^2(\omega^2+\nu^2)}{\omega^2\delta^2}. \tag{4.3-3}$$

The dependence of electron density on the collision frequency for momentum transfer is shown in Fig. 4.3-1. Given is a family of curves, corresponding to various skin depths, all for an applied microwave field at a frequency of 2.45 GHz. For all practical purposes, a skin depth of 100 mm is indistinguishable from one of 10 m due to the size of the apparatus used in the experiments. It is clear that if any skin effect is observed experimentally, then the electron density must be in excess of $5 \times 10^{10}/cm^3$.

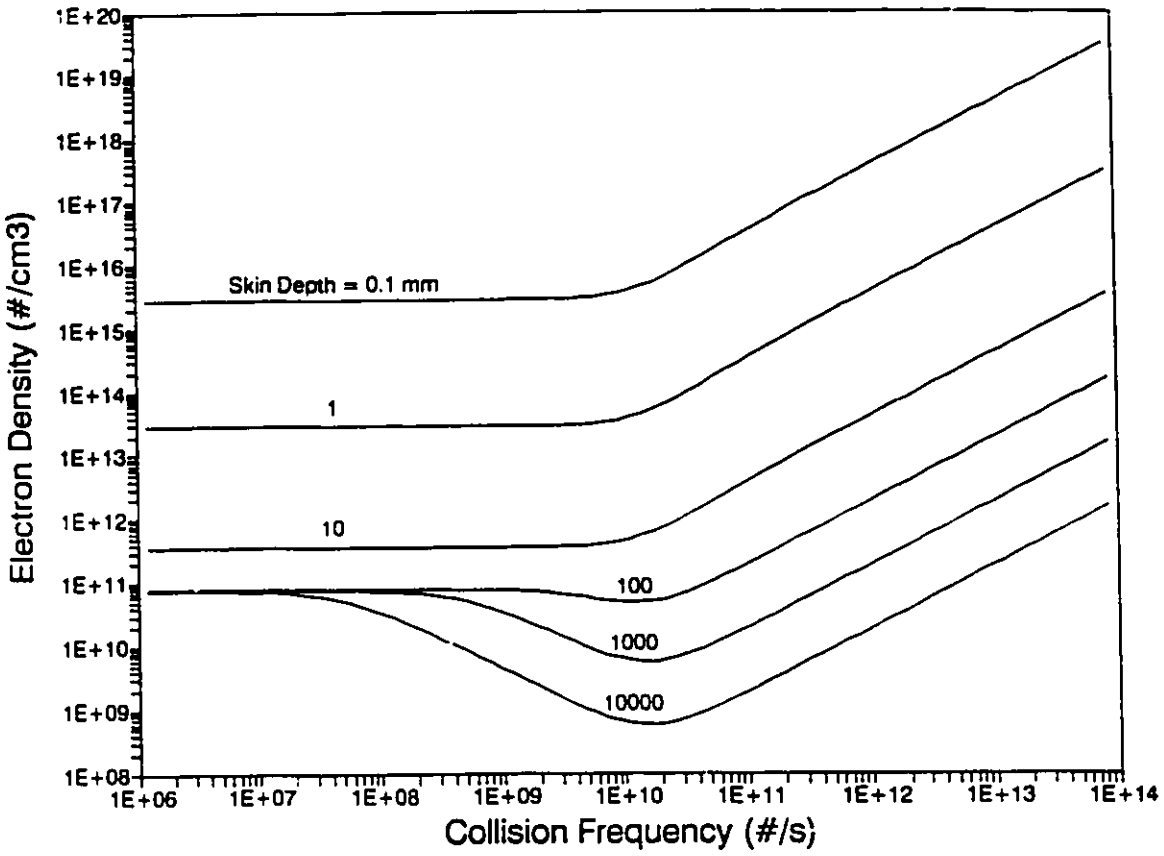

Figure 4.3-1 Log-log graph of a family of curves relating electron density to the collision frequency for momentum transfer for several values of skin depth. The applied frequency is 2.45 GHz. The skin depth is reasonably approximated as the observable sheath thickness of the discharge.

4.4 Electric-Field Strength in a Plasma

In Section 3.2 of the previous chapter, the peak electric-field strength is calculated for a TE_{102} resonator. Specifically, the peak electric-field strength, given in terms of the microwave power, the angular frequency, the cavity volume and the cavity Q is

$$E_0^2 = \frac{8Q}{\varepsilon_0 \omega_r V} P_{2.45GHz}. \qquad (3.2-9)$$

Unfortunately, the same approach could not be used to find the peak electric-field strength in cases in which a plasma is present. The presence of a discharge radically alters the field distributions. In addition, the complex permittivity of the plasma must be taken into account. It is necessary to solve this problem using a different approach.

In a sense, this problem has been dealt with already. In Section 4.1, the imaginary wavenumber for a plasma and the variation of the electric field within is determined. That treatment (see Eqs. 4.1-14 and 4.1-15) assumes that the plasma is homogeneous, isotropic and linear, and neglects reflections from the plasma boundary. The spatial variation of the power is also developed for those conditions, is given by

$$p \equiv \vec{j}_c \cdot \overrightarrow{E^*} = Re(\sigma |E^2|) = \frac{\varepsilon_0 E_0^2 \omega_p^2 \nu}{\omega^2 + \nu^2} e^{-2k''z}. \qquad (4.1-16)$$

where k" is

$$k'' = \frac{\omega}{c\sqrt{\omega^2+\nu^2}} \sqrt{\frac{\sqrt{(\omega^2+\nu^2-\omega_p^2)^2 + \left(\omega_p^2 \frac{\nu}{\omega}\right)^2} - (\omega^2+\nu^2-\omega_p^2)}{2}}. \qquad (4.1-14h)$$

But the power absorbed by the discharge is known from Section 3.2. Rearranging Eq. 3.2-8, one obtains

$$P_{discharge} = \left(1 - \frac{Q_2}{Q_1}\right) P_{2.45GHz}, \qquad (4.4-1)$$

where Q_1 and Q_2 are defined as the quality factor for the resonator excluding and including the discharge, respectively. The total power is related to the power density by an integration over the active volume of the discharge, that is

$$P_{discharge} \equiv \int\int\int_{V_{eff}} p\, dV. \qquad (4.4-2)$$

The only spatial variation in the power density is in the direction of propagation, and is in fact an exponential attenuation. Thus the maximum power density, occurring at the plasma boundary, is

$$p = \frac{\varepsilon_0 E_0^2 \omega_p^2 \nu}{\omega^2 + \nu^2}. \qquad (4.4-3)$$

Therefore Eq. 4.4-2 becomes

$$P_{discharge} = \int\int\int_V p\,dV = p\,V_{eff}, \qquad (4.4-4)$$

where V_{eff} is the effective volume of the discharge. This volume takes into account the spatial variation of the power density and the value of the imaginary wavenumber. In plasmas for which the attenuation (i.e., k") is large, the effective volume is less than the actual volume contained by the discharge envelope in order to ensure the equality in Eq. 4.4-4.

Rearranging the above expressions gives an approximate relationship between the peak electric-field strength and the microwave power, namely

$$E_0^2 \approx \frac{(1 - Q_2/Q_1)(\omega^2 + \nu^2)}{\varepsilon_0 \omega_p^2 \nu V_{eff}} P_{2.45GHz}. \qquad (4.4-5)$$

It is desirable to evaluate Eq. 4.4-5 for values that correspond to practical experimental conditions in order to estimate upper and lower limits for the electric-field strength within the discharge. In order to do this, consider the case of a horizontal 6.5-mm ID discharge tube, for which the internal volume is 3220 mm^3. Take the total microwave power level to be 220 W and the coupling efficiency to be ~93% (i.e., typical experimental values). As usual, the angular frequency is $1.54 \times 10^{10} rad/s$. For the lower limit, the denominator must be maximized and the numerator minimized. In this case, a reasonable upper limit on collision frequency is a value of 10^{12} #/s. From Fig. 4.2-1, the plasma frequency is 10^{13} rad/s

for a skin depth of 0.4 mm. Thus the effective volume is that of a hollow cylinder having walls one skin depth thick (i.e., 750 mm^3). Substituting these values into Eq. 4.4-5 puts a lower limit on the peak electric field of $5.5 \times 10^2 V/m$.

For the upper limit, the numerator must be maximized and the denominator minimized. This criterion implies a low collision frequency, 10^7 #/s for example. At this collision frequency, there will be minimal attenuation of the microwave field. Therefore the plasma frequency (from Fig. 4.2-1) is $1.54 \times 10^{10} rad/s$, and the effective volume is the full inside volume of the tube (3220 mm^3). Taking coupling losses into account, this corresponds to a maximum field strength of $8.5 \times 10^5 V/m$, which can be taken to be an effective upper limit. A word of caution is appropriate here. This electric field is slightly in excess of that calculated for an empty resonator under the same conditions. The problem lies in the calculation of the coupling efficiency; under conditions of small attenuation, the Q of the resonator (including the discharge) is higher than the value of 30 that has been used in the calculation, and so the discharge power is actually lower than predicted. The method of estimating Q described in Section 3.2 is not valid under these circumstances.

4.5 Estimation of Electron Energy

Unfortunately, typical electron energies are not so easily found as electron densities or peak electric-field strengths. However, reasonable estimates can be made and thus discussion of this topic is still warranted. In Section 2.5, it is shown that the maximum kinetic energy that a single electron carries in a microwave field is given by

$$U = \frac{1}{2} m v_{max}^2 = \frac{E_0^2 e^2}{2m\omega^2}. \qquad (2.5-6)$$

As usual, the frequency of the applied microwave field is 2.45 GHz. After substituting the values of the physical constants, Eq. 2.5-6 becomes

$$U = \frac{1}{2} m v_{max}^2 = 3.71 \times 10^{-19} E_0^2 \quad eV, \qquad (4.5-1)$$

where the electric field is in V/m, and the energy is in eV. Again, the energy given by Eq. 4.5-1 is in fact the total energy of the electron, and all electrons under the influence of the microwave field have that energy (in steady state) if there are no collisions.

Now consider a group of electrons that are present in a volume of ionized gas. These electrons will undergo collisions, as was discussed in Section 2.8. The collision frequency for scattering has been shown to be

$$\nu_s = N q_s v, \qquad (2.8-5)$$

where N is the target-particle density. In general, the scattering cross-section q_s is a function of the velocity v; consequently, the linear relationship between collision frequency and velocity that is indicated in Eq. 2.8-5 is only valid in special circumstances. For the purposes of this discussion, such linearity is assumed to be a reasonable approximation. In particular, the development (given in the previous sections) of an expression for the electron density (as a function of the collision frequency and skin depth) indicates that the collision frequency for scattering is not strongly dependant on the electron density. This independence is also true of the scattering cross-section. However, the velocity distribution is strongly dependent on collision frequency, and therefore the equations are coupled in an extremely inconvenient way.

The simplest case is that in which the collision frequency for scattering is much lower than the cyclic frequency of the microwave field. Under this condition, the electron energy (ignoring any thermal effects) is given by Eq. 4.5-1 with reasonable accuracy. It is also implied that the collision frequency for scattering is approximately equal to the collision frequency for momentum transfer, which is often true. As will become apparent in the next section, the first condition is very rarely met in practice; only in cases of low pressures and

small collision cross-sections is the collision frequency low enough to be ignored.

4.6 Experimental

In the previous three sections, expressions are given that relate several observable, measurable and/or estimable parameters to the electron density, electric field strength, and collisionless electron energy. Experimentally, the primary observable parameter that is used to characterize the discharge is skin depth. As is discussed previously, the presence of a plasma causes the microwave field to be attenuated. To first order, the optical emission from a point in the discharge is proportional to the power that is absorbed from the microwave field. Under the present assumptions, the absorbed power is in turn proportional to the incident power. In a real discharge, the plasma is often observed to be confined near the inside walls of the envelope. The thickness of the plasma sheath can be measured, and it is taken to be the skin depth of the plasma.

In order to allow a greater range of values to be observed, a large-diameter discharge envelope is employed (see Fig 4.6-1). This discharge envelope is constructed from fused-silica tubing and fused-silica windows. The gas inlets for this structure are bent in order to penetrate the end-wall sliders. This design eliminates the need to remove the side walls in order to remove the discharge envelope.

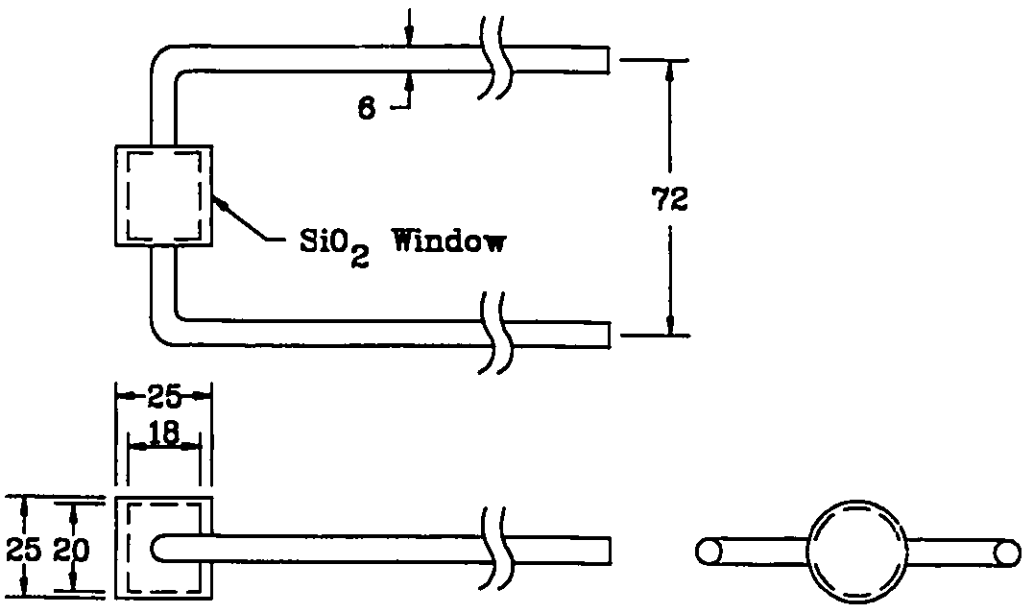

Figure 4.6-1 Large-diameter discharge envelope used for microwave characterization experiments. This envelope is constructed from fused silica windows and tubing. The bent gas-inlet arms allow the insertion and removal of the envelope without requiring the removal of the side walls of the resonator.

The experimental configuration is shown in Fig. 4.6-2. Light from the discharge passes through the window and propagates down the center of the end-wall slider. A 20-cm focal length lens is positioned 40 cm from the center of the discharge envelope; a translucent screen is positioned another 40 cm from the lens. Thus a 1:1 image of the discharge is projected on the screen, which is ruled with a 0.1" grid. A video camcorder equipped with a macro lens (Sanyo Zeema VM-ES88) is positioned 4 cm from the other side of the screen.

Only pure noble gases are used for these experiments; halogen-bearing discharges etch silica readily. The procedure is the same for each of gases (He, Ne, Ar, Kr, Xe). The discharge envelope is first evacuated and then filled with a few Torr of the appropriate gas.

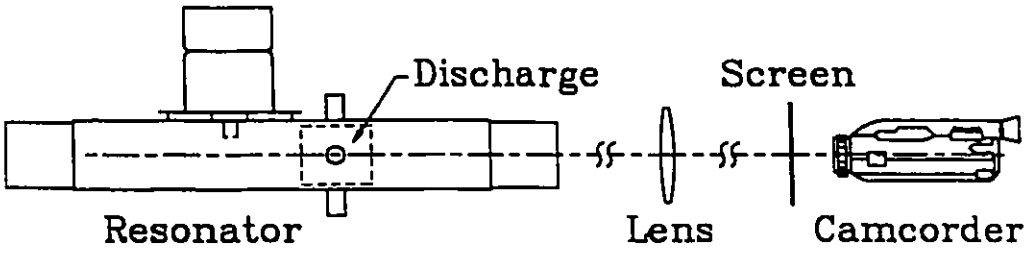

Figure 4.6-2 Microwave characterization experimental configuration. A 1:1 image of the discharge is projected on the translucent screen. The camcorder records this image superimposed on a grid that is printed on the screen. Sheath-thickness measurements are made directly from the screen of a playback monitor.

Power is applied to the magnetron, and a discharge is established. As usual, the anode current is set to 100 mA, which corresponds to a discharge power of approximately 210 W. The main vacuum valve is opened until the pressure in the envelope drops to 250 mTorr. With the camcorder recording, the pressure is slowly increased from 250 mTorr to several hundred Torr. Skin depth values (i.e., sheath thickness) are measured directly from the screen of a playback monitor at a later time.

The variation in skin depth for pressures ranging from 250 mTorr to 200 Torr is shown in Fig. 4.6-3 for all five gases. At the lowest pressure, there is no skin effect apparent for any of the gases. Therefore, a lower limit for the skin depth is set at 10 mm, which is the inside radius of the discharge envelope. Data was collected for pressures in excess of 200 Torr, but the sheath thickness in all cases is measured to be 0.4 mm. Smaller thicknesses cannot be observed under these conditions because of the length of the discharge envelope; the uncertainty in the object distance is effectively 9 mm, resulting in a slightly blurred image.

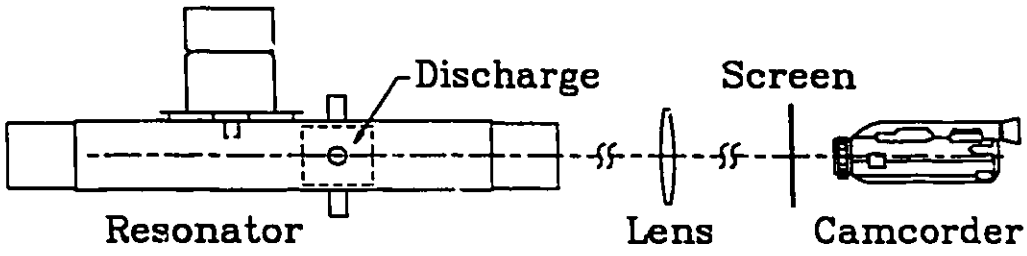

Figure 4.6-2 Microwave characterization experimental configuration. A 1:1 image of the discharge is projected on the translucent screen. The camcorder records this image superimposed on a grid that is printed on the screen. Sheath-thickness measurements are made directly from the screen of a playback monitor.

Power is applied to the magnetron, and a discharge is established. As usual, the anode current is set to 100 mA, which corresponds to a discharge power of approximately 210 W. The main vacuum valve is opened until the pressure in the envelope drops to 250 mTorr. With the camcorder recording, the pressure is slowly increased from 250 mTorr to several hundred Torr. Skin depth values (i.e., sheath thickness) are measured directly from the screen of a playback monitor at a later time.

The variation in skin depth for pressures ranging from 250 mTorr to 200 Torr is shown in Fig. 4.6-3 for all five gases. At the lowest pressure, there is no skin effect apparent for any of the gases. Therefore, a lower limit for the skin depth is set at 10 mm, which is the inside radius of the discharge envelope. Data was collected for pressures in excess of 200 Torr, but the sheath thickness in all cases is measured to be 0.4 mm. Smaller thicknesses cannot be observed under these conditions because of the length of the discharge envelope; the uncertainty in the object distance is effectively 9 mm, resulting in a slightly blurred image.

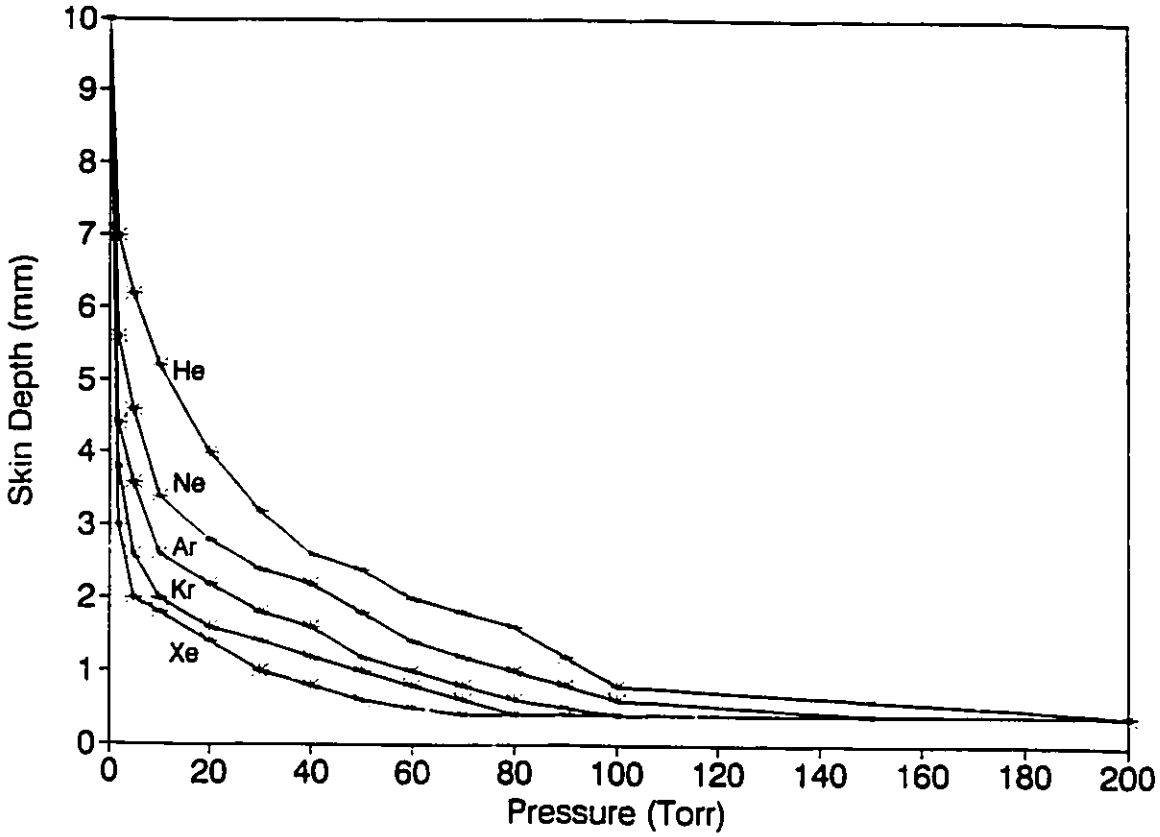

Figure 4.6-3 Skin depth versus pressure for the five lightest noble gases over the pressure range 0.25 Torr to 200 Torr.

Noble Gas Data

	Atomic radius[1] (Angstroms)	Cross-Section[2] (m^2)	Ionization Energy[3] (eV)
He	0.30	2.83×10^{-21}	24.6
Ne	0.37	4.30×10^{-21}	21.6
Ar	0.67	1.41×10^{-20}	15.8
Kr	0.85	2.27×10^{-20}	14.0
Xe	1.00	3.14×10^{-20}	12.1

[1]from *Handbook of Atomic Spectra* (Fraga, 1976)
[2]elastic scattering cross-section using hard-sphere model
[3]from *CRC Handbook of Chemistry and Physics* (Weast, 1986)

Table 4.6-1

The collision frequency for momentum transfer is calculated using

$$\nu = 5.31 \times 10^{28} \frac{Pq}{T_d} \sqrt{T_e} \quad \#/s, \qquad 4.6-1$$

where P is the pressure (in Torr), q is the cross-section (in m^2), T_e is the electron temperature and T_d is the discharge temperature (both in Kelvin). This relationship is derived from the ideal gas law. Table 4.6-1 gives pertinent data for the noble gases. The cross-sections are calculated using the hard-sphere model and the atomic radii that are listed. Consider the average electron energy (i.e., kT_e with k as Boltzmann's constant) to be equal to the ionization energy for the gas. Furthermore, the temperature of the discharge can be shown to be reasonably approximated by the wall temperature of the discharge envelope (Ballik, 1964). The wall temperature is measured with a thermocouple (Type K, Chromel-Alumel) and digital voltmeter (Hewlett-Packard E2373A), and is found to range from 375 K to 500 K for these experiments. Due to the high microwave power levels, the wall temperature cannot be measured while the power is on. Rather, the measurements must be made immediately

after the power is turned off in order to prevent damage to the voltmeter. For the purposes of the calculations in this chapter, the discharge temperature is taken to be 450 K. The variation of collision frequency with pressure and gas composition is shown in Fig. 4.6-4.

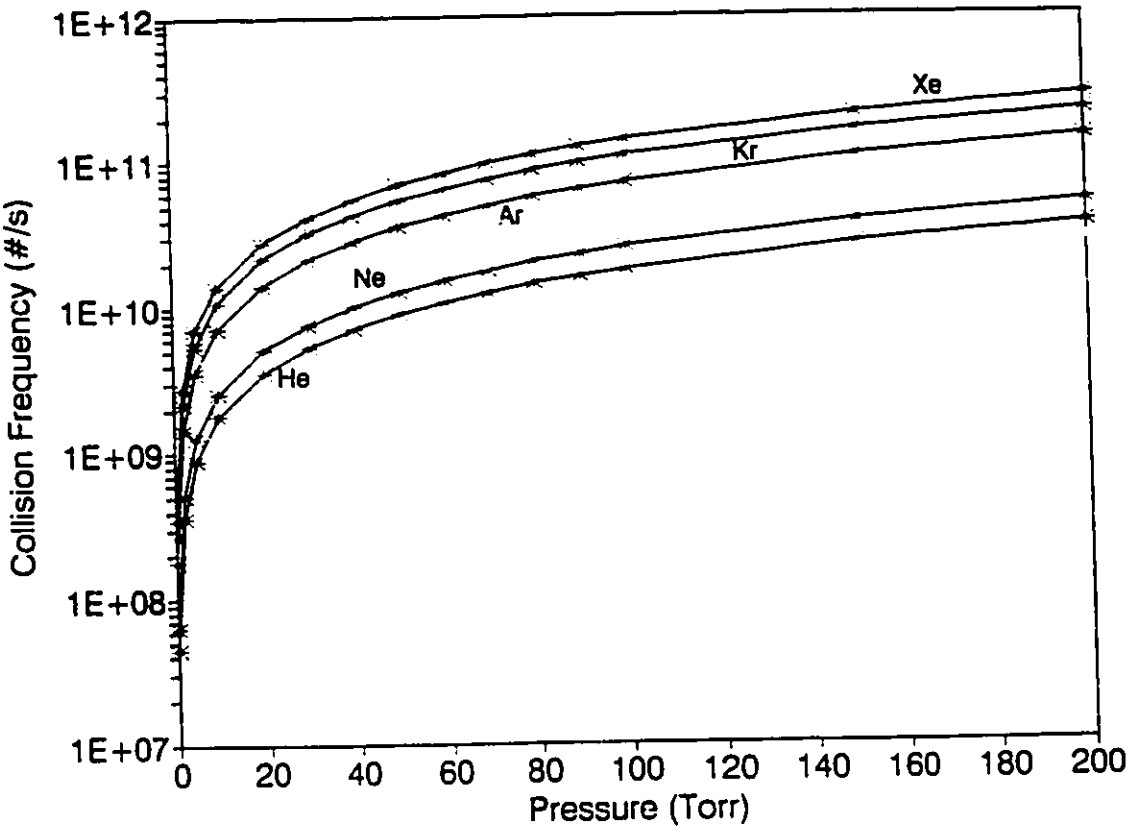

Figure 4.6-4 Collision frequency for momentum transfer versus pressure for the five lightest noble gases. The collision cross-sections are calculated from the hard-sphere model, and the discharge temperature is taken to be 450 K.

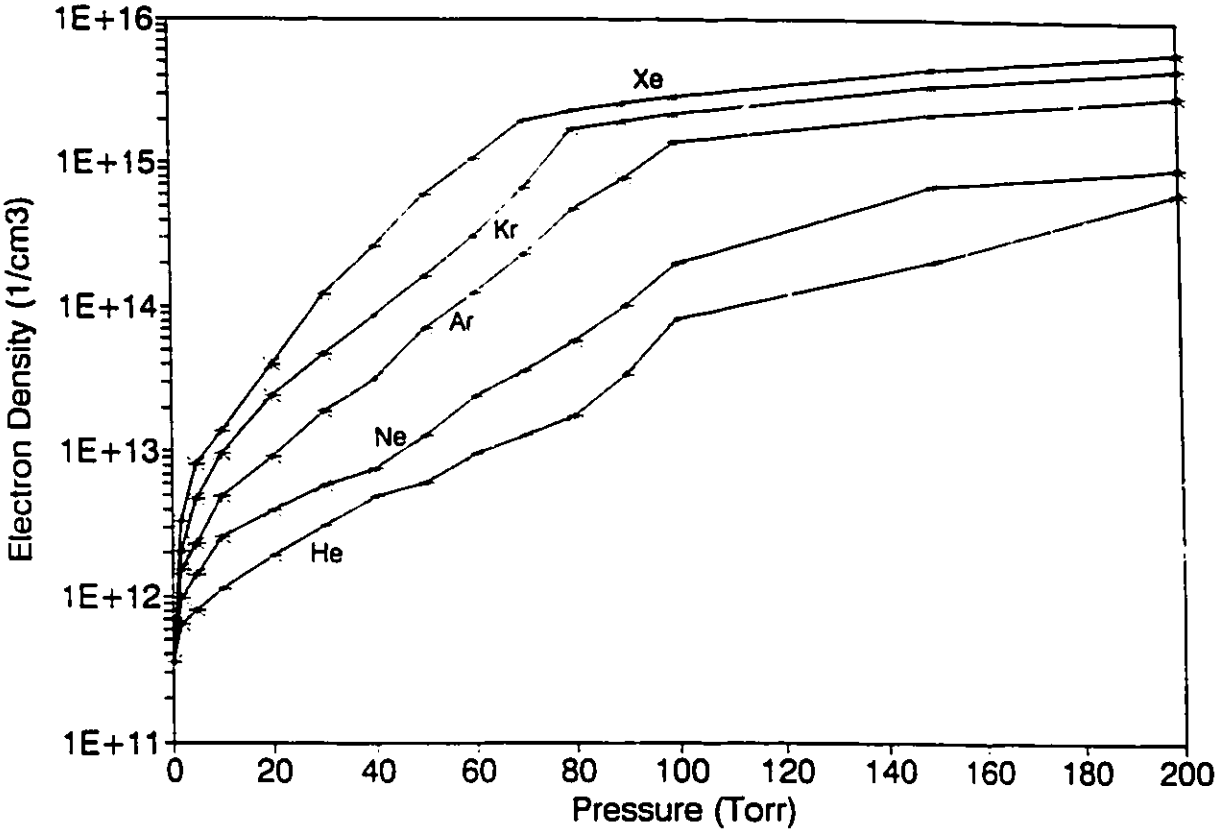

Figure 4.6-5 Electron density versus pressure for the five lightest noble gases.

Substituting the above data into Eq. 4.3-2, one obtains the variation of electron density with gas type and pressure. The resulting curves are shown in Fig. 4.6-5. Using the fact that the density of gas atoms can be written

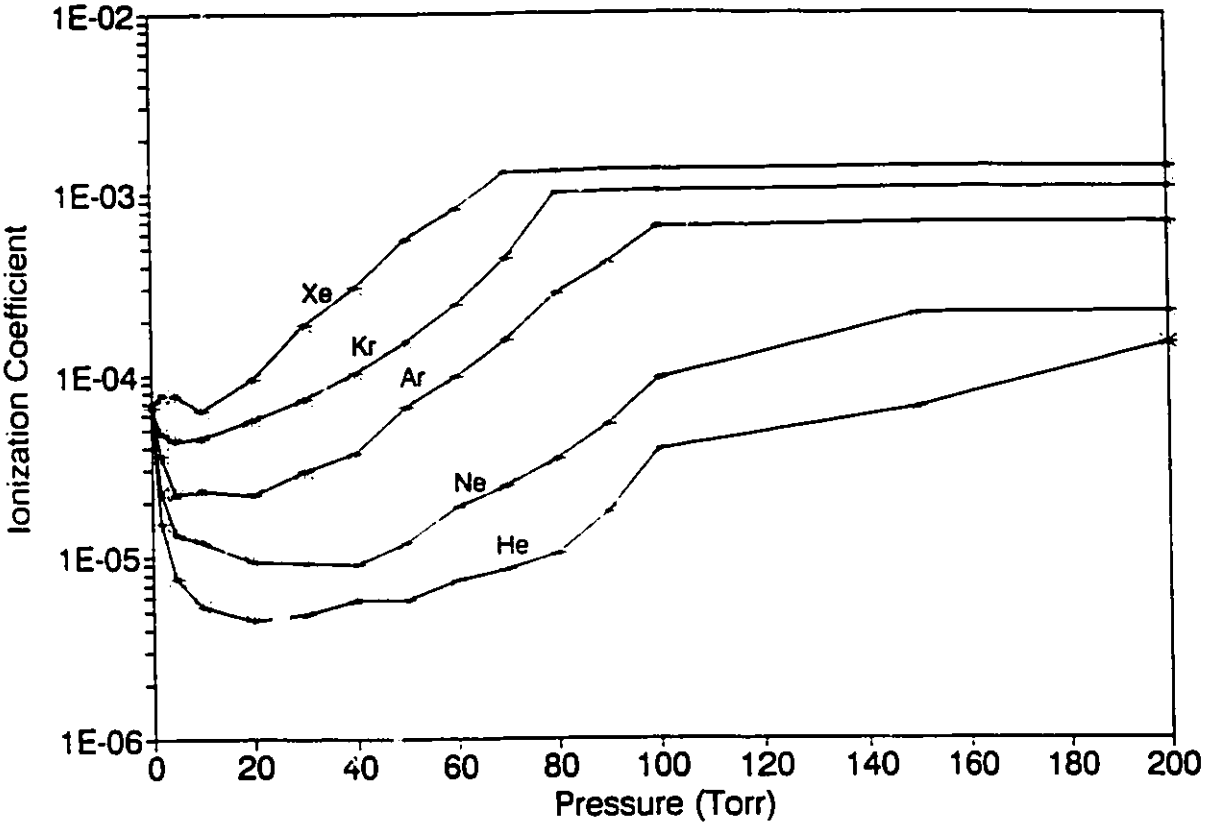

Figure 4.6-6 Ionization coefficient versus pressure for the five lightest noble gases.

$$N_a = 9.65 \times 10^{18} \frac{P}{T} \quad \#/cm^3, \qquad (4.6-2)$$

it is easy to calculate the ionization coefficient for the same conditions. These results are given in Fig. 4.6-6.

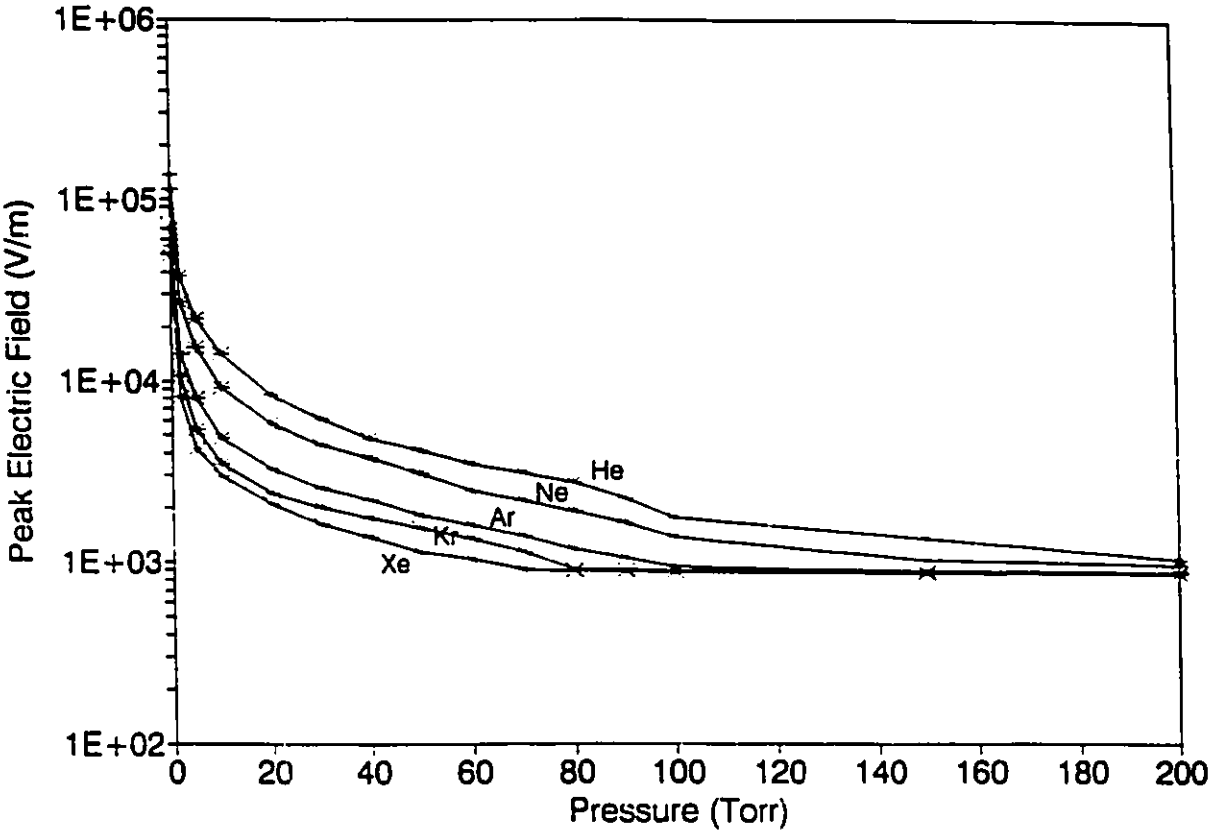

Figure 4.6-7 Peak electric-field intensity versus pressure in the discharge.

There is also sufficient information to calculate the peak electric field in the plasma. Under the conditions of interest (i.e., P < 200 Torr), the discharge is a cylindrical shell with an effective volume given by

$$V_{eff} = 18\pi(10^2 - (10-\delta)^2) \quad mm^3, \tag{4.6-3}$$

where the inside dimensions of the discharge envelope have been used. It can be shown from Eq. 4.4-5 that

$$E_0 = \sqrt{\frac{(\omega^2 + \nu^2) m P_{discharge}}{e^2 N_e \nu V_{eff}}}. \tag{4.6-4}$$

In the case of these experiments, the power absorbed by the discharge is taken to be 210 W. Evaluating Eq. 4.6-4 under these conditions yields the curves that are given in Fig. 4.6-7.

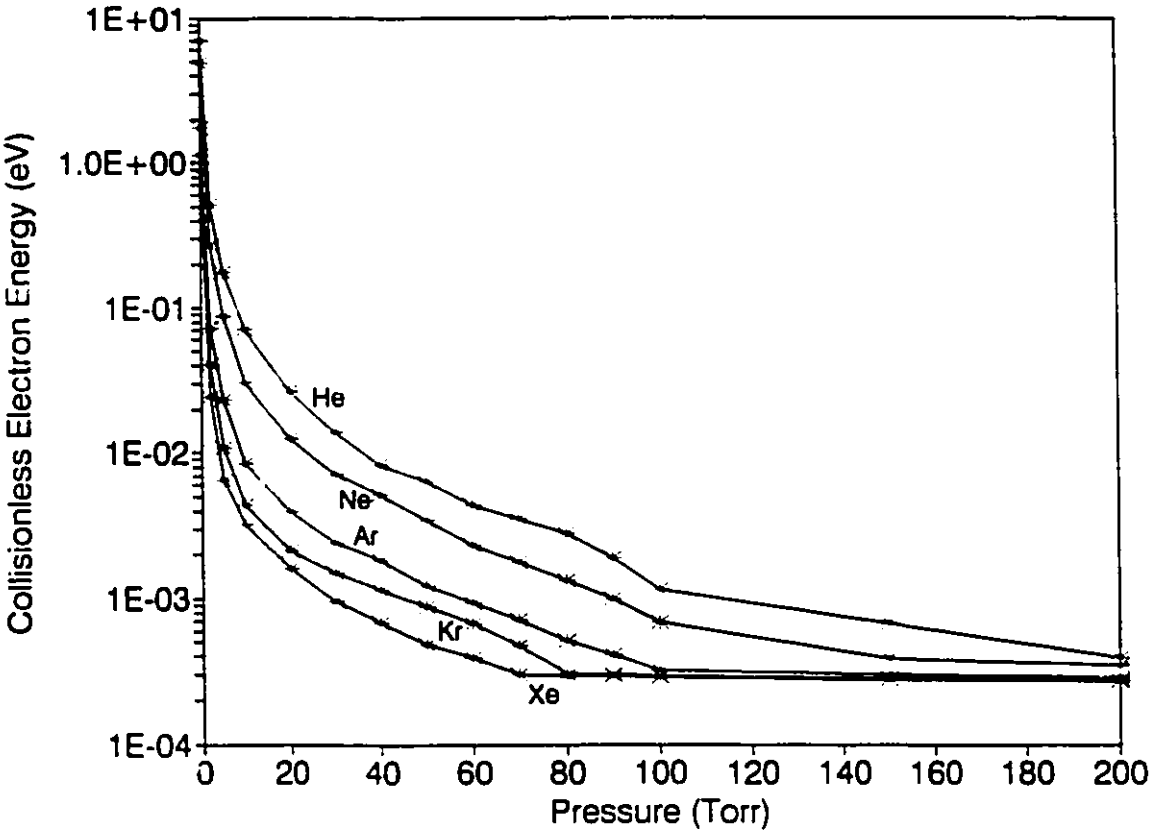

Figure 4.6-8 Collisionless electron energy based on peak electric-field intensity.

Using the above information, it is possible to calculate the collisionless electron energy from Eq. 4.5-1; these results are shown in Fig. 4.6-8. From Table 4.6-1, the ionization energies of the noble gases range from 12 eV (Xe) to 25 eV (He). Electron energies below these values are insufficient to ionize the gas. Visible photons have energies of in the range 1.8 eV to 3.1 eV, and so there must be electrons in a luminous discharge that have energies in excess of 1.8 eV. Thus it is clear from Fig. 4.6-8 that collisions must be taken into account

for all cases, except perhaps those involving the lowest pressures and lightest noble gases (i.e., He and Ne at 0.25 Torr). Referring to the collision frequency data (Fig. 4.6-4), it would appear that collisions cannot be safely neglected in electron energy calculations unless the collision frequency is one or more orders of magnitude below the applied microwave frequency. If this is not true, then dephasing collisions are required to allow the electrons to acquire more energy than the steady-state collisionless values.

Chapter 5

Continuous-Wave Excimer Fluorescence

In this chapter, details of the realization of microwave-excited excimer lamps are presented. Following a brief summary of the fundamental concepts of excimer chemistry and physics, the results of an extensive investigation of continuous-wave microwave-excited excimer fluorescence are reported. Rare-gas halide, homonuclear halogen and heteronuclear halogen systems are examined under comparable conditions, and ultraviolet spectra are given for these cases. The effects of total pressures and gas composition on fluorescence output are investigated for the more promising systems, and again the appropriate spectra are presented. An excellent general reference for excimer systems is the text edited by Rhodes (1982).

5.1 Introduction to Excimer Transitions

Originally, the term excimer (derived from excited dimer) was used to describe homonuclear compounds, such as Xe_2. The term exciplex (from excited complex) was

reserved for heteronuclear compounds, such as KrF. In order to be consistent with popular usage, this distinction is not made in this thesis. Both excimer and exciplex compounds and transitions are termed excimer.

Excimer transitions are characterized by an ionically or covalently bound upper state, and a dissociative or repulsive ground state. The excimer transitions of interest here are the rare-gas monohalide transitions and the molecular halogen transitions. Rare-gas excited dimers are not considered because their transition wavelengths cannot be detected with the equipment available for this research.

An intuitively-satisfying explanation of rare-gas monohalide excimer formation is given by Verdeyen (1981, p. 383). Consider a rare-gas atom (e.g., Xe) and a halogen atom (e.g., Cl). Because a rare gas is normally inert, it is clear that the potential energy of this system will increase without bound as the internuclear separation is reduced. This is the basis of the dissociative or repulsive ground state for an excimer transition. But if the Xe is excited, say through an electronic collision, then an electron is moved from its closed shell to the next available level. This makes the excited Xe atom "appear" (in the chemical sense) to be a Cs atom. Note that the excited Xe has not yet been ionized in this reaction. Now if the excited Xe atom is allowed to approach the Cl atom, at some critical distance the electron will be stripped from the Xe by the Cl, resulting in the formation of two oppositely-charged ions: Cl^- and excited Xe^*. Of course, these two ions are electrostatically attracted to each other, and the excited complex (i.e., excimer) XeCl is formed. This would be a stable compound, except for the fact that the excited Xe (and thus XeCl) has a short lifetime. Therefore, on the order of nanoseconds, the Xe^* ion returns to its ground state and retrieves its electron from the Cl^- ion. This is a radiative transition; energy is conserved by the creation of a UV photon. The Xe and Cl atoms are left in the repulsive ground state, and move away from each other in order to minimize the potential energy of the system.

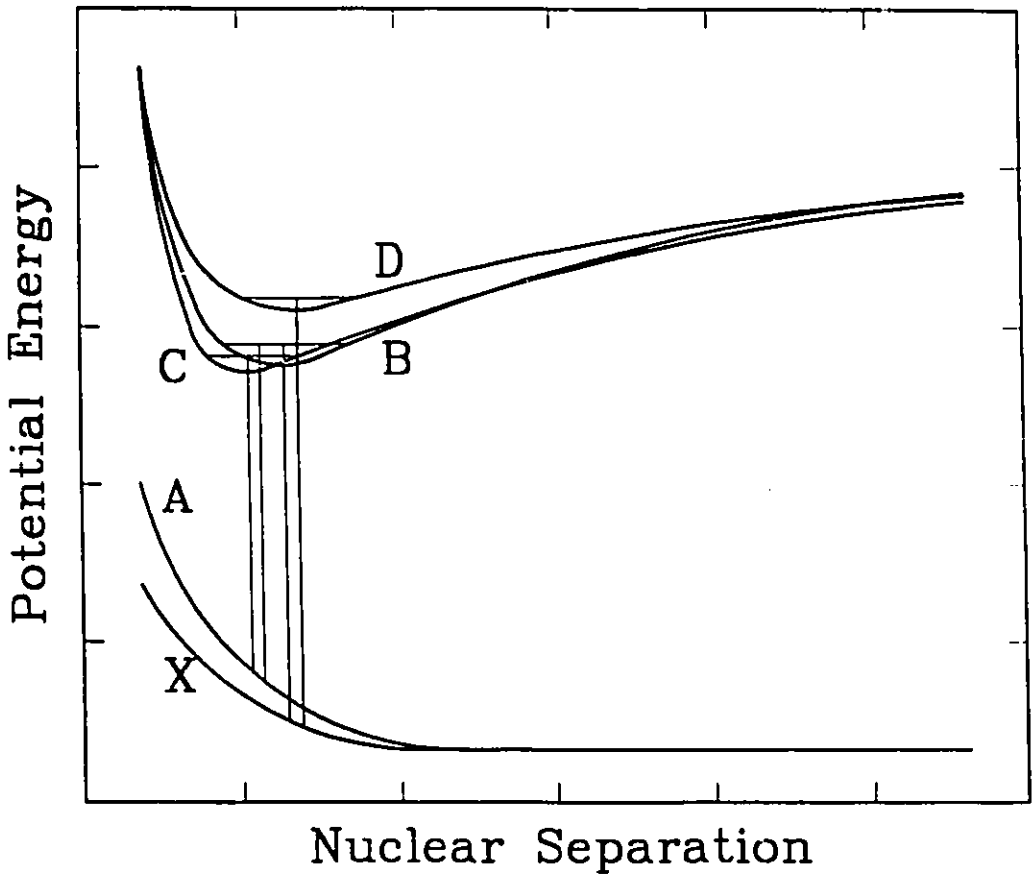

Figure 5.1-1 Potential energy as a function of internuclear spacing for a typical rare-gas monohalide molecule.

A generalized potential energy diagram (as a function of internuclear separation) for a typical rare-gas monohalide excimer is given in Fig. 5.1-1. In this figure, the thin horizontal lines indicate the lowest energy levels of the potential wells that are defined by the bound states. The vertical lines show the four possible radiative transitions to the dissociative ground states. Of these, the B→X transition is the most probable, and therefore the strongest.

Known Rare Gas and Halogen Transition Wavelengths

	F (nm)	Cl (nm)	Br (nm)	I (nm)	Transition
Ar	(185)[1]	-	-	-	D→X
	193	175	-	-	B→X
	(203)	-	-	-	C→A
	(204)	-	-	-	B→A
	285	245	-	-	Triatomic
Kr	220	200	-	-	D→X
	248	222	207	-	B→X
	275	240	222	-	C→A
	(272)	-	228	-	B→A
	420	325	318	-	Triatomic
Xe	264	236	221	203	D→X
	351	308	282	253	B→X
	460	345	300	265	C→A
	(410)	(340)	320	320	B→A
	610	490	440	375	Triatomic
I	[251][2]	[301]	[318]	343	
	{233}[3]	{297}	{317}		
Br	[226]	[276]	293		
	{215}	{275}			
Cl	[208]	258			
	{202}				
F	158				

[1]parentheses indicate theoretical values
[2]square brackets indicate arithmetic mean of homonuclear values
[3]brace brackets indicate geometric mean of homonuclear values

Table 5.1-1

Table 5.1-1 gives a summary of the known excimer transitions and their wavelengths; the top half deals with rare-gas halide transitions (triatomic species, such as Ar_2F, are included for completeness), the bottom half lists the molecular halogen transition wavelengths. There are no published reports of heteronuclear halogen fluorescence (e.g.,

from ICl or BrF). However, the formation of such compounds seems possible. The wavelengths given in the square and brace brackets are neither observed nor theoretical values for such species, but are simply the arithmetic and geometric means of the observed homonuclear wavelengths. These mean wavelengths are calculated to give approximate values for the possible fluorescence wavelengths of heteronuclear compounds.

Historically, the most extensive practical use of excimer transitions has been in pulsed lasers. Pumped by either electric discharges or e-beams, excimer lasers operate over a wavelength range that extends from the near-UV to the VUV. Because they can be reasonably efficient, and are scaleable to high average powers, these lasers are a very popular source of coherent UV radiation.

Pulsed operation is a requirement for excimer lasers; to date, there have been no reports of CW laser oscillation for these systems. One reason for this is that DC discharges are unstable at the high gas pressures that are required for efficient excimer formation. Laser operation can only be achieved using a relatively uniform discharge to excite the gain medium. Even with complicated preionization techniques and low-inductance discharge circuits, the volume discharge typically lasts less than 200 ns before it begins to collapse into a filamentary discharge. To date, the long st optical pulses from a XeCl laser are approximately 1.5 μs (Taylor and Leopold, 1985). Furthermore, fluorescence studies of krypton and fluorine in multimicrosecond discharges (Kumagai and Obara, 1988) have indicated that there is an intrinsic pulse length limitation in systems employing electrodes. There are indications that this limitation may result from a localized halogen depletion in the filaments that form following a volume discharge (Webb, 1990).

The observation of CW fluorescence in XeCl has been reported previously (Mikhkel'soo *et al*, 1987), but was attained by mixing independent streams of Xe and HCl that had been excited via two DC discharges. Although this achievement demonstrates that

there are no intrinsic limitations on pulse duration for this system, the technique employed is unnecessarily cumbersome, and therefore not very practical. Of more interest are the demonstrations of essentially CW fluorescence from KrF and ArF in a microwave-excited discharge (Kumagai and Obara; June, July and October, 1989). In this research, pulses having durations of many milliseconds were generated with efficiencies of several percent. In October of 1990, the first truly continuous microwave-excited excimer fluorescence was observed in a binary mixture of xenon and chlorine (Hassal and Ballik, 1990); analogous KrCl excimer fluorescence was achieved shortly afterwards (Hassal and Ballik, 1991). In both cases, excimer emission due to molecular chlorine was detected as well. The remainder of this chapter is devoted to describing the continuation and expansion of this research.

5.2 Experimental Overview

The microwave resonator is described more fully in Chapter 3. For convenience, its design and performance are summarized here. The 97-mm wide rectangular waveguide resonator operates in the TE_{102} mode. The magnetron source (Goldstar 2M223) is mounted on the top surface, probe coupled to the cavity. On the opposite side of the null plane, the discharge tube (6.5-mm inside diameter, fused-silica) extends through side walls of the cavity, parallel to the x-direction. Filter tubes are employed to minimize leakage and allow physical access to the interior of the cavity. The resonator is tuned by adjusting the position of the two end-wall sliders. The slider design incorporates thin-wall tubing to allow a good side view of the discharge. With no discharge tube, the quality factor of the apparatus is measured to be approximately 665. With the empty discharge tube in place, the Q falls to 620. Thus the coupling efficiency of the resonator/magnetron assembly is ~93%;, and the DC coupling efficiency is ~65%.

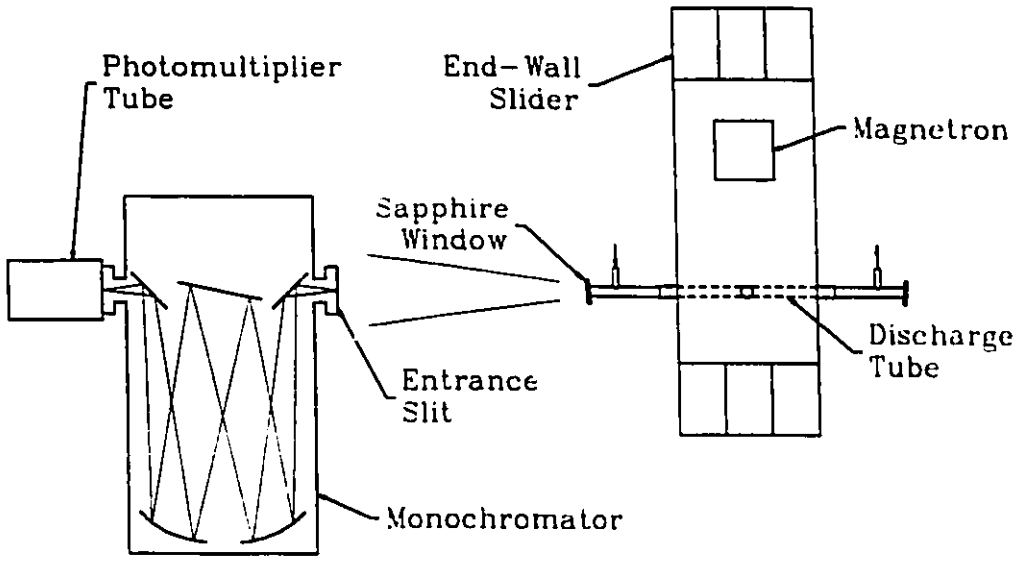

Figure 5.2-1 Schematic view of the experimental apparatus used for the fluorescence investigations. Light generated in the discharge propagates down the discharge tube, through the sapphire window and falls incident upon the entrance slit of the monochromator. The monochromator output is monitored using a photomultiplier tube.

Figure 5.2-1 gives a schematic overview of the experimental apparatus. Light from the plasma passes down the discharge tube and through a sapphire window (mounted 5° off axis to avoid reflections), to fall incident onto the entrance slit of a monochromator (Jarrell-Ash 82-487) equipped with a motor drive. The monochromator output is monitored using a UV photomultiplier (RCA 4831) connected to the y-input of an X-Y recorder (Hewlett-Packard 2FA). The spectral resolution of this system is better than 0.5 nm.

The desired gases are mixed in a 500-ml chamber before the discharge tube is filled (see Section 3.5 for more details). Pressure is measured using a piezo-resistive transducer (Motorola MPX 201AP). A DC power supply, in series with a 10-kΩ ballast resistor, provides 100 mA of current to the magnetron, with a corresponding input power of 320 W.

Assuming typical performance, the microwave power absorbed by the discharge is ~210 W, resulting in a input-power density in excess of 65 W/cm^3 in the discharge. The optical signal has less than 5% noise from all sources. Two fans are used to cool the apparatus; one blows across the cooling fins of the magnetron, the other is directed down the resonator through the end-wall sliders.

The following four sections deal with the investigation of excimer fluorescence from binary rare gas and halogen mixtures (Section 5.3), pure halogens (Section 5.4), and binary halogen mixtures (Section 5.5). In order to allow comparisons to be made among the data of these sections, all spectra are taken at a discharge power of 210 W and a total pressure of 5 Torr. Section 5.6 describes the results of more detailed investigations of systems that show particular promise. The instrument settings and parameters are indicated in Table 5.2-1.

Data for Recording Spectra

Figure	Gases (Conc.)	Total Pressure (Torr)	PMT Voltage (V)	Slit Widths (μm)	Recorder Scale (mV/in)	Wavelength Range (nm)
5.3-1	Ar(50%), Cl_2	5	900	25, 25	50	180-360
5.3-2	Ar(50%), SF_6	5	900	25, 25	10	180-360
5.3-3	Kr(50%), Br_2	5	900	25, 25	10	180-360
5.3-4	Kr(50%), Cl_2	5	900	25, 25	10	180-360
5.3-5	Kr(50%), SF_6	5	900	25, 25	10	180-360
5.3-6	Xe(50%), I_2	5	900	25, 25	10	180-360
5.3-7	Xe(50%), Br_2	5	900	25, 25	10	180-360
5.3-8	Xe(50%), Cl_2	5	900	25, 25	50	180-360
5.3-9	Xe(50%), SF_6	5	900	25, 25	10	180-360
5.4-1	I_2(100%)	5	900	25, 25	50	180-360
5.4-2	Br_2(100%)	5	900	25, 25	50	180-360
5.4-3	Cl_2(100%)	5	900	25, 25	10	180-360
5.4-4	SF_6(100%)	5	900	25, 25	50	180-360
5.5-1	I_2(50%), Br_2	5	900	25, 25	50	180-360
5.5-2	I_2(50%), Cl_2	5	900	25, 25	50	180-360
5.5-3	I_2(50%), SF_6	5	900	25, 25	50	180-360
5.5-4	Br_2(50%), Cl_2	5	900	25, 25	10	180-360
5.5-5	Br_2(50%), SF_6	5	900	25, 25	50	180-360
5.5-6	Cl_2(50%), SF_6	5	900	25, 25	10	180-360
5.6-1	Kr, Cl_2	0-100	500	50, 100	100	220
5.6-2a	Kr(80%), Cl_2	50	600	50, 100	100	200-320
5.6-2b	Kr(60%), Cl_2	30	600	50, 100	100	200-320
5.6-2c	Kr(40%), Cl_2	10	600	50, 100	100	200-320
5.6-2d	Kr(20%), Cl_2	30	600	50, 100	100	200-320
5.6-3	Xe, Cl_2	0-100	610	50[1], 100	100	308
5.6-4a	Xe(80%), Cl_2	75	610	50[1], 100	100	200-320
5.6-4b	Xe(60%), Cl_2	40	610	50[1], 100	100	200-320
5.6-4c	Xe(40%), Cl_2	40	610	50[1], 100	100	200-320
5.6-4d	Xe(20%), Cl_2	14	610	50[1], 100	100	200-320
5.6-5	Cl_2(100%)	0-100	700	50, 100	100	258
5.6-6	Cl_2(100%)	35	700	50, 100	100	200-320

[1]with a fused-silica condensing lens (f = 5 cm)

Table 5.2-1

5.3 Rare-Gas Monohalide Fluorescence

Using the gases available, there are nine distinct 50:50 binary mixtures. Excimer fluorescence (if present) is expected to occur at the wavelengths given in Table 5.1-1. Each of these mixtures is discussed individually.

Argon and Chlorine Binary Mixture (Fig. 5.3-1)

In this case, the B→X transition wavelength is at 175 nm, and is therefore outside the detectable range of the photomultiplier. The only other previously observed fluorescence is due to the triatomic excimer Ar_2Cl, and occurs at 245 nm. There is a small feature near this wavelength in Fig. 5.3-1, but it is not possible to conclusively attribute it to the triatomic transition. The strongest feature of this spectrum is the transition at 258 nm, which is due to molecular chlorine.

Argon and Sulfur Hexafluoride Binary Mixture (Fig. 5.3-2)

For this mixture the B→X wavelength is 193 nm, which is just within the detectable range. From the figure, there is no fluorescence evident near this wavelength. Furthermore, none of the other excimer transitions are apparent. The spectral content of this figure is most likely due to SF_6 and its dissociation products.

Krypton and Bromine Binary Mixture (Fig 5.3-3)

From the figure, there is a very small peak evident near 207 nm, and a slightly larger one near 222 nm; these wavelengths correspond to the B→X and C→A transitions of KrBr. The strongest feature in this spectrum is the 293-nm transition due to molecular bromine.

Krypton and Chlorine Binary Mixture (Fig 5.3-4)

The 222-nm KrCl B→X transition is obviously the most prominent feature in this mixture. In addition, there is a small feature near 200 nm that may be due to the D→X transition, although this assignment is not conclusive. No other excimer transitions are apparent.

Krypton and Sulfur Hexafluoride Binary Mixture (Fig. 5.3-5)

As in the case of the Ar and SF_6 mixture, most of the spectral content is probably due to the dissociation products of SF_6. Because this overlaps the excimer wavelengths, it is impossible to detect the excimer transitions.

Xenon and Iodine Binary Mixture (Fig. 5.3-6)

Although there are small features near 253 nm and 265 nm, these cannot be attributed to excimer transitions. A comparison with the spectrum for pure iodine (Fig. 5.4-1) indicates that they are part of the I_2 spectral structure.

Xenon and Bromine Binary Mixture (Fig. 5.3-7)

Again, it is likely that any overlap between features of this spectrum and the transitions due to XeBr (e.g., the 282-nm B→X transition) are coincidental.

Xenon and Chlorine Binary Mixture (Fig. 5.3-8)

The strongest feature of this spectrum is due to the 308-nm XeCl B→X transition. The 236-nm D→X transition is also readily apparent, as is the 258-nm molecular chlorine transition.

Xenon and Sulfur Hexafluoride Binary Mixture (Fig. 5.3-9)

For this mixture, there is a spectrum consisting of many weak lines that overlap the region of interest; it is impossible to detect any that are due to XeF excimer transitions.

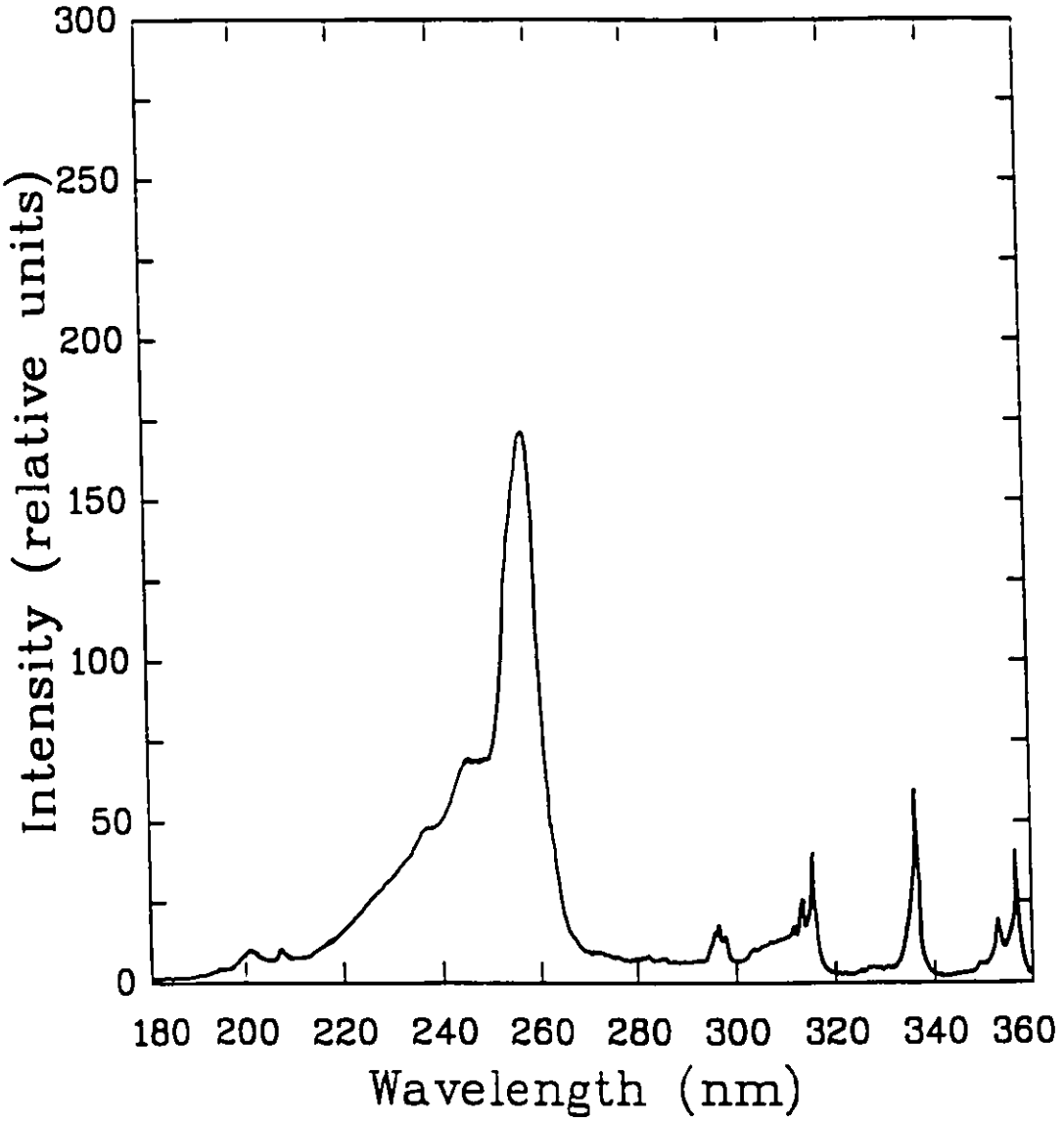

Figure 5.3-1 Fluorescence spectrum for a 50:50 Ar:Cl_2 mixture at a total pressure of 5 Torr.

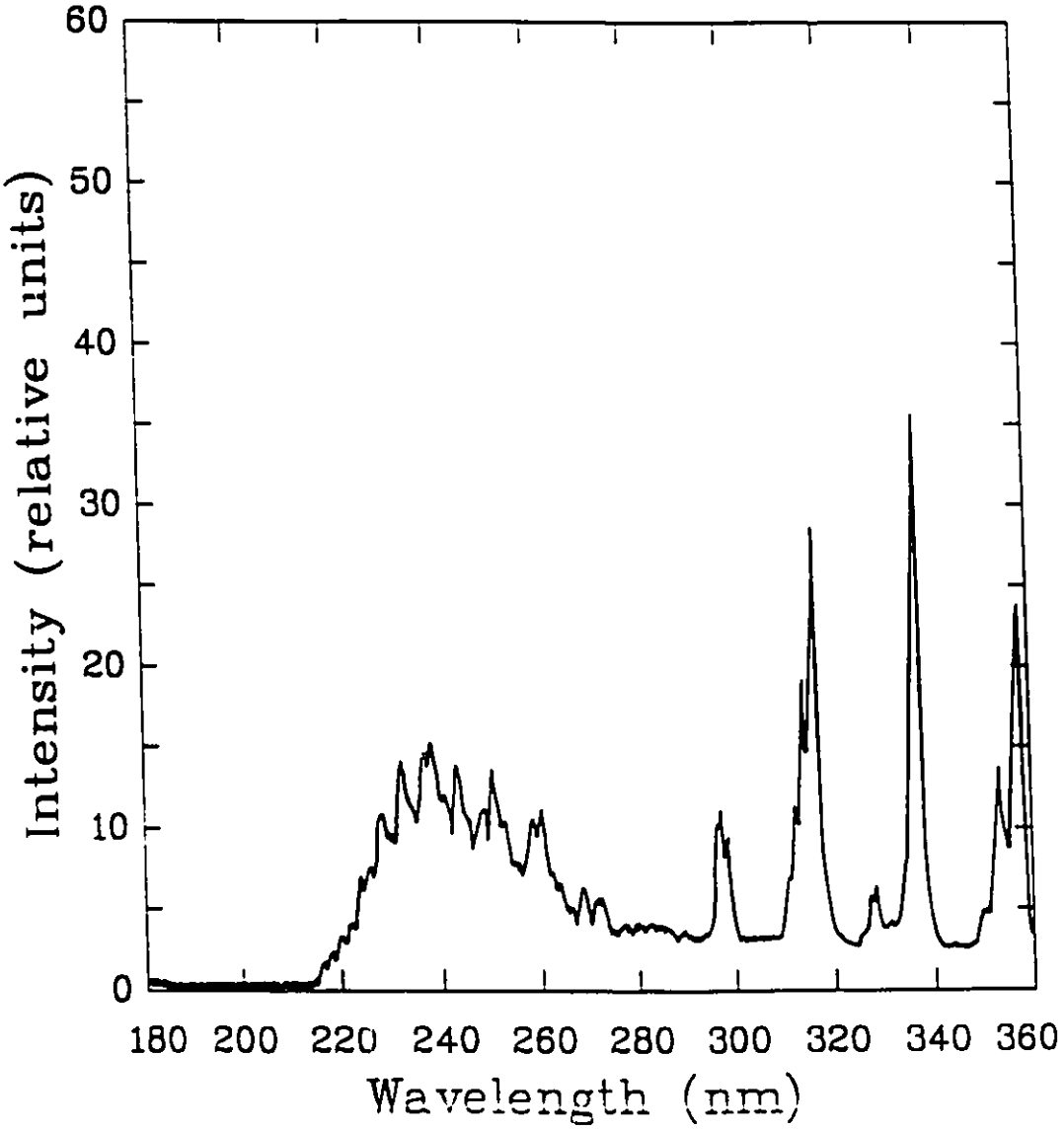

Figure 5.3-2 Fluorescence spectrum for a 50:50 Ar:SF_6 mixture at a total pressure of 5 Torr.

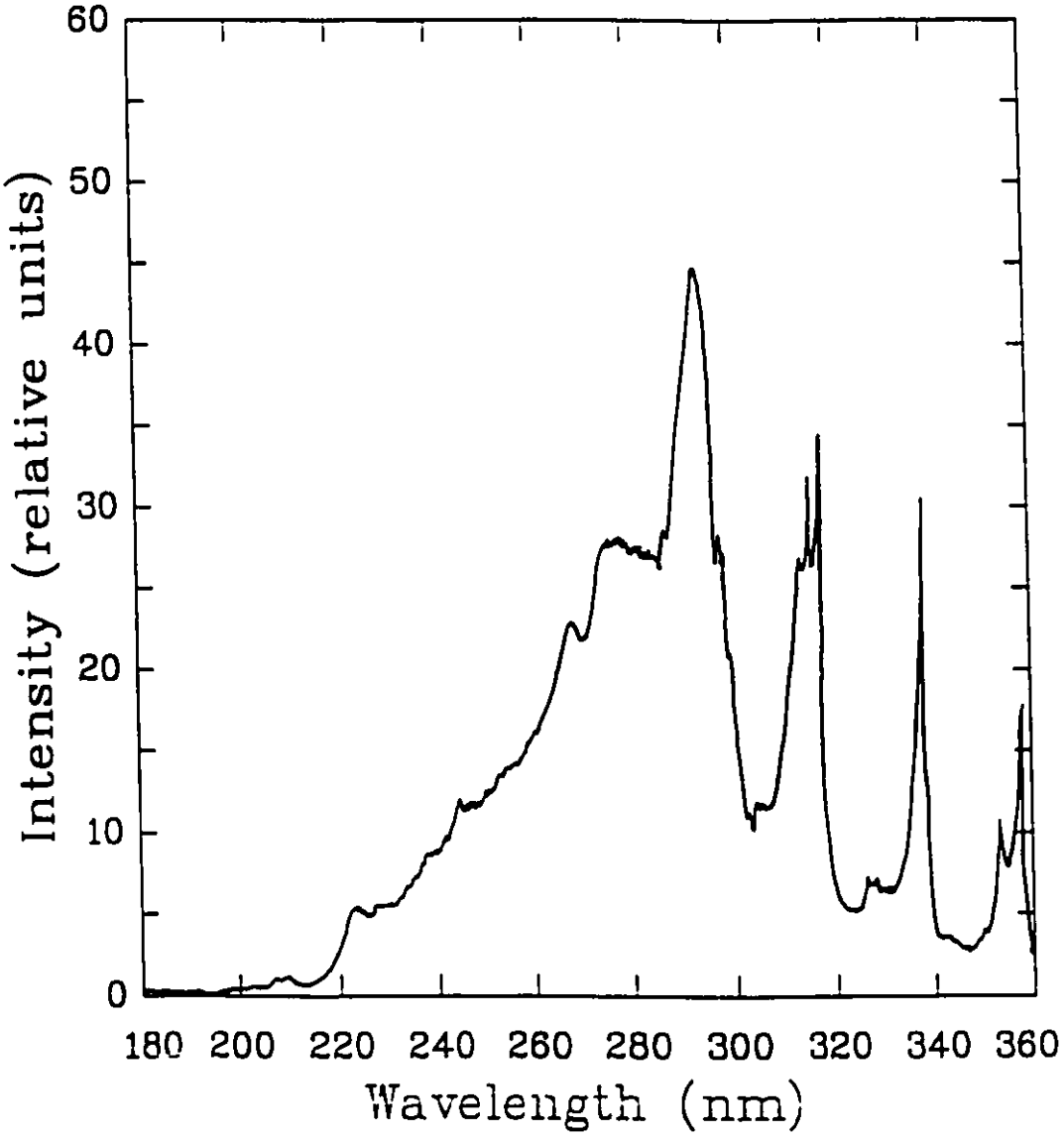

Figure 5.3-3 Fluorescence spectrum for a 50:50 Kr:Br_2 mixture at a total pressure of 5 Torr.

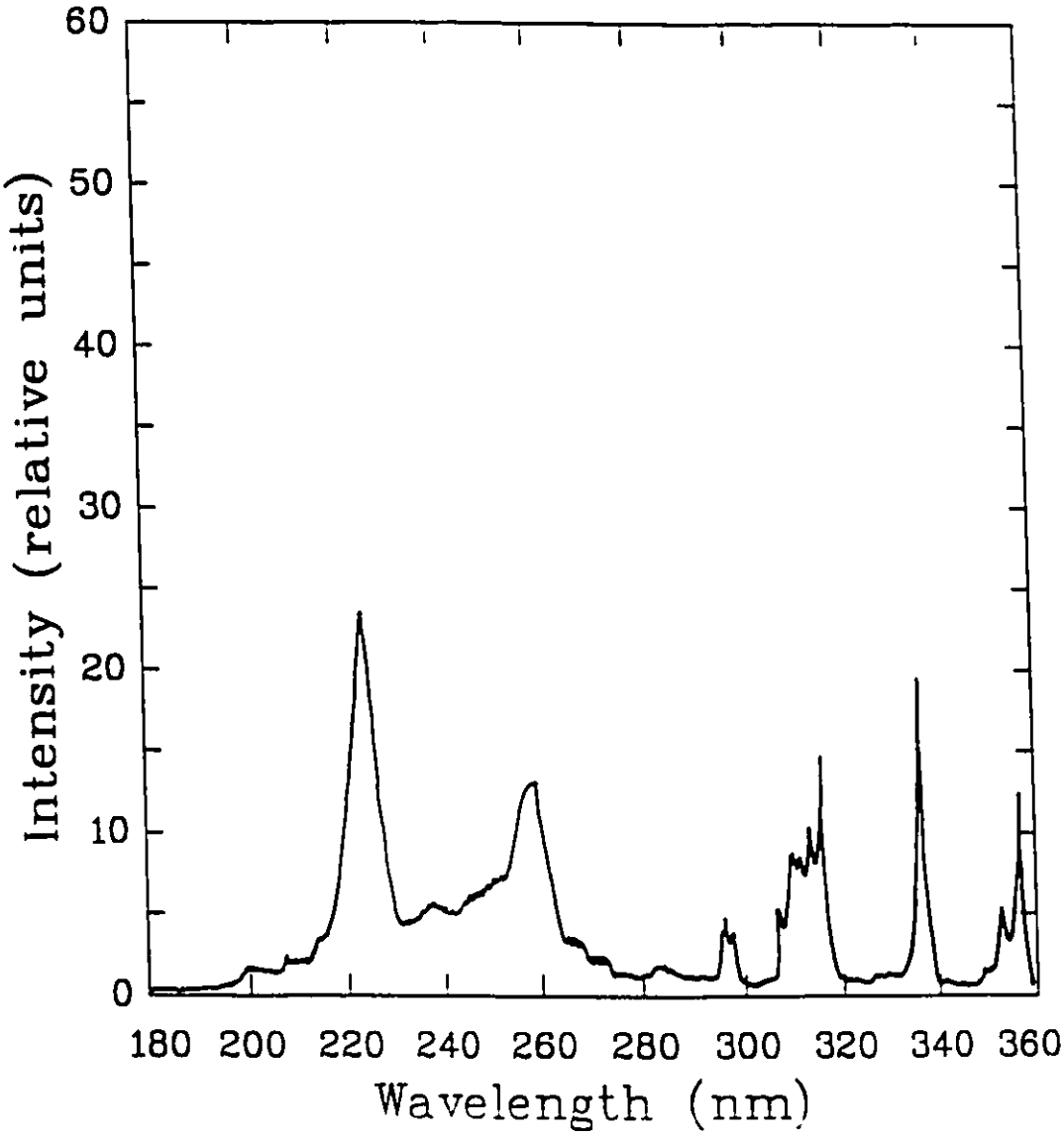

Figure 5.3-4 Fluorescence spectrum for a 50:50 Kr:Cl_2 mixture at a total pressure of 5 Torr.

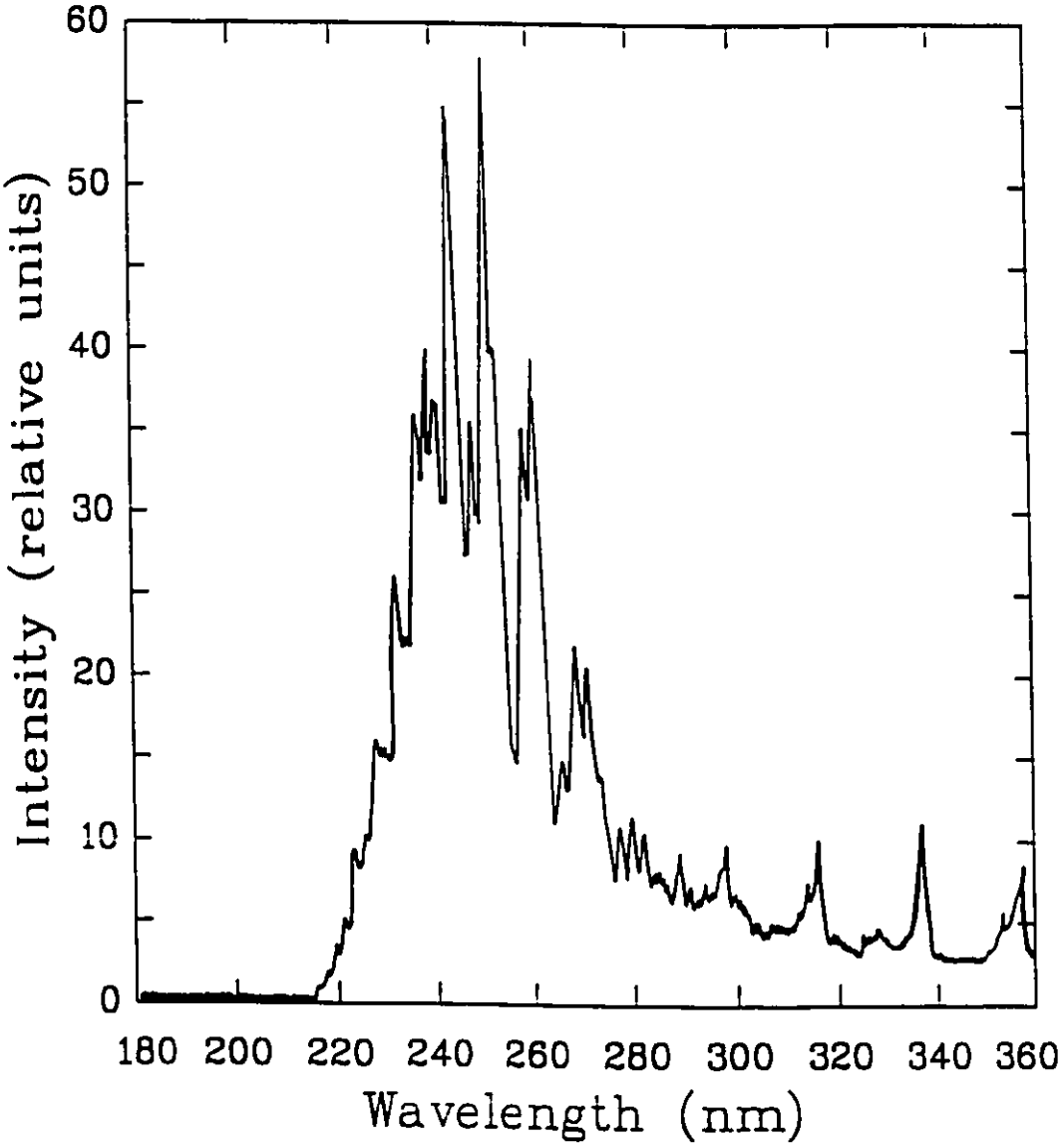

Figure 5.3-5 Fluorescence spectrum for a 50:50 Kr:SF_6 mixture at a total pressure of 5 Torr.

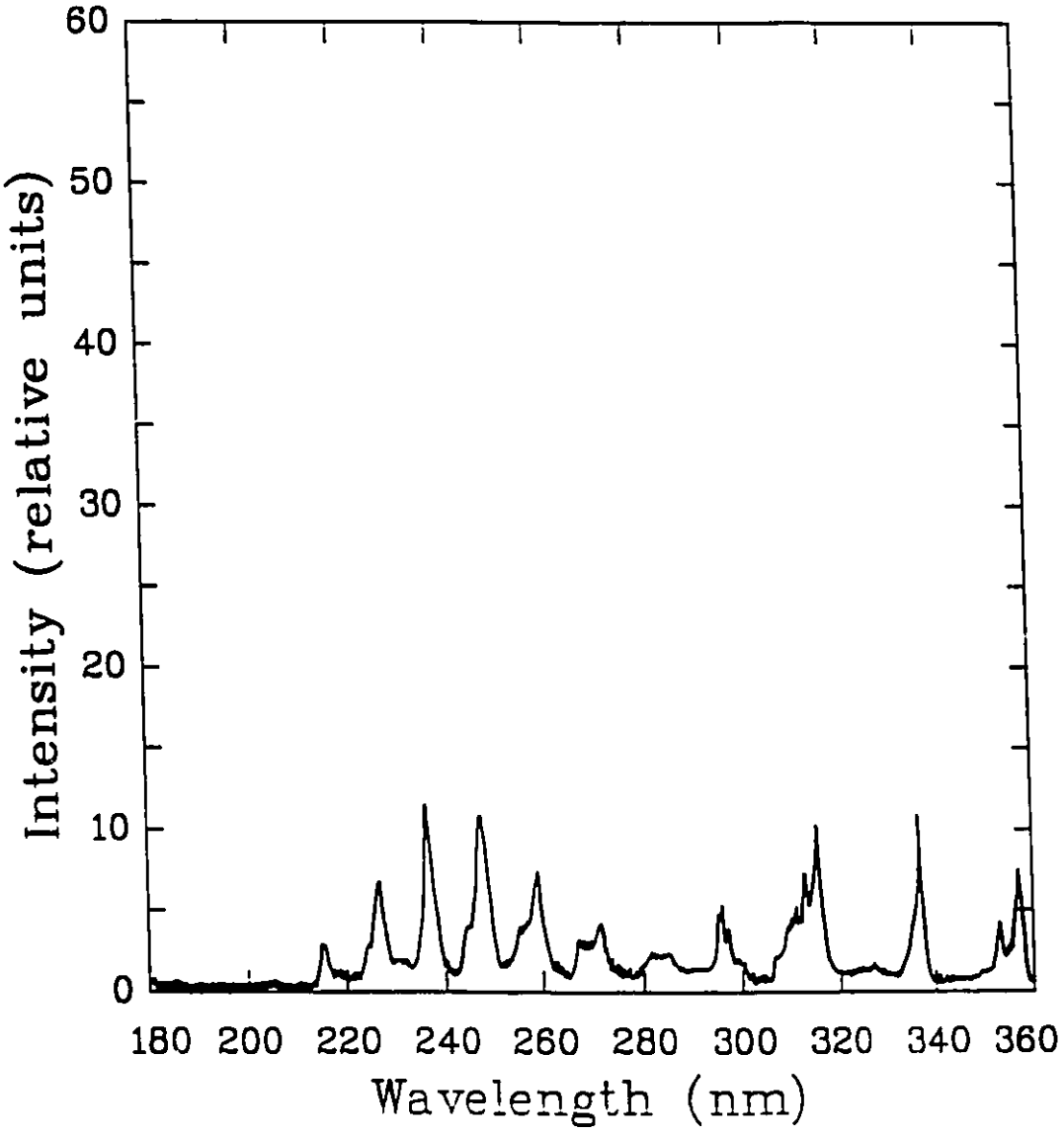

Figure 5.3-6 Fluorescence spectrum for a 50:50 Xe:I_2 mixture at a total pressure of 5 Torr.

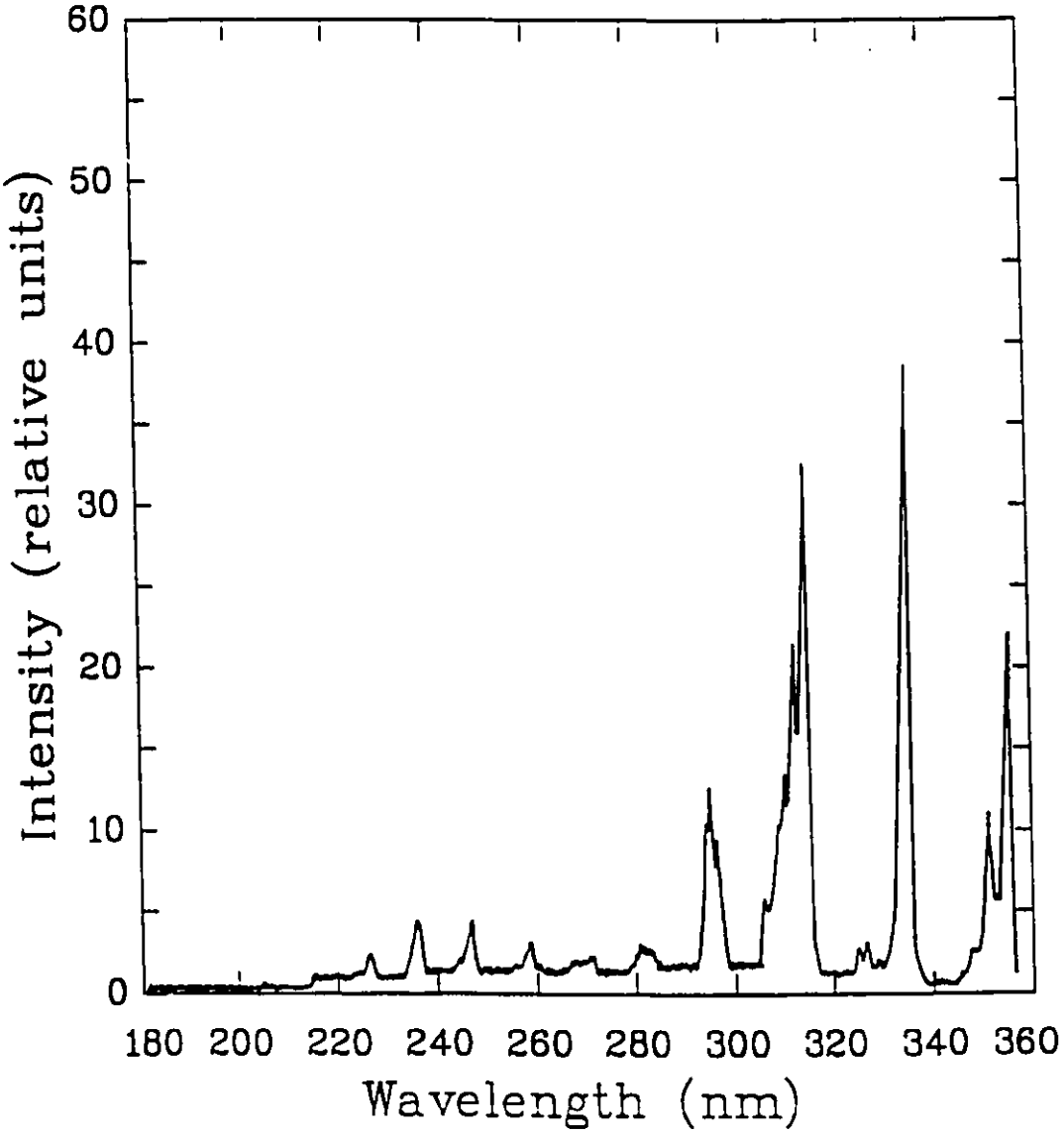

Figure 5.3-7 Fluorescence spectrum for a 50:50 Xe:Br_2 mixture at a total pressure of 5 Torr.

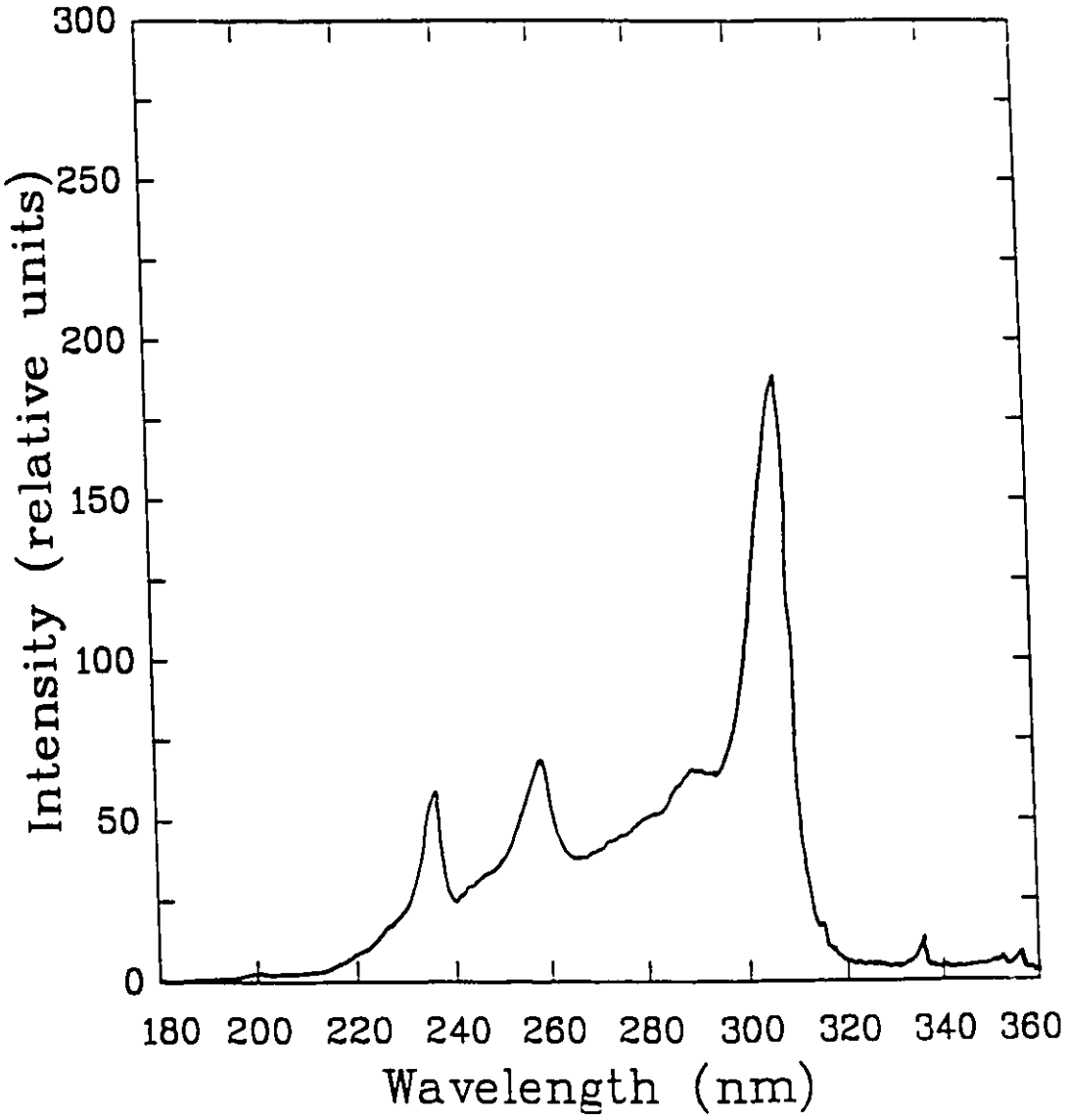

Figure 5.3-8 Fluorescence spectrum for a 50:50 $Xe:Cl_2$ mixture at a total pressure of 5 Torr.

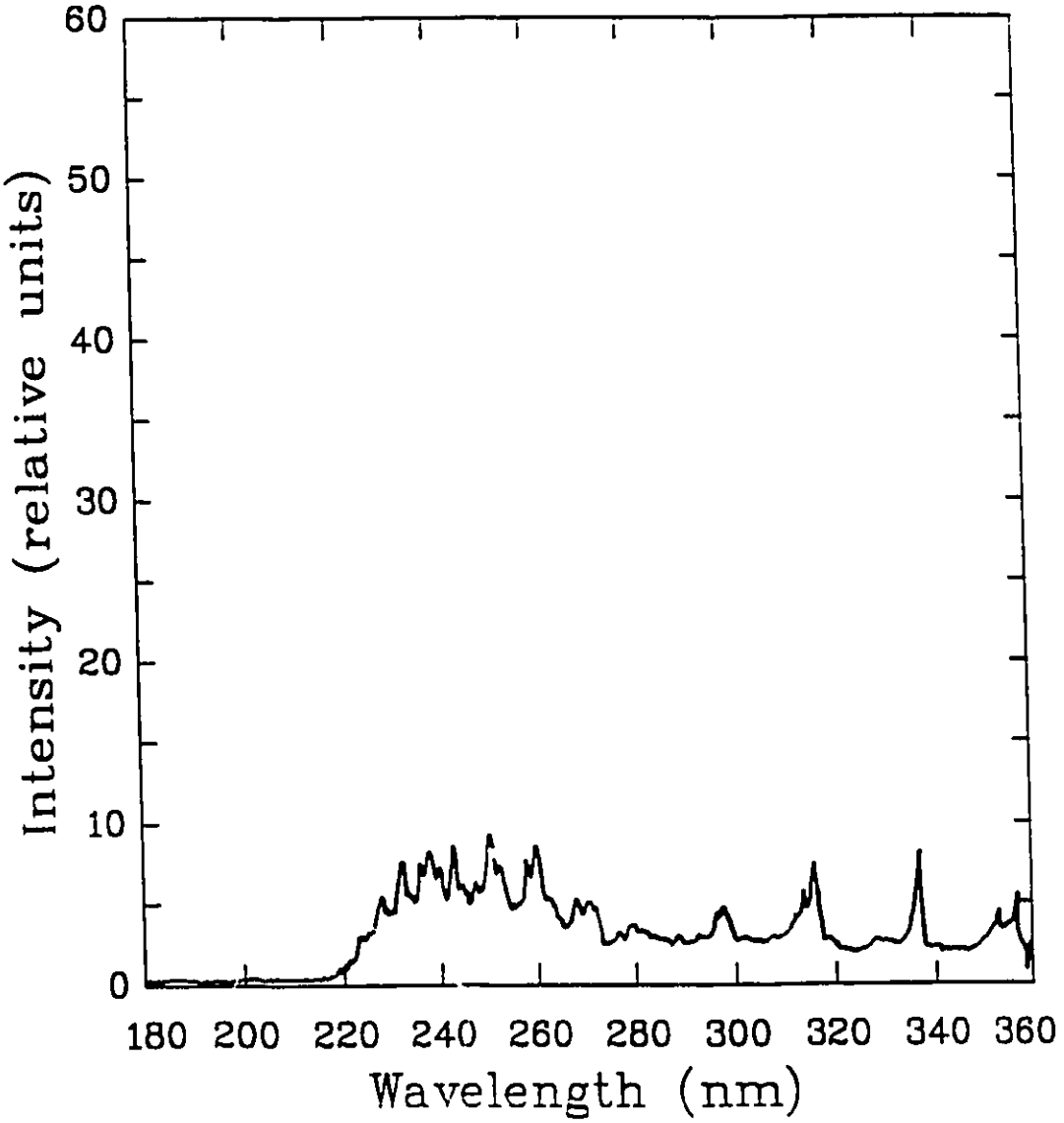

Figure 5.3-9 Fluorescence spectrum for a 50:50 Xe:SF_6 mixture at a total pressure of 5 Torr.

5.4 Homonuclear Halogen Fluorescence

Each of the four halogen (or halogen-bearing, in the case of SF_6) gases are examined for homonuclear molecular excimer fluorescence.

Pure Iodine (Fig. 5.4-1)

The published value for the molecular I_2 transition is near 343 nm (Hays *et al*, 1976). The spectrum given here shows over twenty well-resolved transitions, the strongest of which has a wavelength near 337 nm. It is unlikely that any of these peaks are due to excimer fluorescence.

Pure Bromine (Fig. 5.4-2)

The most prominent feature of this spectrum is the 293-nm molecular Br_2 transition, which has a full-width at half-maximum (FWHM) of ~8 nm. Note the broad fluorescence between 220 nm and 285 nm.

Pure Chlorine (Fig. 5.4-3)

The most prominent feature is the excimer transition, which is due to molecular Cl_2 and has a wavelength of 258 nm.

Pure Sulfur Hexafluoride (Fig. 5.4-4)

The expected transition wavelength (158 nm) is well beyond the detectable range of the photomultiplier tube. This spectrum is included only for completeness.

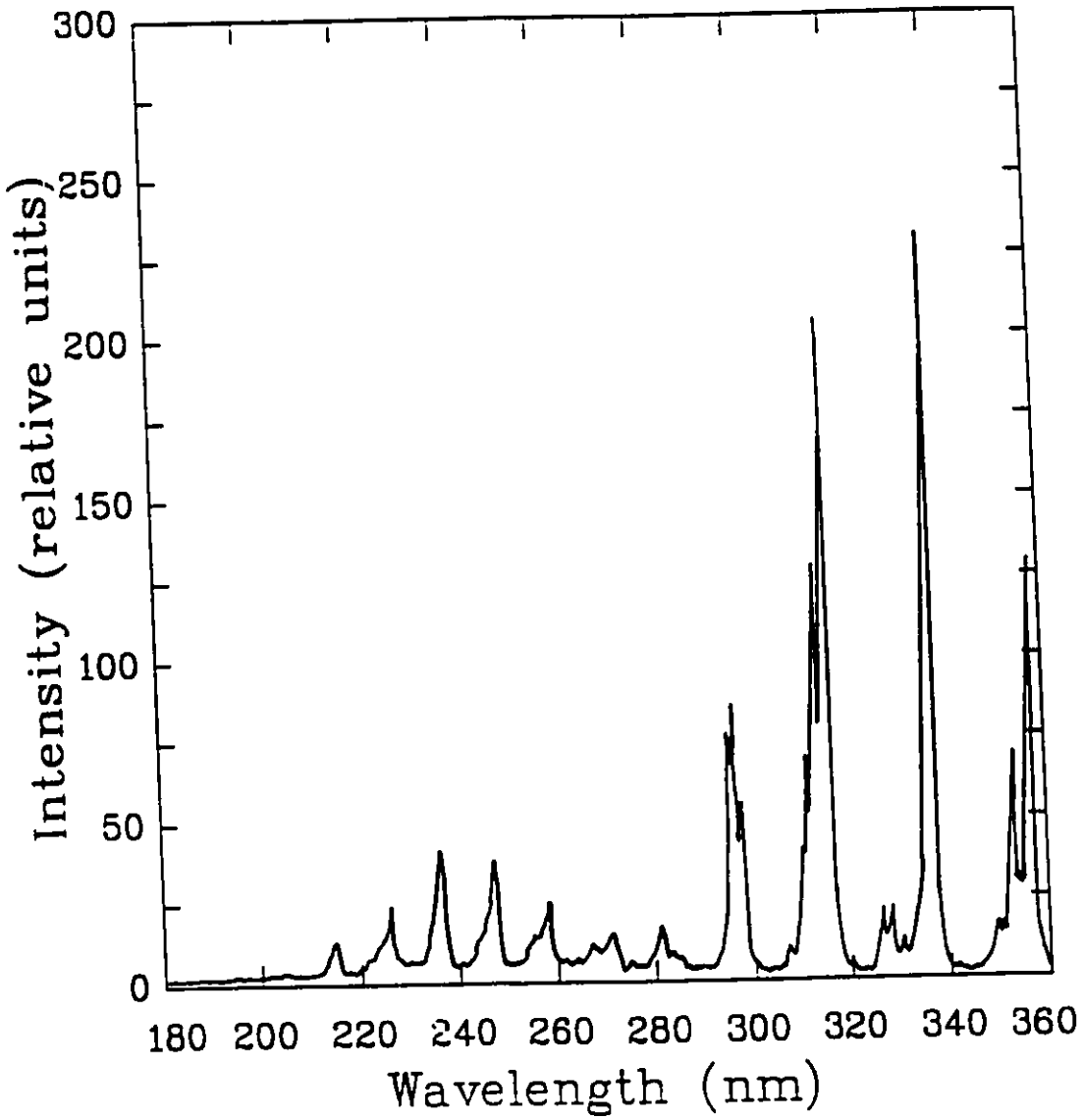

Figure 5.4-1 Fluorescence spectrum for I_2 at a total pressure of 5 Torr.

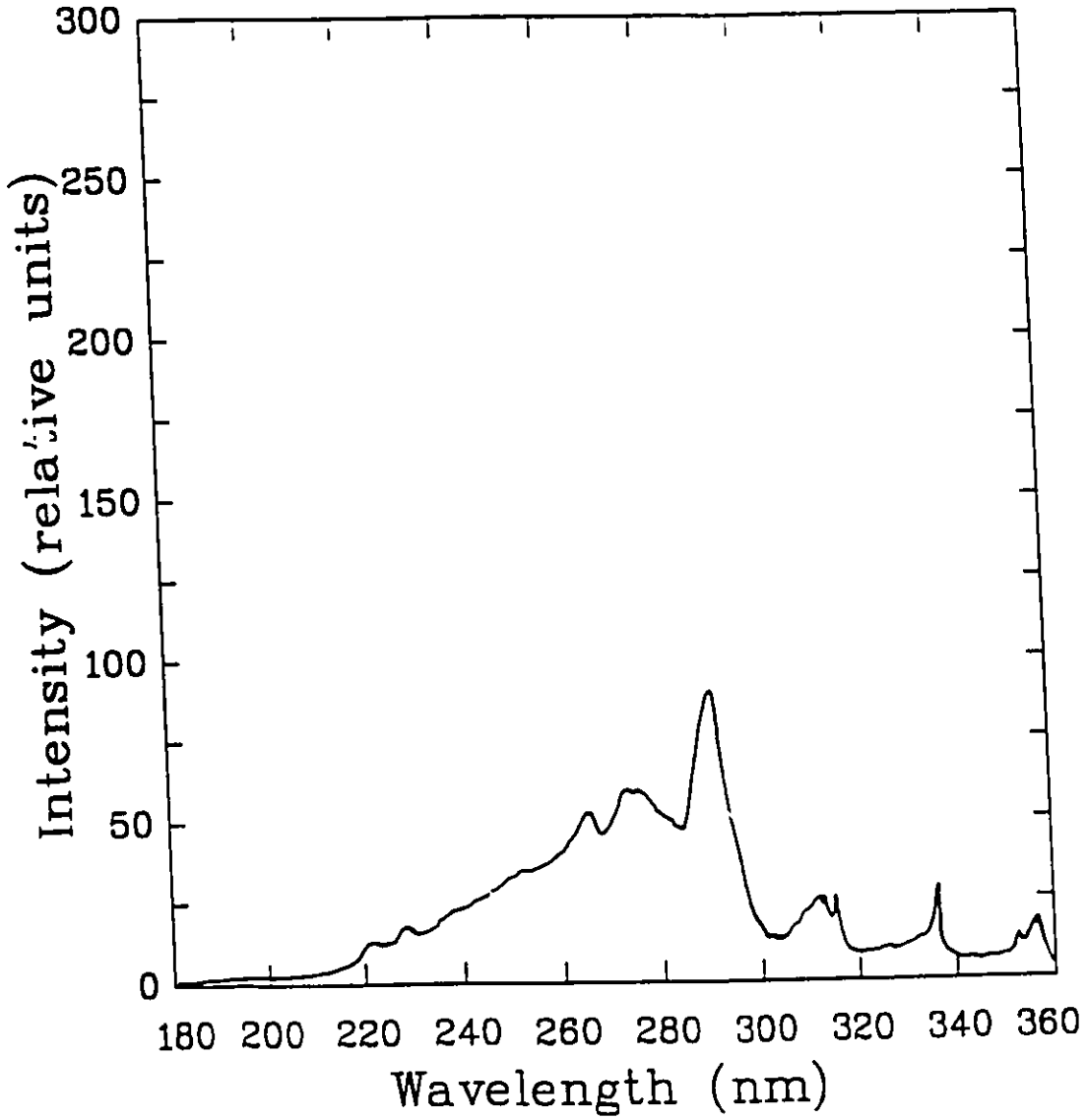

Figure 5.4-3 Fluorescence spectrum for Br_2 at a total pressure of 5 Torr.

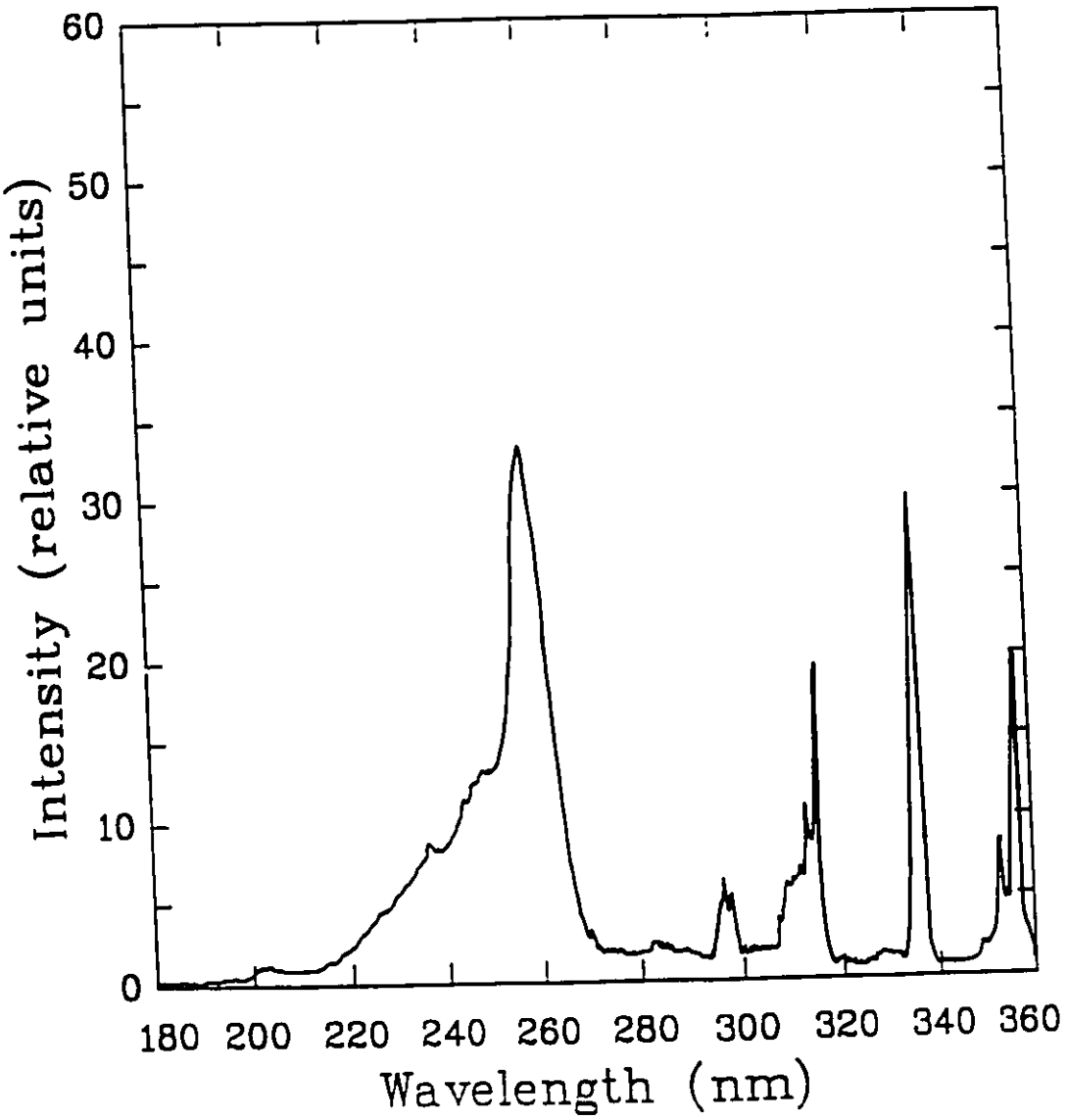

Figure 5.4-2 Fluorescence spectrum for Cl_2 at a total pressure of 5 Torr.

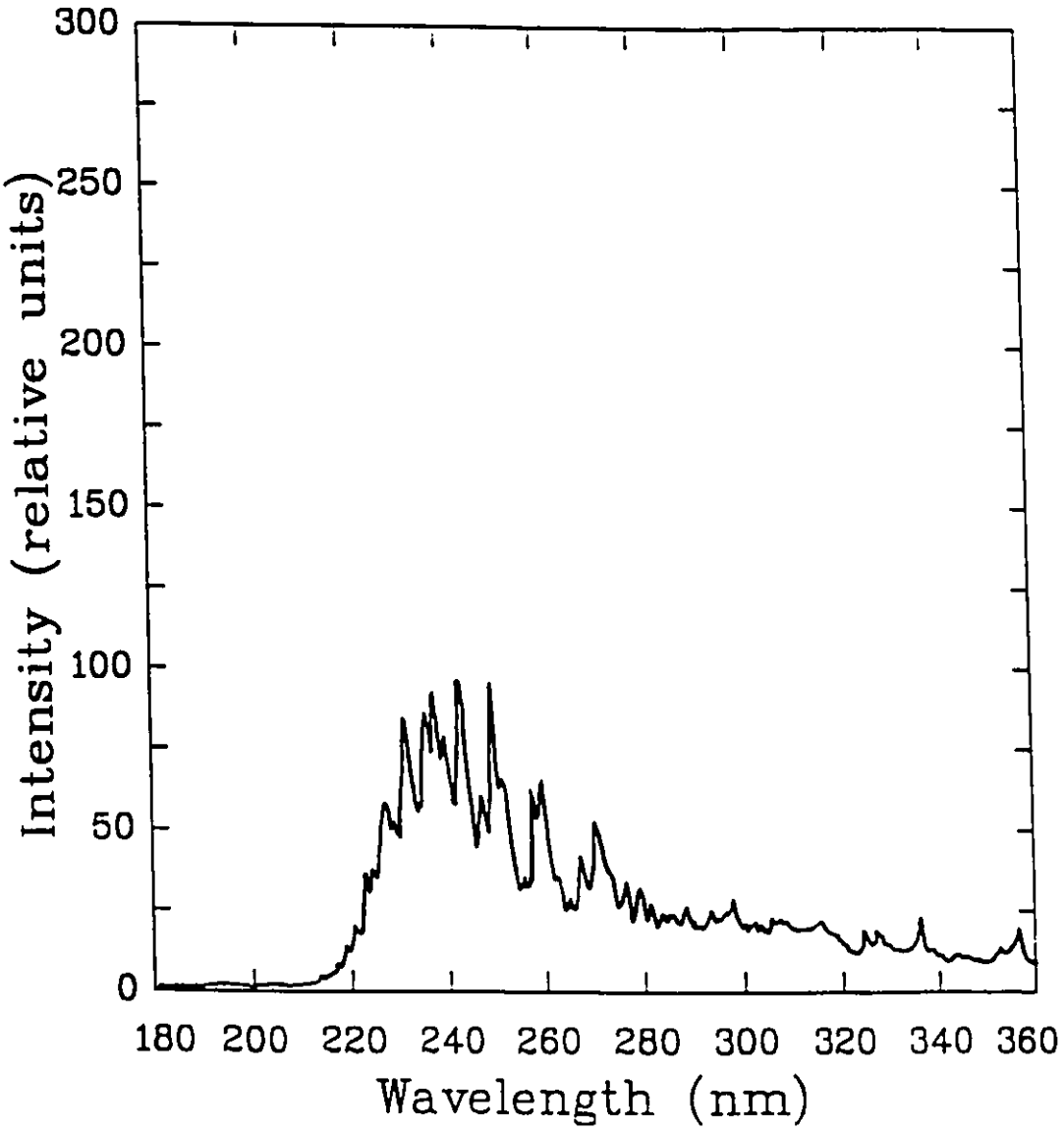

Figure 5.4-4 Fluorescence spectrum for SF_6 at a total pressure of 5 Torr.

5.5 Heteronuclear Halogen Fluorescence

As mentioned previously, it is possible that excimer transitions based on heteronuclear molecular species (such as BrCl) could occur. Using the halogen-bearing gases available, there are six distinct 50:50 binary mixtures that can be examined. These mixtures, and the corresponding spectra, are as follows:

Iodine and Bromine Mixture	(Fig. 5.5-1)
Iodine and Chlorine Mixture	(Fig. 5.5-2)
Iodine and Sulfur Hexafluoride Mixture	(Fig. 5.5-3)
Bromine and Chlorine Mixture	(Fig. 5.5-4)
Bromine and Sulfur Hexafluoride Mixture	(Fig. 5.5-5)
Chlorine and Sulfur Hexafluoride Mixture	(Fig. 5.5-6)

No heteronuclear transitions are apparent from any of these spectra. The most interesting emission is that of the mixture of bromine and chlorine (Fig. 5.5-4). In this case, the 291-nm peak due to Br_2 combines with the 258-nm Cl_2 peak to give a strong, broad emission over the wavelength range 220 nm to 295 nm. If the heteronuclear excimer BrCl is being formed, its emission cannot be resolved under these conditions.

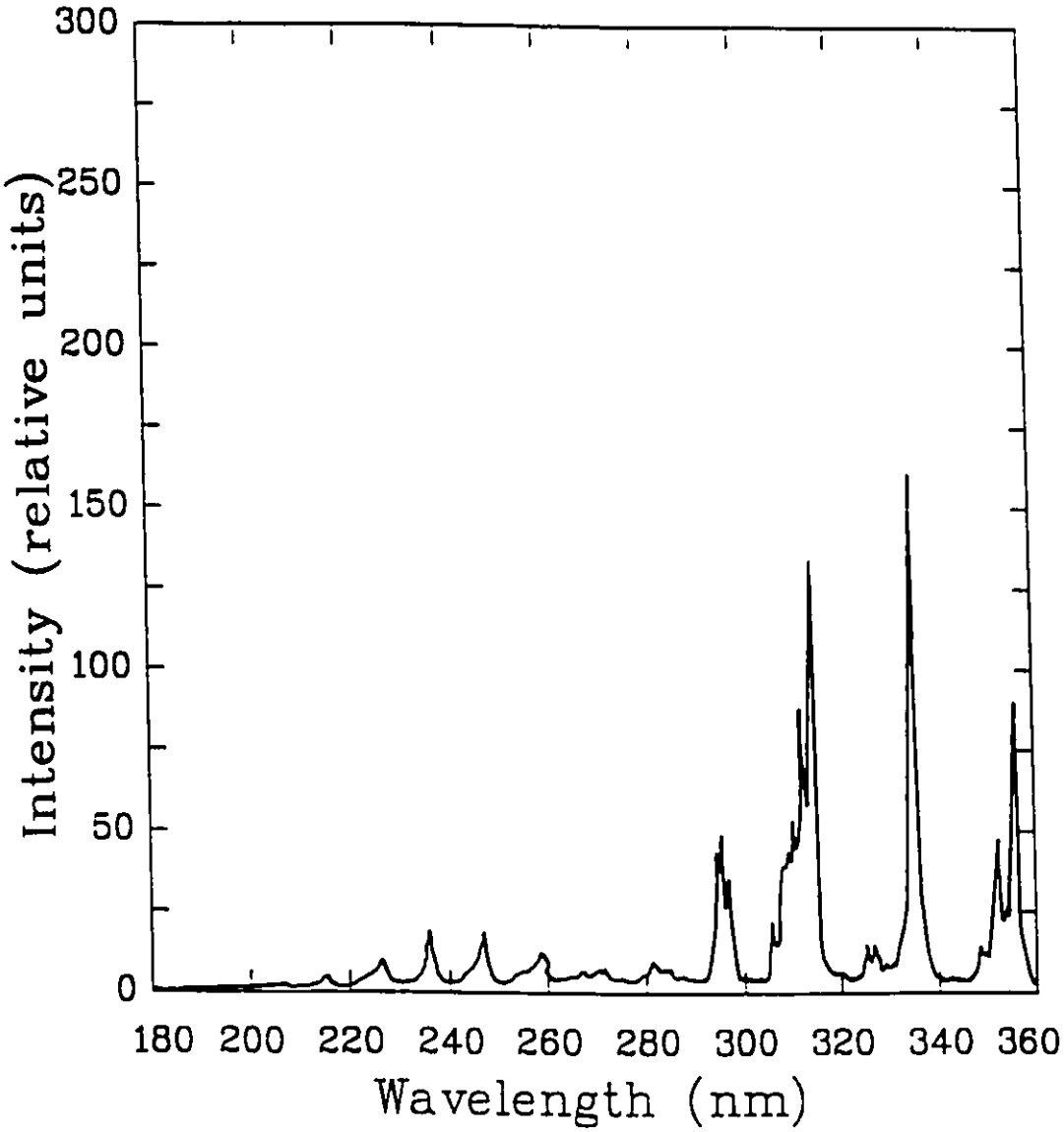

Figure 5.5-1 Fluorescence spectrum for a 50:50 I_2:Br_2 mixture at a total pressure of 5 Torr.

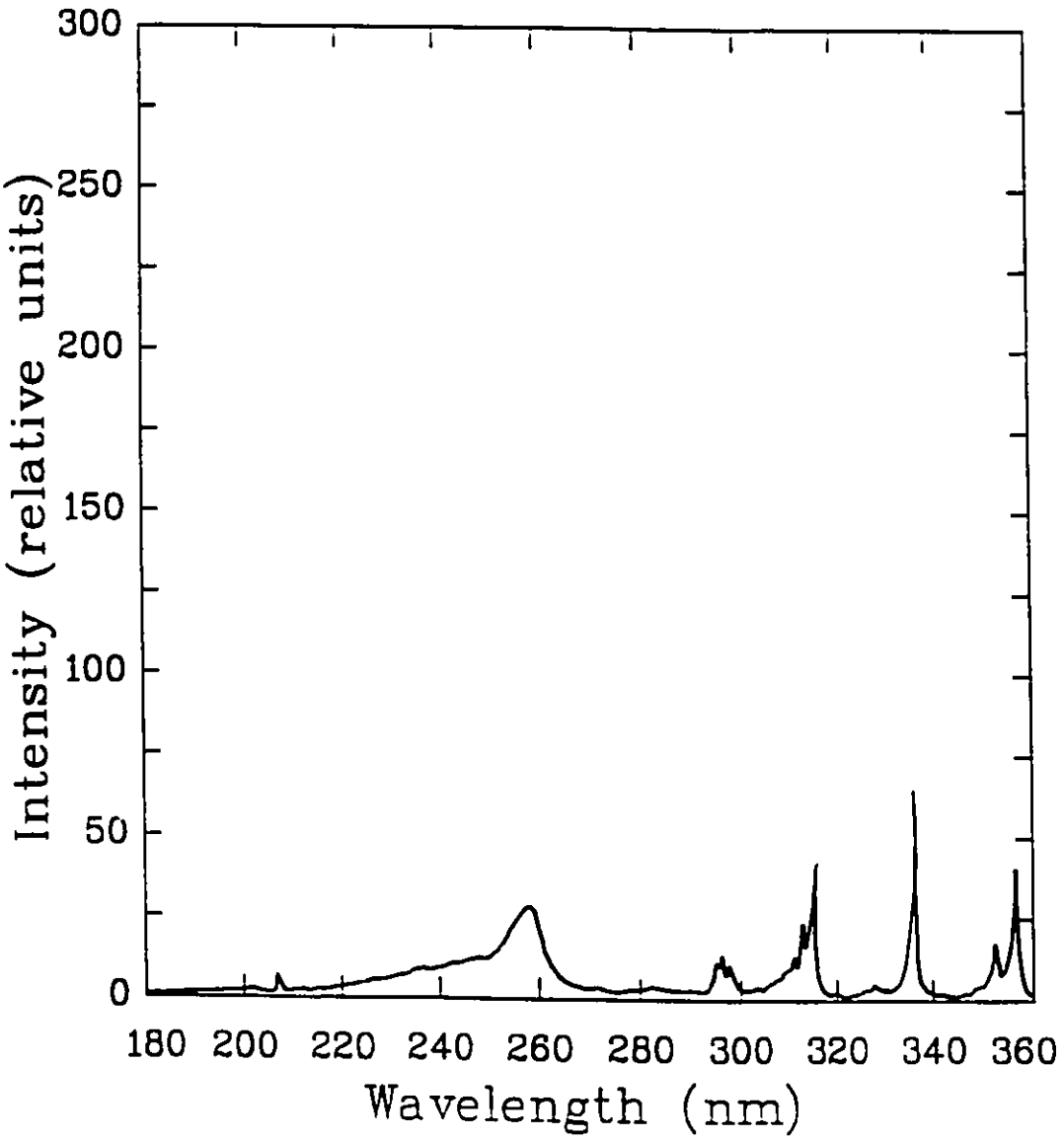

Figure 5.5-2 Fluorescence spectrum for a 50:50 I_2:Cl_2 mixture at a total pressure of 5 Torr.

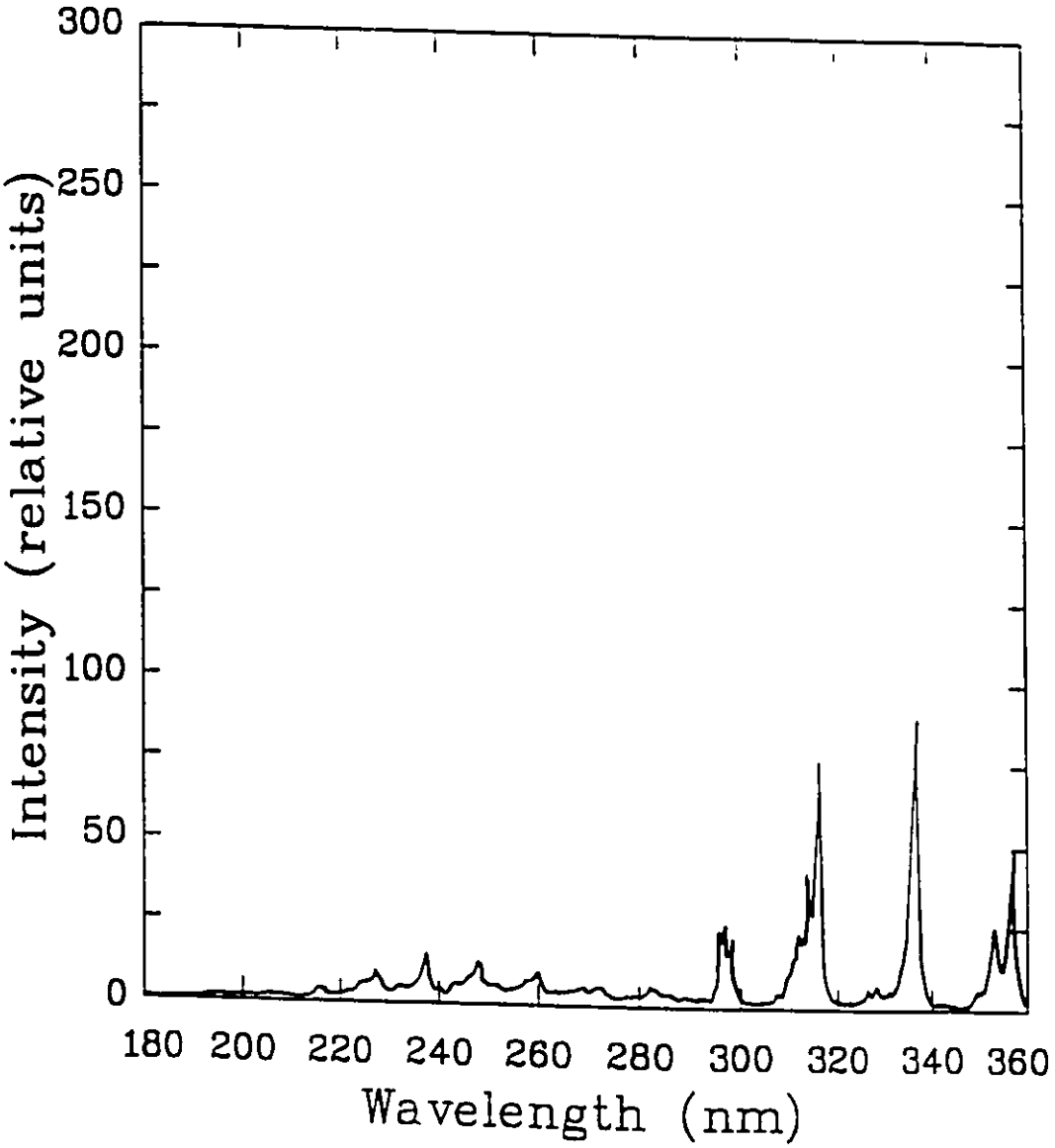

Figure 5.5-3 Fluorescence spectrum for a 50:50 I_2:SF_6 mixture at a total pressure of 5 Torr.

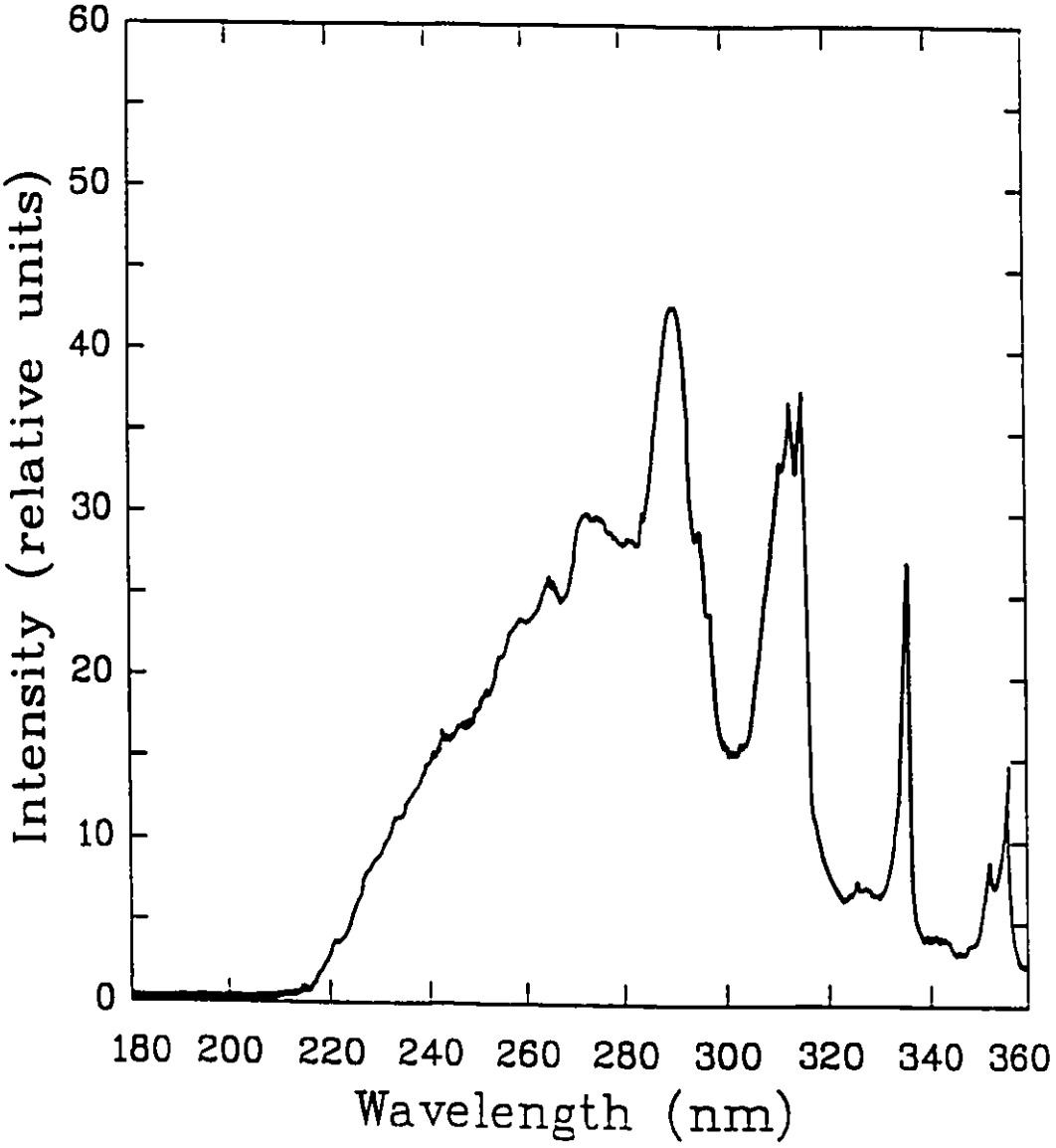

Figure 5.5-4 Fluorescence spectrum for a 50:50 Br_2:Cl_2 mixture at a total pressure of 5 Torr.

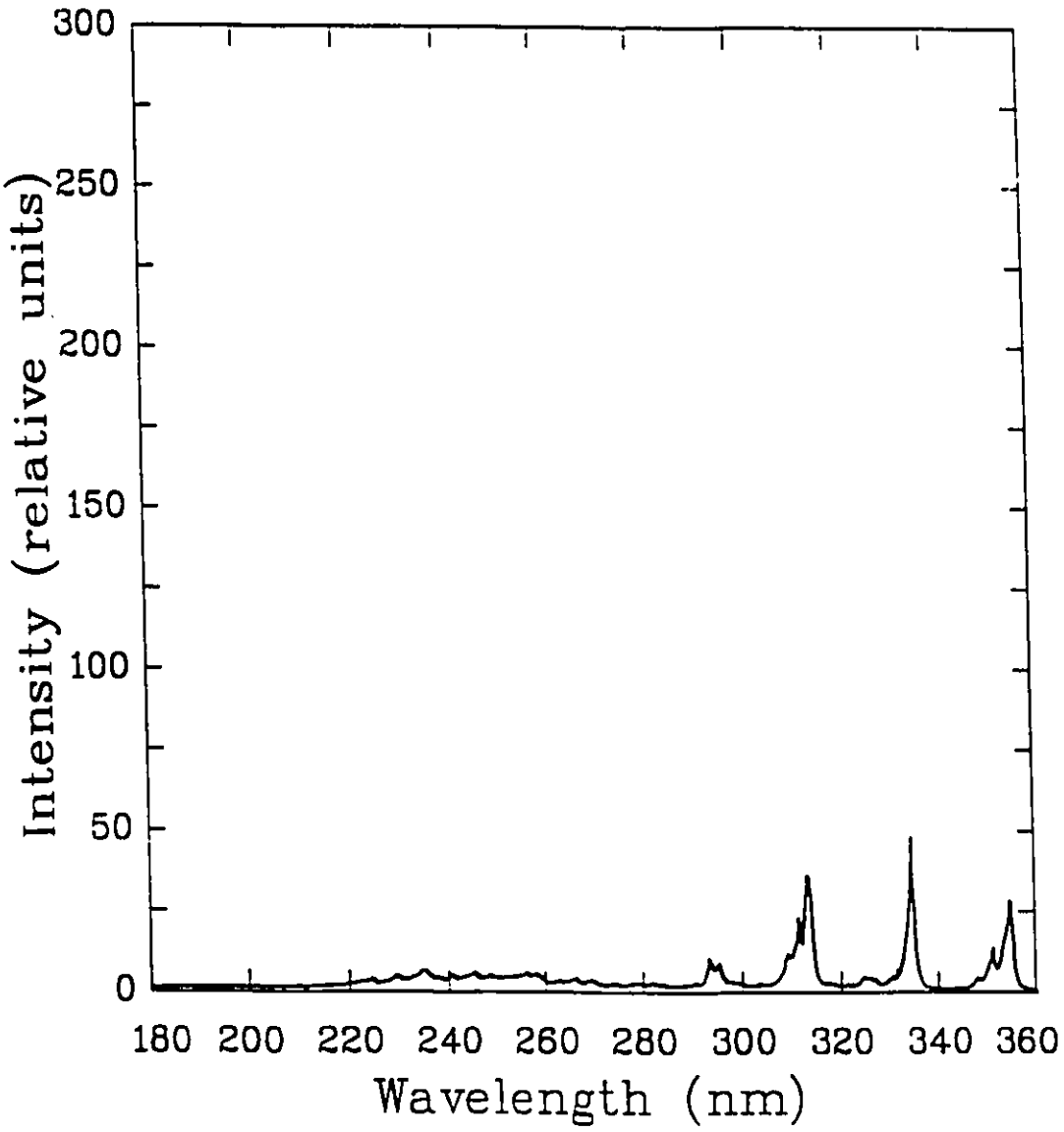

Figure 5.5-5 Fluorescence spectrum for a 50:50 Br_2:SF_6 mixture at a total pressure of 5 Torr.

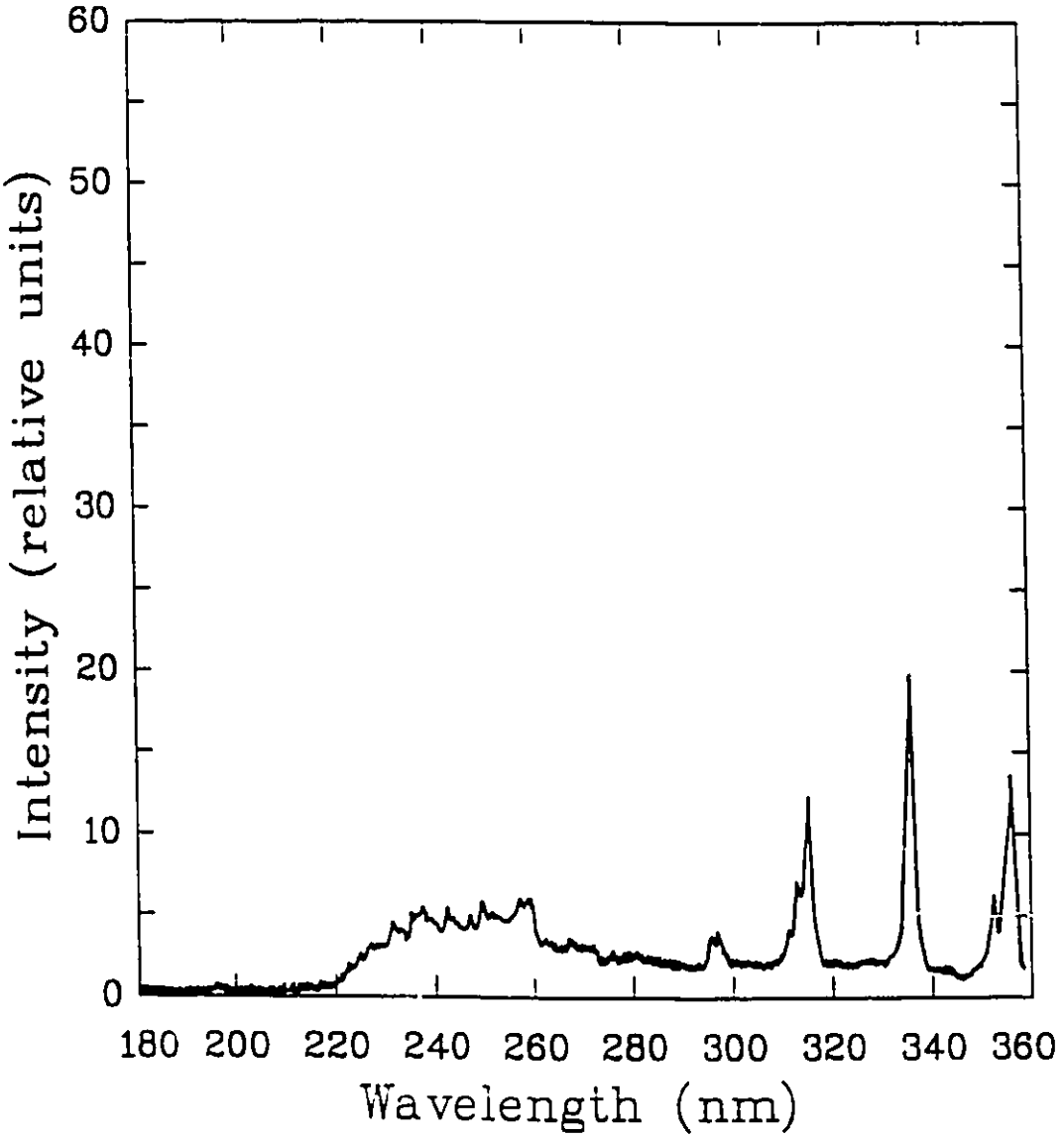

Figure 5.5-6 Fluorescence spectrum for a 50:50 Cl_2:SF_6 mixture at a total pressure of 5 Torr.

5.6 Total-Pressure Optimization

For those gas mixtures that showed strong excimer fluorescence under the above conditions (i.e., at total pressures of 5 Torr with 50:50 gas ratios), further results are reported regarding the optimum total pressure and gas composition. Specifically, three cases are considered: KrCl, XeCl, and Cl_2.

Krypton and Chlorine Binary Mixture:

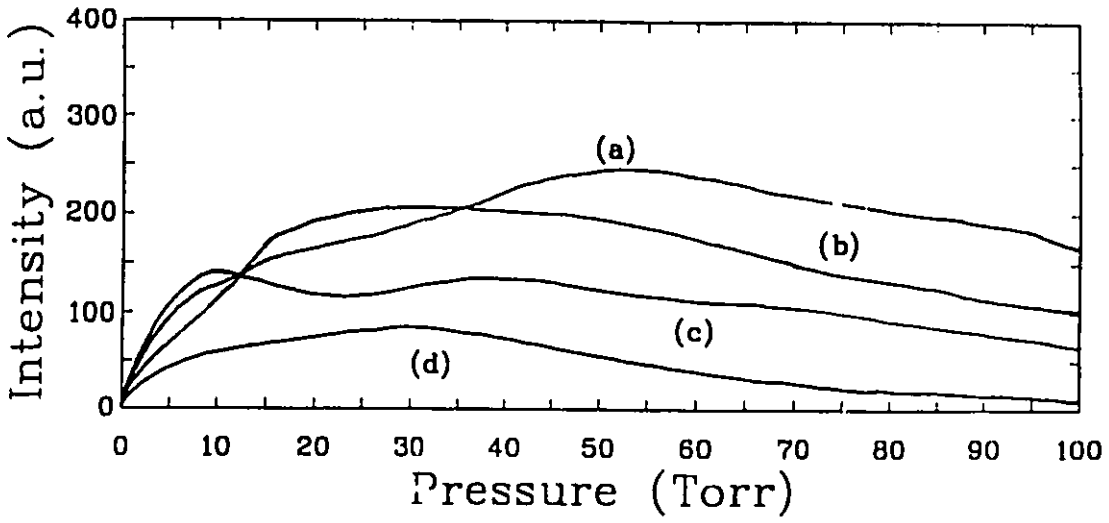

Figure 5.6-1 Effect of total pressure on 222-nm fluorescence intensity in a mixture of krypton and chlorine. The gas ratios Kr:Cl_2 are (a) 80:20, (b) 60:40, (c) 40:60, and (d) 20:80.

Before recording spectra, the KrCl B→X emission at λ = 222 nm is investigated for four different gas compositions, all at total gas pressures between 0 Torr and 100 Torr. These four mixtures, which are denoted by (a), (b), (c) and (d), had Kr:Cl_2 ratios of 80:20, 60:40, 40:60 and 20:80, respectively. Typical data of fluorescence output at λ = 222 nm as

a function of pressure are shown in Fig. 5.6-1. From these data it is evident that the peak 222-nm fluorescence decreases with decreasing krypton concentration, and that the optimum total pressure for maximum fluorescence varies with gas composition.

Spectra for the wavelength range 200 nm to 320 nm, measured for the same four gas mixtures at fixed pressures, are shown in Figs. 5.6-2a to 5.6-2d. The pressures for mixtures (a), (b), (c) and (d), corresponding to maximum 222-nm B→X fluorescence, are near 50 Torr, 30 Torr, 10 Torr and 30 Torr, respectively. Note the presence of the 258-nm excimer Cl_2 transition in each case. For the last case in particular (for which the Kr:Cl_2 ratio is 20:80 and the total pressure is 30 Torr), the 258-nm chlorine transition is extremely intense. The FWHM of the 222-nm transition is approximately 3 nm, and that of the 258-nm transition is approximately 5 nm. Under the tested conditions, the center wavelengths and spectral widths remain constant to within experimental error.

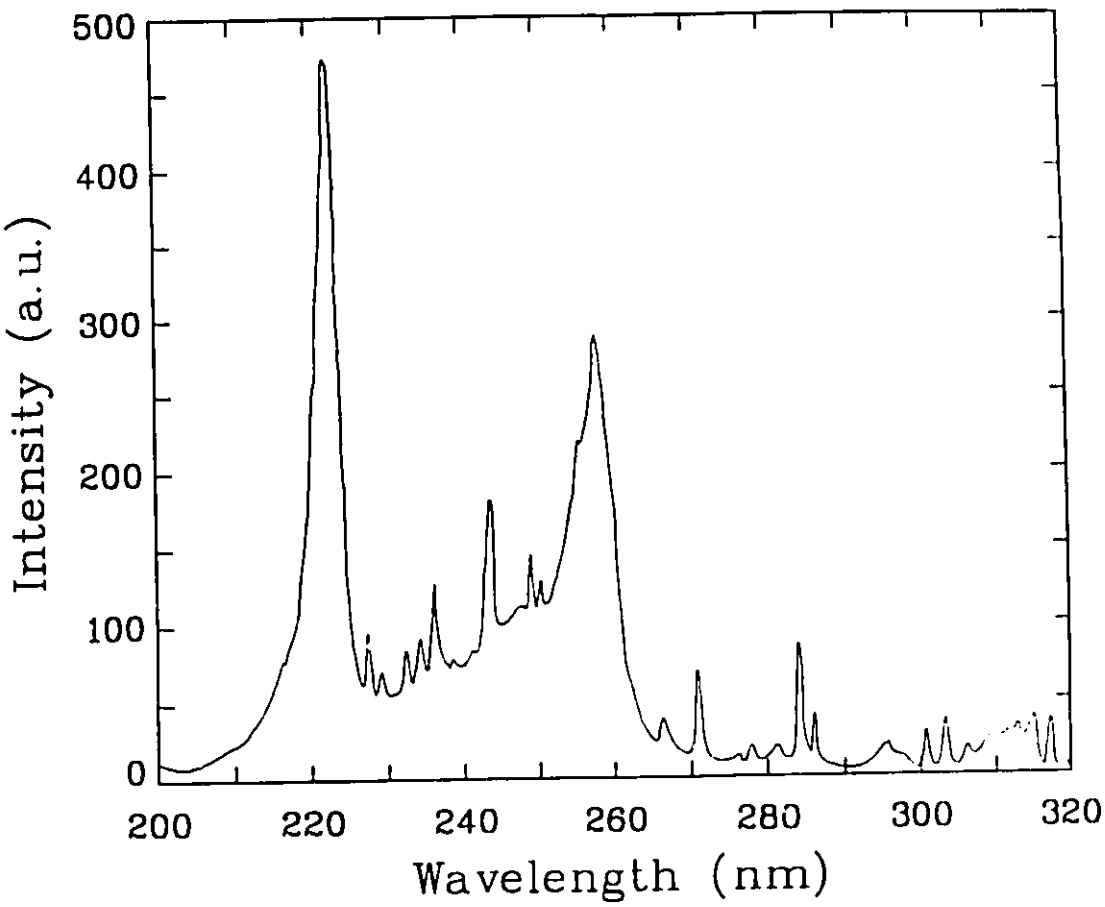

Figure 5.6-2a Fluorescence spectrum for an 80:20 Kr:Cl_2 mixture at a total pressure of 50 Torr.

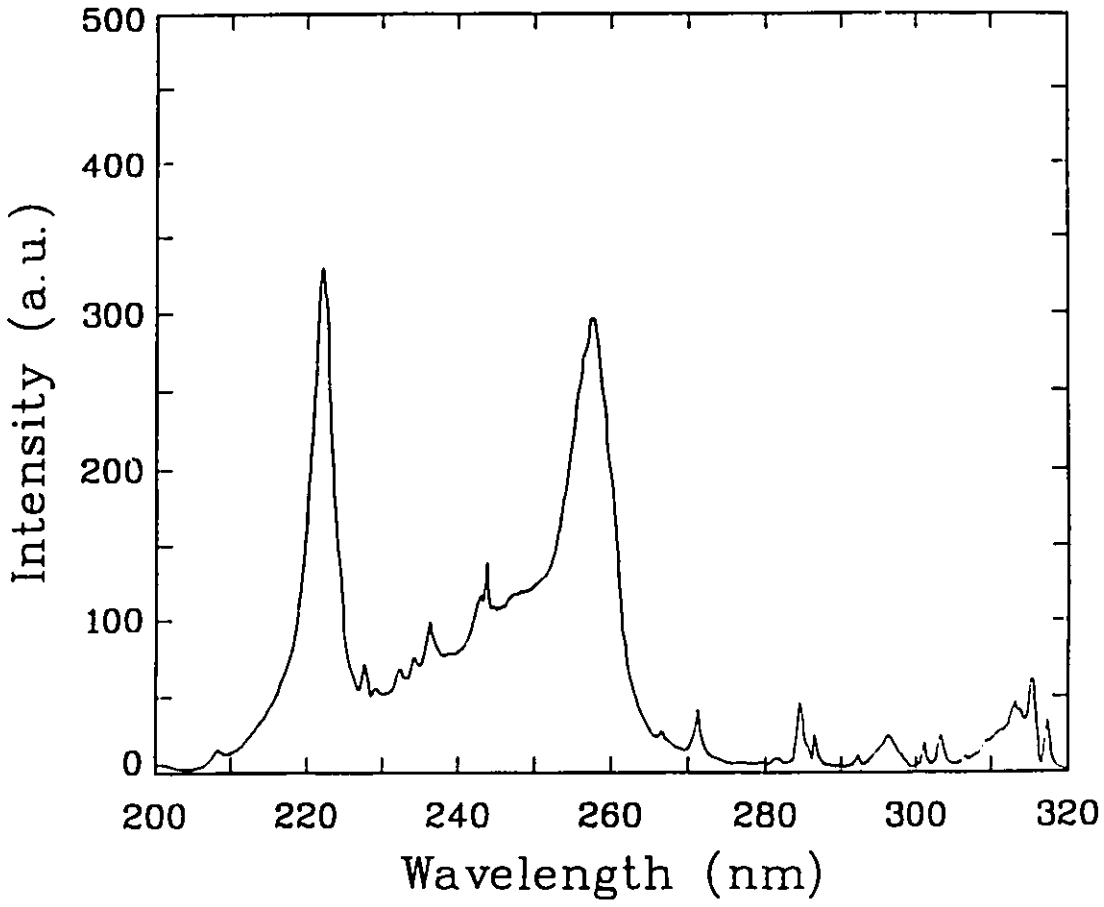

Figure 5.6-2b Fluorescence spectrum for a 60:40 Kr:Cl_2 mixture at a total pressure of 30 Torr.

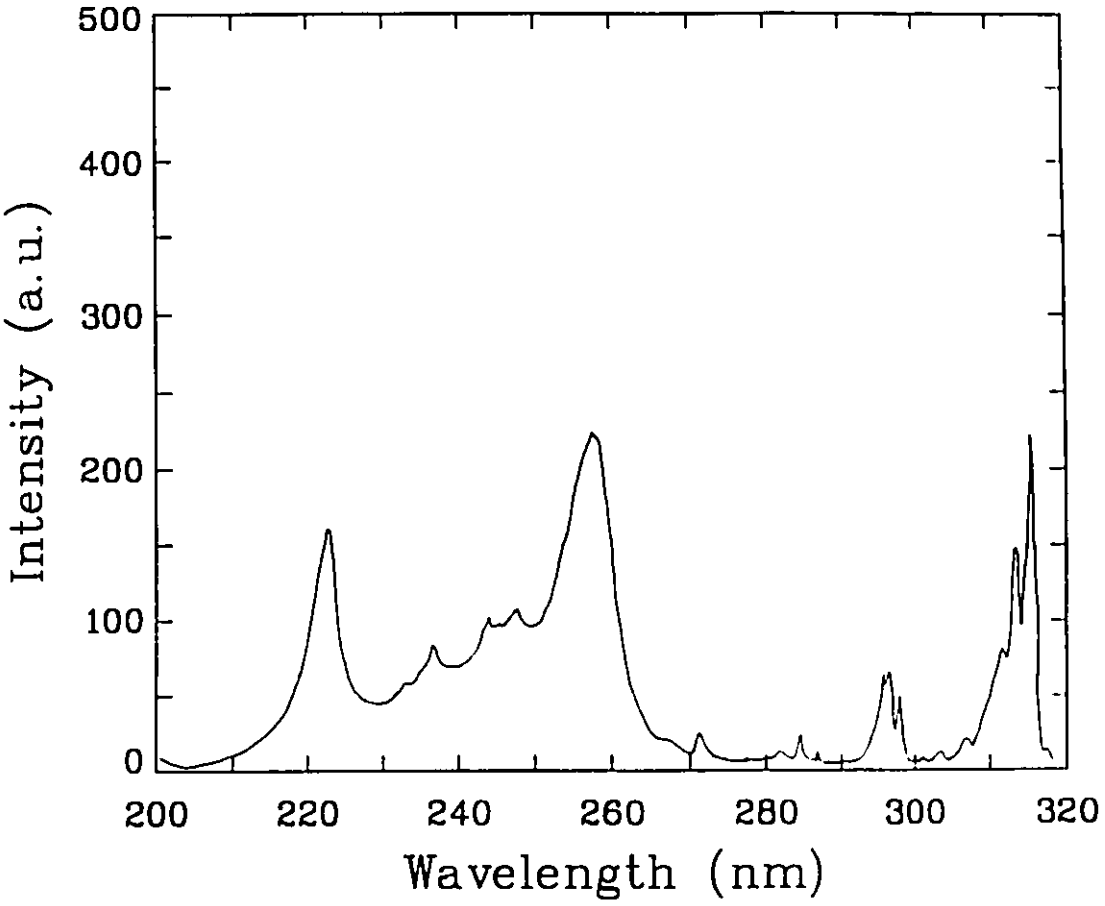

Figure 5.6-2c Fluorescence spectrum for a 40:60 Kr:Cl_2 mixture at a total pressure of 10 Torr.

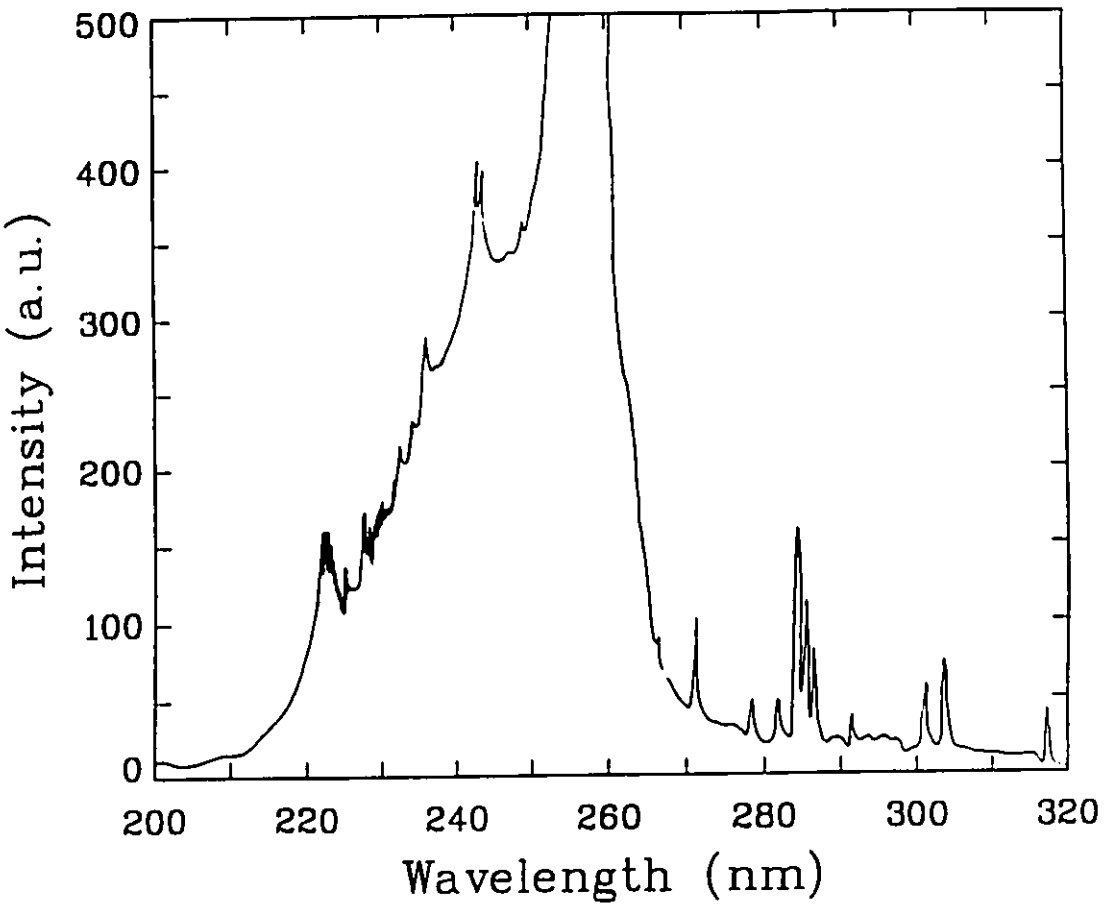

Figure 5.6-2d Fluorescence spectrum for a 20:80 Kr:Cl_2 mixture at a total pressure of 30 Torr.

Xenon and Chlorine Binary Mixture:

The effect of total pressure on the XeCl B→X fluorescence at λ = 308 nm was investigated for gas mixtures having Xe:Cl_2 ratios of 80:20, 60:40, 40:60, and 20:80, termed (a), (b), (c), and (d), respectively. In each case, the pressure was varied from 0 Torr to 100 Torr and is monitored using the pressure transducer to drive the x-input of the X-Y recorder. The monochromator was fixed at 308 nm. Typical data are shown in Fig. 5.6-3. Mixture (c) has the strongest peak fluorescence, this occurring at a pressure near 40 Torr. The optimum pressure for mixture (b) is also near 40 Torr. The chlorine-rich mixture (d) shows the weakest peak fluorescence, with an optimum pressure near 14 Torr. In all mixtures but (a), a change from a uniform discharge to one consisting of filamentary arcs took place at a pressure between 25 Torr and 50 Torr. The exact pressure for arc formation is not reproducible, although the effects are obvious. For example, at pressures greater than 50 Torr, the effect of the arcing is clearly visible as noise on traces (b) and (c) in Fig. 5.6-3. Mixture (a) exhibits unique behavior in a number of ways. The optimum pressure for this mixture, near 75 Torr, is much higher than for any other mixture, and the fluorescence is least sensitive to variations in total pressure. Finally, this xenon-rich mixture rarely produced arc discharges below a pressure of 90 Torr. As before, a precise pressure for arc formation could not be determined.

The spectra for the above four gas mixtures were measured over the wavelength range 200 nm to 320 nm, as shown in Figs. 5.6-4a to 5.6-4d. The pressures for mixtures (a), (b), (c) and (d), corresponding to maximum B→X fluorescence, are 75, 40, 40 and 14 Torr, respectively. Note that the 258-nm Cl_2 transition is present in each case. To within experimental error, no wavelength shifts are evident for any of the transitions.

Figure 5.6-4a shows that the 308-nm transition (B→X) is clearly dominant under the operating conditions used (Xe:Cl_2 ratio 80:20, 75-torr pressure). The FWHM of this

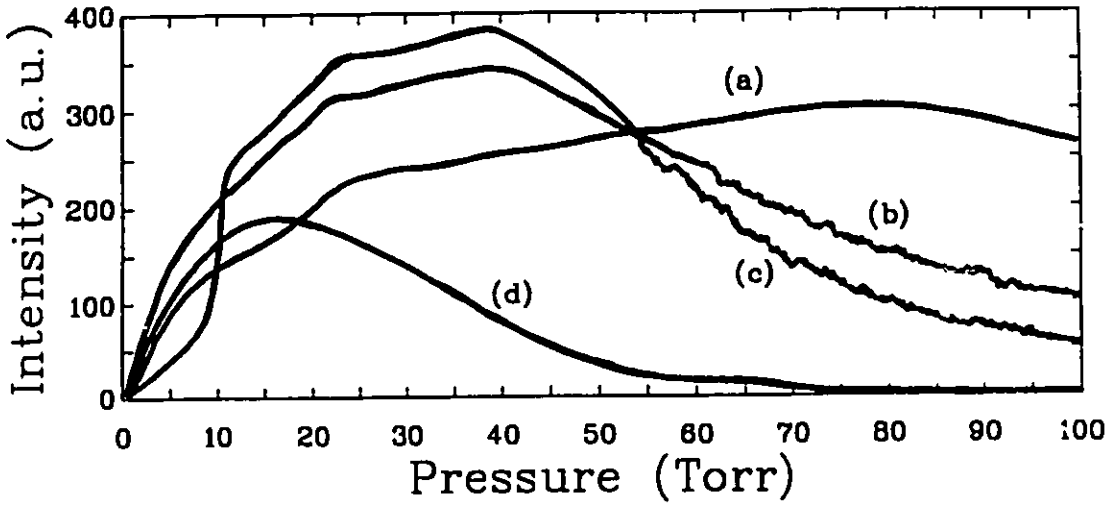

Figure 5.6-3 Effect of total pressure on 308-nm fluorescence intensity in a mixture of xenon and chlorine. The gas ratios $Xe:Cl_2$ are (a) 80:20, (b) 60:40, (c) 40:60, and (d) 20:80.

transition is approximately 8 nm. The 236-nm transition (D→X), with a FWHM of approximately 6 nm, is also visible, but is an order of magnitude less intense, as is the molecular chlorine transition at 258 nm.

Figure 5.6-4b has a profile that is very similar to Fig. 5.6-2a. Note that the intensity of the 258-nm molecular chlorine transition is increased relative to the 236-nm XeCl transition (D→X).

Figure 5.6-4c is dominated by the 258-nm molecular chlorine transition (8-nm FWHM), but the 308-nm XeCl transition (B→X) is also quite strong. The peak intensity of the 236-nm XeCl transition (D→X) is much less than that of the 308-nm transition. Under the present conditions, there is an increased broad fluorescence between 260 nm and 300 nm.

Figure 5.6-4d shows the spectrum for the chlorine-rich mixture at a pressure of only 14 Torr. The weak intensity of the Cl_2 transition can be explained by the relatively low total pressure.

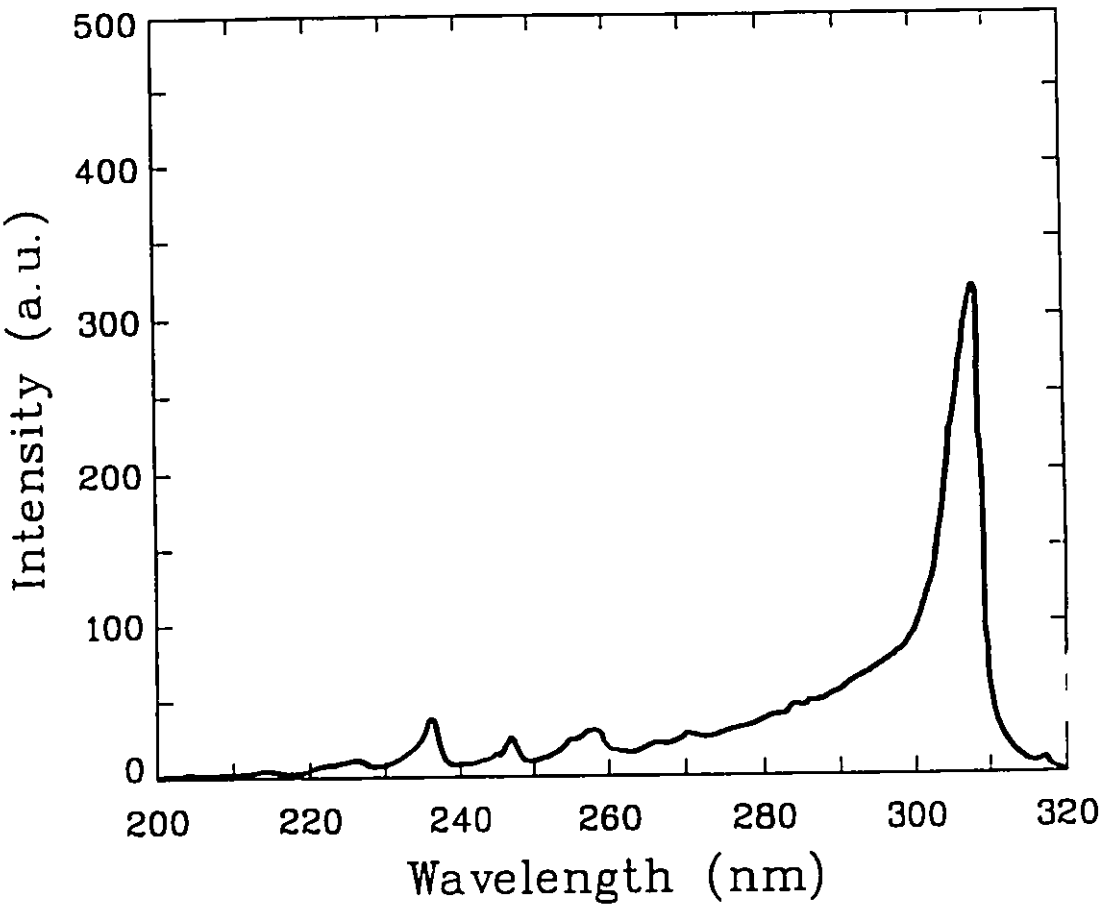

Figure 5.6-4a Fluorescence spectrum for an 80:20 Xe:Cl_2 mixture at a total pressure of 75 Torr.

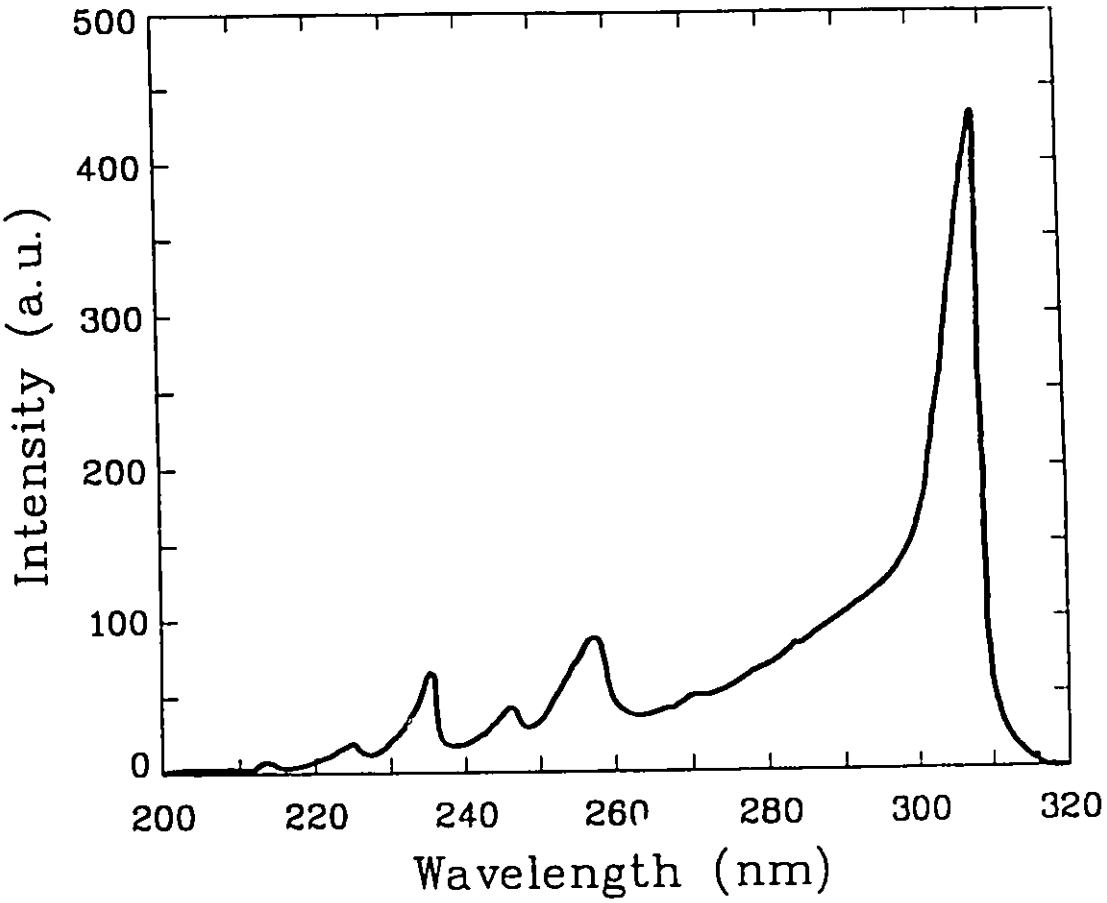

Figure 5.6-4b Fluorescence spectrum for a 60:40 $Xe:Cl_2$ mixture at a total pressure of 40 Torr.

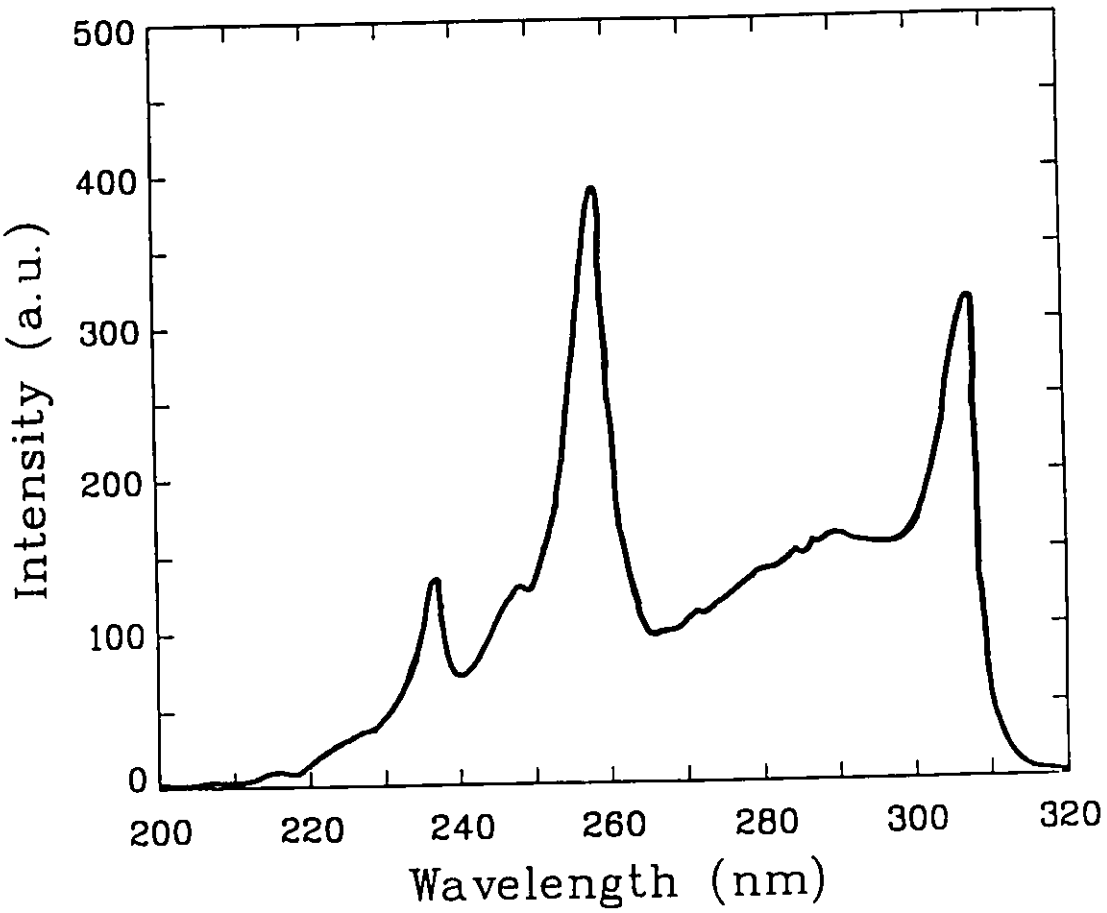

Figure 5.6-4c Fluorescence spectrum for a 40:60 Xe:Cl_2 mixture at a total pressure of 40 Torr.

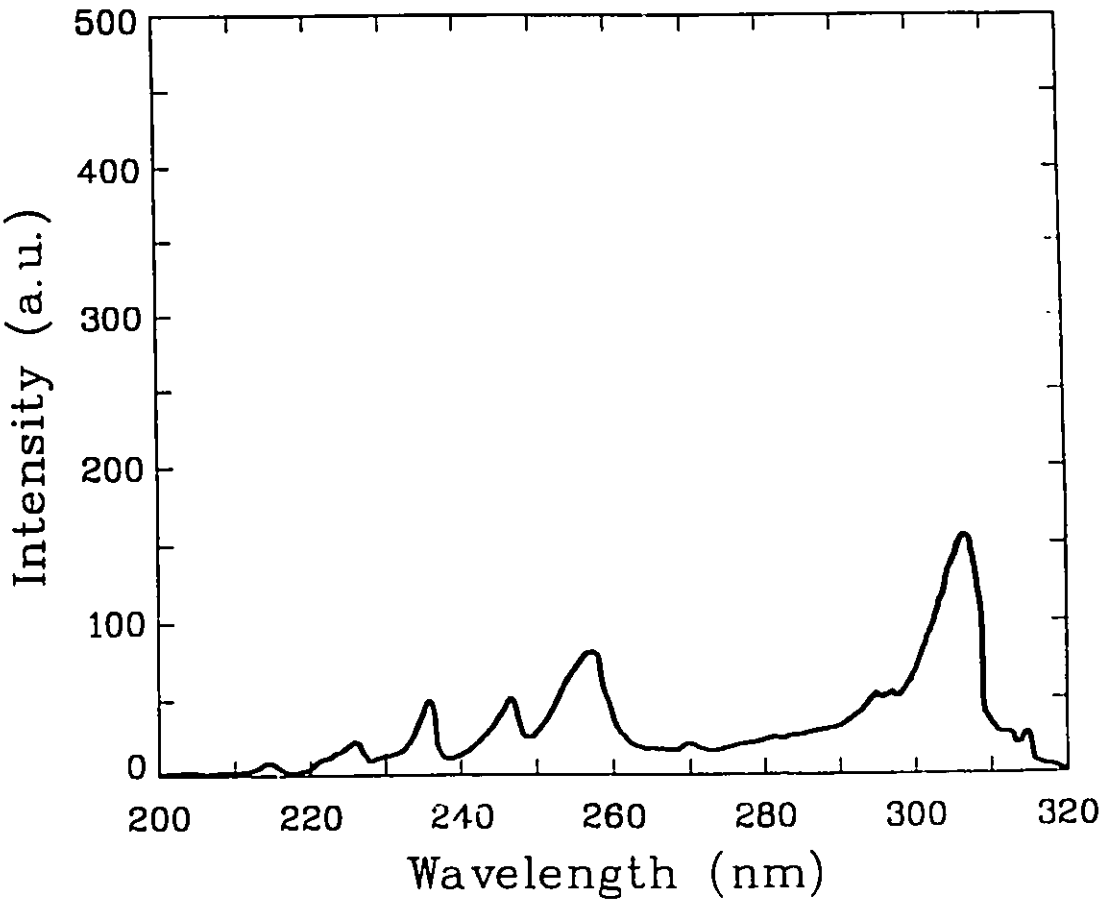

Figure 5.6-4d Fluorescence spectrum for a 20:80 Xe:Cl_2 mixture at a total pressure of 14 Torr.

Pure Chlorine:

The effect of total pressure on the molecular Cl_2 fluorescence at $\lambda = 258$ nm was investigated for pure chlorine. Again, the pressure is varied from 0 Torr to 100 Torr and was monitored using the pressure transducer to drive the x-input of the X-Y recorder. The monochromator was fixed at 258 nm. Typical data are shown in Fig. 5.6-5. From this curve, it is clear that the optimum pressure for 258-nm excimer fluorescence is near 35 Torr. The spectrum over the range 200 nm to 320 nm is given for this optimum pressure in Fig. 5.6-6. This spectrum consists mainly of a single strong peak at 258 nm with a FWHM of ~8 nm. There is some broad fluorescence between 220 nm and the principal peak. The longer-wavelength components that are apparent at a pressure of 5 Torr (see Fig. 5.4-3) are suppressed at this higher pressure.

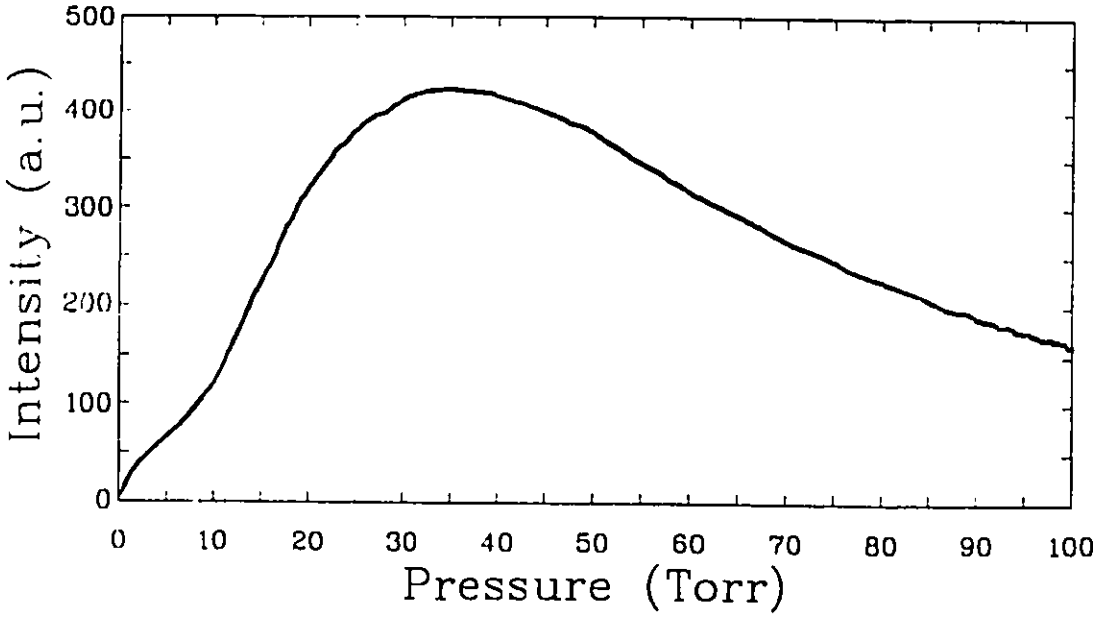

Figure 5.6-5 Effect of total pressure on 258-nm fluorescence intensity in chlorine.

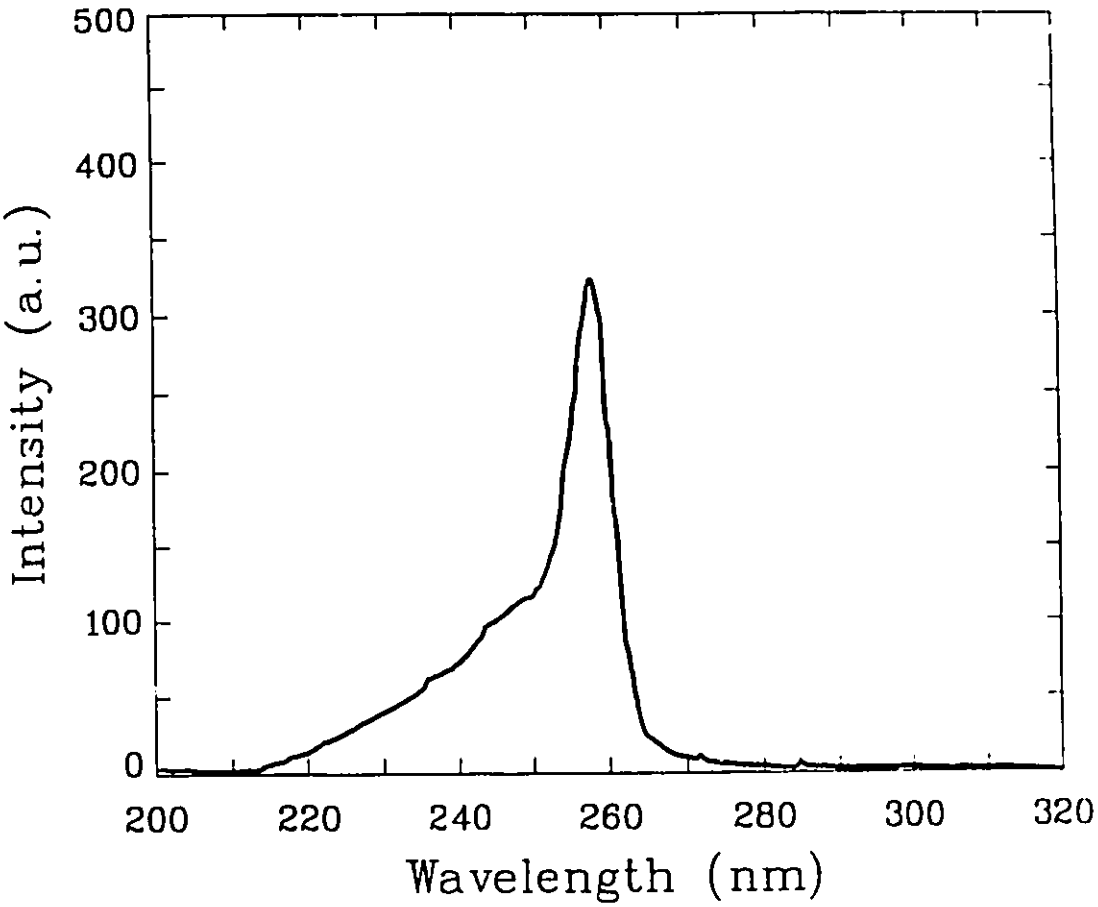

Figure 5.6-6 Fluorescence spectrum for Cl_2 at a total pressure of 35 Torr.

Chapter 6

Investigation of Gain in a Microwave Discharge

This chapter describes the investigation of gain in microwave-excited gas discharges. These investigations require a different microwave resonator from the lamp studies. This resonator is characterized analogously to that described in Chapter 3. Production of a uniform plasma column in a $CO_2/N_2/He$ laser mixture and in argon is described. Furthermore, upper limits are deduced for the small-signal gain under various conditions for each of these systems. In this chapter, a familiarity of basic laser theory (i.e., Fabry-Perot resonators, laser threshold, etc.) and the specific laser systems is assumed of the reader. For a good introduction to these topics, refer to the text by Verdeyen (1981) or that by Yariv (1985). A more advanced treatment of the physics and technology of carbon dioxide lasers is given by Witteman (1987).

6.1 Microwave Resonator Design

The microwave resonator employed for the gain investigations (termed the "gain

resonator") is different from that used for the incoherent-lamp studies (termed the "lamp resonator"). In order to obtain laser operation, it is necessary to have a high overall gain per pass. To this end, the gain resonator was designed and constructed to allow the excitation of a long (i.e., > 0.5 m) discharge. The side view of this resonator is shown in Fig. 6.1-1. The holes in the side wall allow a clear view of the discharge without allowing significant microwave leakage. Spring-steel clamps, which are not shown in the figure, are used to secure the top and bottom surfaces of the resonator to flanges on the side walls, such that the waveguide width is continuously adjustable. Use is made of brass end-wall sliders, which are described in Section 3.1. The discharge tube, which is shown at the top of Fig. 6.1-1, extends through these sliders down the center of the waveguide. The top and bottom surfaces of the resonator are lined with copper, and the side walls are made from aluminum.

Operation near cutoff increases the waveguide wavelength so that a very long resonator can still operate in the TE_{101} mode. Thus there are no nodes (i.e., dark regions) present in the discharge. If the waveguide width is adjusted so that the resonator is at cutoff (or slightly below), it is possible to create conditions under which the discharge will extend almost indefinitely along the waveguide. Qualitatively, this can be explained by considering that the presence of a discharge (because of its relative permittivity) effectively increases the electrical width of a waveguide. If a signal is injected below cutoff into the middle of a long waveguide, it will be exponentially attenuated. If a discharge is created, it will form where the power is greatest, at the injection point. The presence of the discharge will allow the signal to propagate (now above cutoff) away from the injection point, thus allowing the discharge to extend further from the injection point. This process continues until there is so much attenuation from the plasma that the electric field from the signal is insufficient to ionize the gas that is adjacent to the ends of the discharge. The resulting steady-state length of the discharge is a function of the waveguide attenuation (which, ideally, does not consume

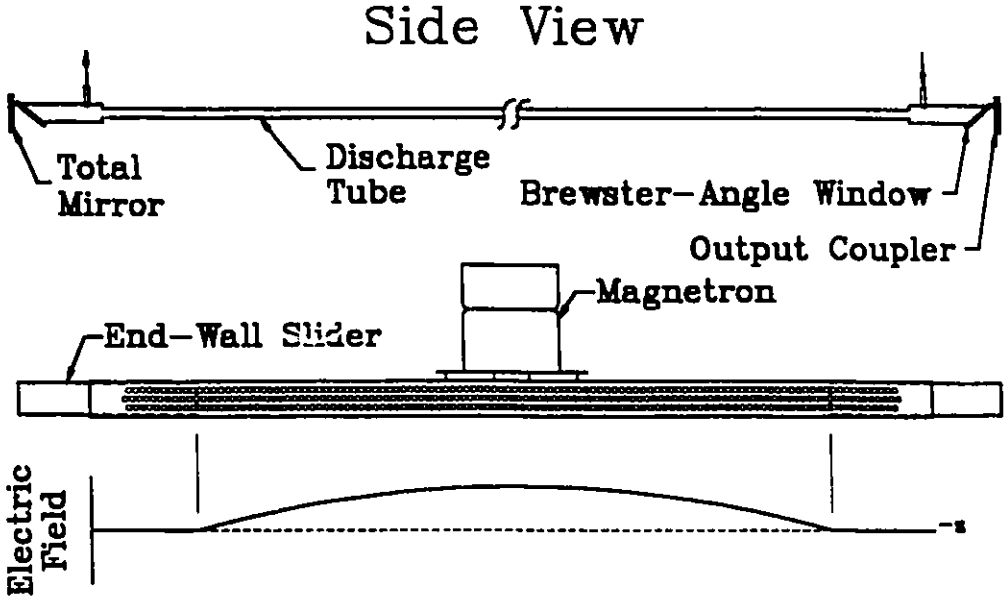

Figure 6.1-1 Side view of the magnetron/resonator assembly constructed for the gain investigations. For clarity, the clamps described in the text are not shown. The resonator operates near cutoff in the TE_{101} mode. Tuning is accomplished by adjusting the position of the end-wall sliders. Also shown is the electric-field distribution before discharge ignition (below) and the discharge tube and optical resonator (removed from waveguide, above).

power), the plasma attenuation (which always consumes power), other plasma properties (i.e., breakdown field, maintenance field, etc.) and the injected power level. It is even possible to produce a long-column discharge without an external waveguide: under certain conditions surface waves can form, containing and directing a discharge down a dielectric tube (Moisan *et al*, 1975). The mechanism by which this occurs is quite complicated, and is not discussed further.

For all of the investigations reported here, the gain resonator is set to operate slightly above cutoff in order to allow a quantitative analysis to be made. Although operation is in the TE_{101} mode (rather than the TE_{102} mode), the relationships that are developed in Section 3.2 are still valid. In particular, the expression for the quality factor of the resonator is

$$Q = \omega_r \frac{W}{P_{loss}} = \frac{\omega_r \varepsilon_r Z_0^2}{4} \left(\frac{abc}{R_{s1}ab + R_{s2}bc + R_{s3}ac} \right). \qquad (3.2-6)$$

By definition, the surface resistance is

$$R_s = \frac{1}{\sigma l \delta} = \sqrt{\frac{\omega\mu}{2\sigma}}. \qquad (3.2-1)$$

The conductivities of brass, aluminum and copper are $1.57 \times 10^7 S/m$, $3.72 \times 10^7 S/m$ and $5.80 \times 10^7 S/m$, respectively. Thus $R_{s1} = .025\Omega$, $R_{s2} = .016\Omega$ and $R_{s1} = .013\Omega$. The dimensions of the resonator are a = 62 mm, b = 25 mm and c = 508 mm. The waveguide impedance is given by

$$Z_0 = \frac{\eta}{\sqrt{1 - (\omega_{co}/\omega)^2}}. \qquad (2.3-6)$$

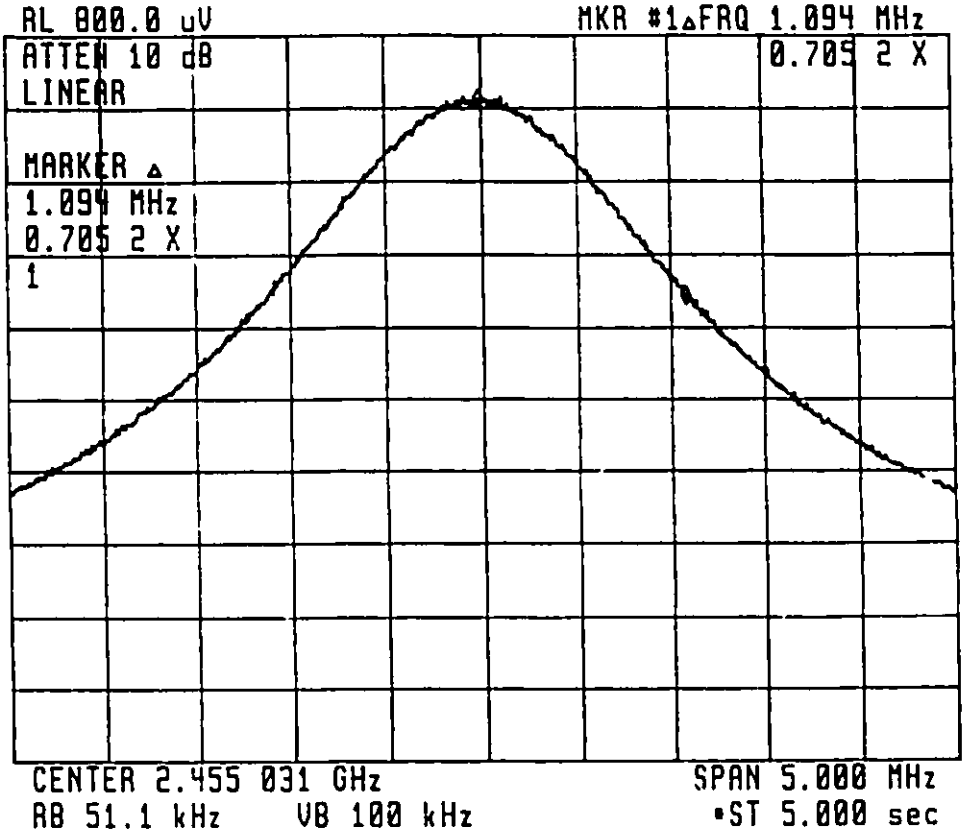

Figure 6.1-2 Two-port frequency response of the empty gain magnetron/resonator assembly as measured on a scalar network analyzer. The frequency range is 5 MHz, and the transmission bandwidth is 2.188 MHz, corresponding to a Q of 1122.

In this case, $Z_o = 2350\Omega$. Substitution of these values into Eq. 3.2-6 gives a Q of approximately 230,000. This huge theoretical value is not a mistake or artifact. The lamp resonator described in Chapter 3 has a theoretical Q of 6100. The greater Q of the gain resonator is due mainly to the drastic increase in waveguide impedance that occurs as cutoff is approached; at cutoff, the TE wave impedance becomes infinite. Measured values of Q are

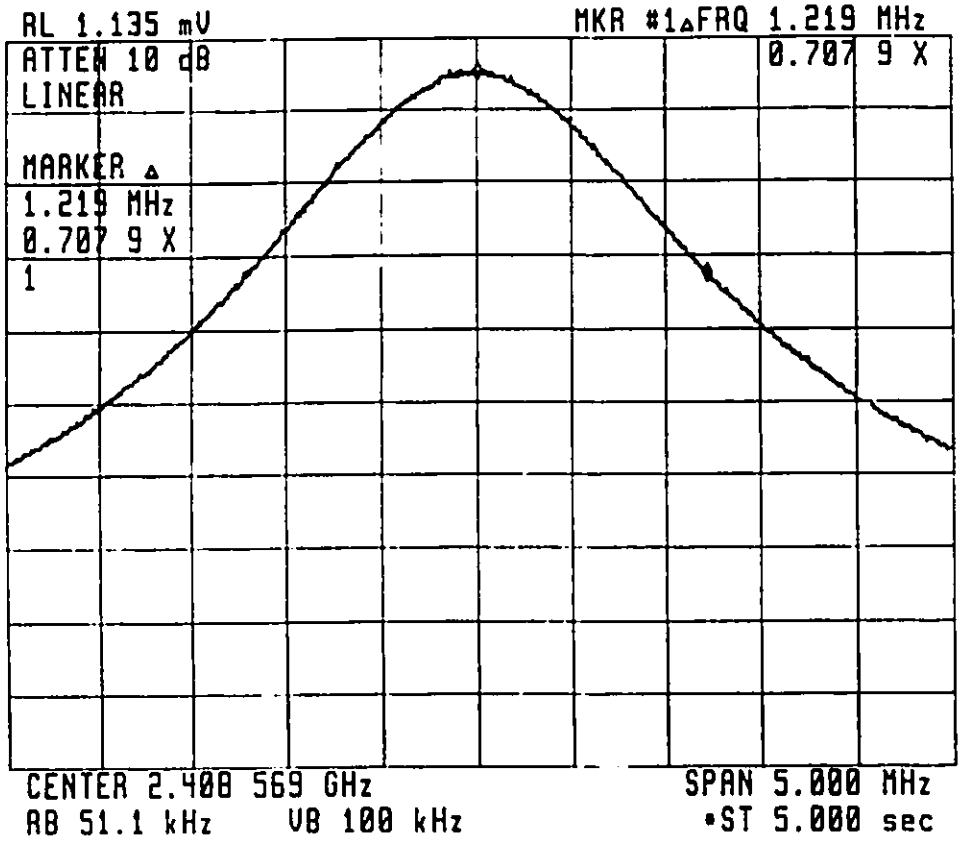

Figure 6.1-3 Two-port frequency response of the magnetron/resonator assembly with a 10-mm fused-silica tube inserted horizontally through the filter tubes. The frequency range is still 5 MHz, and the transmission bandwidth is now 2.439 MHz, corresponding to a Q of 988. Note the 1.9% decrease in the center frequency.

orders of magnitude lower because of losses that have not been considered in this analysis. As before, the most significant of these is the imperfect electrical connection between the end-wall sliders and the waveguide, and the effect of magnetron losses on the assembly. Still, the measured values of Q are significantly higher that those for the lamp resonator. Figure 6.1-2 shows the two-port frequency response of the gain resonator/magnetron

assembly. This response is measured on a scalar network analyzer (Hewlett-Packard 70100A) over a 5-MHz bandwidth centered near 2.45 GHz. The full procedural details are given in Section 3.2. From this figure, the bandwidth is 2.188 MHz and the resonant frequency is 2.455 GHz, yielding Q = 1122.

These frequency-response measurements are repeated with an empty 10-mm SiO_2 discharge tube placed longitudinally in the gain resonator, yielding the data that is given in Fig. 6.1-3. With the tube in place, the bandwidth increases to 2.439 MHz, and the resonant frequency drops slightly to 2.409 GHz. Therefore, Q = 988 under these conditions.

These quality factors seem to indicate that 12% of the microwave power that is incident on the discharge is absorbed by the discharge tube; however, this conclusion is not entirely correct. The presence of the discharge tube in the resonator increases the effective width of the waveguide, moving its operation further from cutoff. One directly observable result of this is the 46-MHz shift in resonant frequency, which results from the insertion of the discharge tube. This represents a 1.9% drop in the resonant frequency. Because the gain resonator is designed to operate so close to cutoff, its electrical parameters are extremely sensitive to changes in its effective dimensions or resonant frequency. The reduced resonant frequency markedly lowers the value for the waveguide impedance and thus lowers the quality factor. An inspection of Eqs. 2.3-6 and 3.2-6 shows just how sensitive the quality factor is when operation is near cutoff. Due to this sensitivity and the uncertainties in the effective dimensions of the waveguide, a full quantitative analysis is not given. Instead, it is reasonable to estimate the absorption to be the same as for the lamp resonator, (i.e., 7%). This estimate is reasonable, as is demonstrated below.

In Section 2.4, it is shown that a square resonator exhibits the least sensitivity (in its resonant frequency) to dimensional tolerances. For a TE_{10n} "square" resonator, the relationship between the width a and length c is simply

$$a = nc, \qquad (6.1-1)$$

where n is a non-zero positive integer. The lamp resonator is quite close to satisfying this condition because a = 97 mm and c = 161 mm. Therefore, the effects that are caused by operation near cutoff do not apply to the lamp resonator; any change in the measured Q that is caused by inserting the discharge tube is entirely due to absorption by that tube. Furthermore, due to the similarities in the discharge tubes that are used in the two microwave resonators, it is reasonable to estimate that the amount of absorption by the tube is the same in each case. Therefore the discharge tubes in both microwave resonators absorb 7% of the microwave power that is incident upon the discharge; the resonator walls and magnetron absorb the balance.

As before, an estimate of the quality factor of the gain resonator with the discharge present can be made. The displacement of the end-wall sliders that causes the brightness of the discharge to decrease by a factor of two is directly related to the quality factor of the cavity. In the case of the gain resonator, the end-wall sliders are not long enough to measure this displacement, regardless of gas composition and total pressure. This sets a lower limit on the displacement of ~13 cm, which indicates that $Q \leq 70$ for the gain resonator with the discharge present. Using Eq. 3.2-8 with these values gives a coupling efficiency of ~93%. Estimating the magnetron efficiency to be 70% gives a DC coupling efficiency of 65%.

6.2 Optical Resonator Design

The gain investigations involve constructing an optical Fabry-Perot resonator and then attempting to achieve laser oscillation using a microwave discharge as the active

medium within the resonator. Two laser systems are examined: the $CO_2/N_2/He$ system, and the Ar^+ system. The optical resonator (refer to Fig. 6.1-1) consists of a "total" mirror (i.e., high reflectivity) and an output coupler (i.e., few percent transmission) that are arranged at each end of the discharge tube. Brewster-angle windows are used to seal the discharge tube while providing low-loss optical coupling between the discharge and resonator.

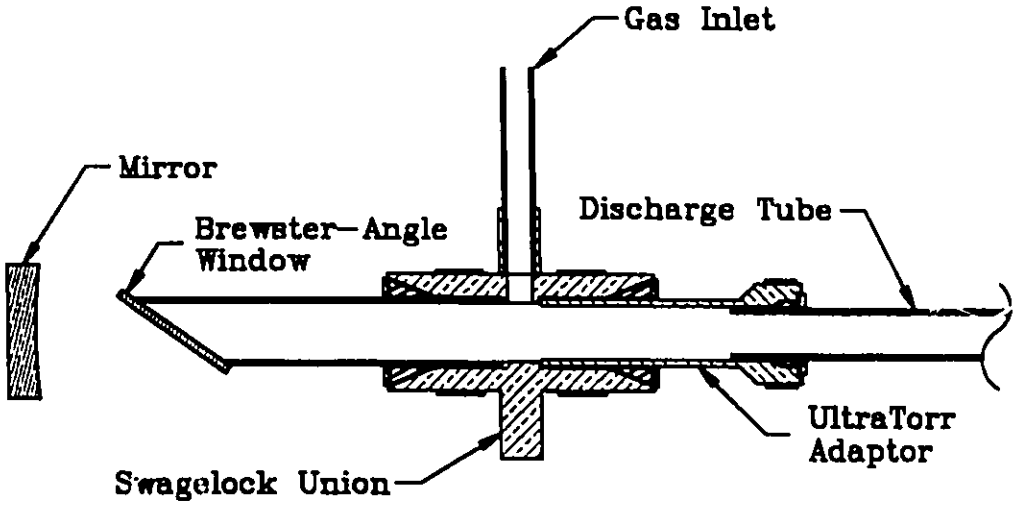

Figure 6.2-1 Cross-sectional view of Brewster-angle window assembly. For clarity, the nuts on the Swagelock and UltraTorr fittings are not indicated. This design allows convenient, reliable interchange of windows.

A detailed cross-section of the Brewster-angle window assembly is given in Fig. 6.2-1. This assembly is built around a 1/2" Swagelock union and a 3/8" UltraTorr adaptor. The union is drilled and a tube is soft-soldered into the hole to provide a gas inlet. The adaptor, bored through along its axis, allows a reliable seal to be made to the fused-silica discharge tube. A short length of brass tube is milled to the appropriate angle and the

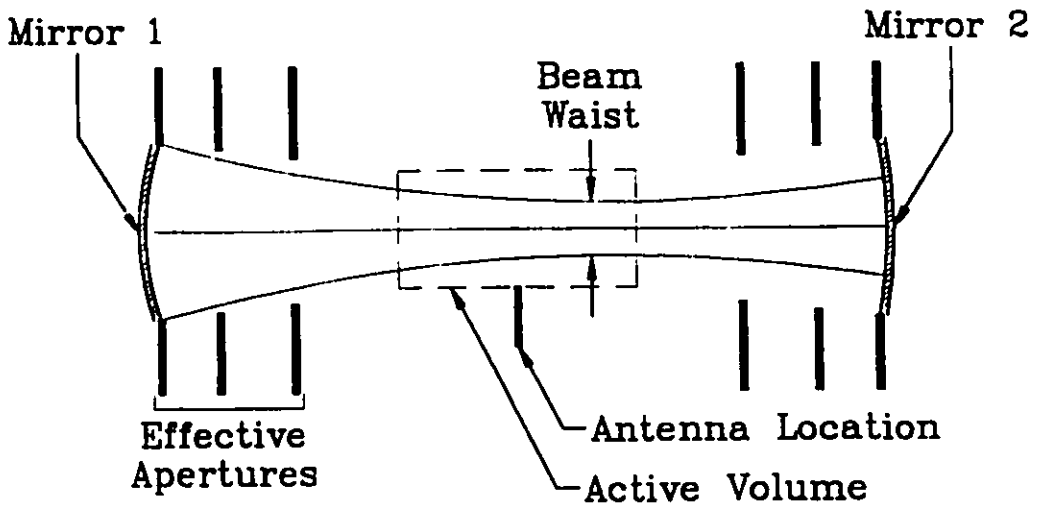

Figure 6.2-2 Schematic view (not to scale) of the optical resonator and TEM_{00} beam profile. The three pairs of effective apertures correspond to (from outside in) the mirrors, the Brewster-angle windows and the ends of the discharge tube. The resonator shown is asymmetric, and Mirror 1 has a smaller radius of curvature than Mirror 2.

Brewster-angle window is fastened to it with epoxy. Teflon ferrules are used to seal the tube and adaptor to the union. The whole assembly is mounted to the optical table using Delrin clamps, which are electrically insulating.

The mirrors are held in position using gimbal mounts (Oriel 14501). A helium-neon laser (Melles Griot 05 LHN 121) is used to aid in mirror alignment. The mirror spacing is set at 130 cm. Different mirrors are used for the two systems; the reflectivity and radius data are given in the appropriate sections. The discharge tube used is 90 cm long and has an inside diameter of 6.5 mm. The mean distance between the Brewster-angle windows is 110 cm.

There are three primary loss mechanisms in an optical resonator: reflection losses, scattering and self absorption by the active medium, and diffraction losses attributable to apertures in the path. Reflection losses include both absorption and transmission; an upper limit is usually specified by the mirror manufacturer. Scattering by the medium is seldom a problem in gas lasers. Self-absorption requires overlapping transitions to occur; for these investigations, this effect is either insignificant or cannot be quantified and is therefore neglected. Diffraction losses, however, are calculable, and further discussion is warranted.

In order to estimate diffraction losses, it is necessary to examine the optical resonator more closely. Figure 6.2-2 shows a schematic view (not to scale) of the optical resonator and the beam profile of the Hermite-Gaussian $TEM_{(00)}$ mode. The design of the optical resonator presents three pairs of effective apertures: the mirrors, the Brewster-angle windows and the ends of the discharge tube. The radii of these apertures are given by a_m, a_w and a_t, respectively. From Fig. 6.2-2, it is clear that only one pair of apertures need be considered (in the case illustrated, the mirror apertures are the limiting factor). An important resonator parameter, the Fresnel number, is defined by

$$N_f \equiv \frac{a^2}{L\lambda}, \qquad (6.2-1)$$

where a is the (limiting) aperture radius, L is the mirror separation and λ is the laser wavelength. The Fresnel number provides a measure of the importance of diffraction for a given situation; the larger its value, the smaller the diffraction losses become.

For the optical resonator described above, the limiting aperture must be moved to the plane of the nearest mirror before calculating the Fresnel number. In order to do this, the beam profile is considered to have a hyperbolic variation in the longitudinal (i.e., z) direction. By phase matching the spherical wavefronts to the curvature of the mirrors, it is

possible to develop the concise formalism that is summarized below (for more detail, see Verdeyen, 1981). The variation in the diameter of the beam is given by

$$w^2(z) = w_0^2\left(1+\left(\frac{z}{z_0}\right)^2\right), \qquad (6.2-2)$$

in which w_0 is the diameter at the beam waist. The parameter z_0 is defined by

$$z_0^2 \equiv \left(\frac{\pi w_0^2}{\lambda}\right)^2 = \frac{L(C_1-L)(C_2-L)(C_1+C_2-L)}{(C_1+C_2-2L)^2}, \qquad (6.2-3)$$

where C_1 and C_2 are the radii of curvature for the mirrors. The mirrors are located at $-z_1$ and z_2 relative to the beam waist ($z = 0$). Using the fact that $L = z_1 + z_2$, it can be shown that

$$z_1 = \frac{L(C_2-L)}{C_1+C_2-2L} \qquad (6.2-4)$$

and

$$z_2 = \frac{L(C_1-L)}{C_1+C_2-2L}. \qquad (6.2-5)$$

The above four equations are used to characterize the spatial extent of the TEM_{00} beam. If the limiting aperture is not that of a mirror, then Eq. 6.2-2 is needed to calculate the limiting aperture radius (i.e., a) and the Fresnel number.

The essential condition for laser oscillation is that the round-trip gain must exceed the total round-trip losses. In gas lasers, spontaneous emission is negligible relative to stimulated emission once oscillation has commenced, and so the oscillation threshold is taken to be the equality of total losses and gain. It is implicitly assumed that the gain is uniform throughout the discharge, and zero elsewhere. Denoting the round-trip gain by G, and the small-signal gain (per unit length) by g, it is evident that

$$G \equiv e^{2gl}, \qquad (6.2-6)$$

where l is the discharge length (and is distinct from the mirror separation, L). Taking into account both reflector and diffraction losses, the threshold condition becomes

$$R_1R_2(1-D)e^{2gl} \geq 1, \qquad (6.2-7)$$

where R_1, R_2 are the mirror reflectances (i.e., power reflection coefficients) and D is the round-trip diffraction loss. It is useful to define an effective reflectance by

$$R \equiv \sqrt{R_1R_2}. \qquad (6.2-8)$$

Using this definition and taking the equality in Eq. 6.2-7, the small signal gain is given by

$$g = -\frac{2\ln R + \ln(1-D)}{2l}. \qquad (6.2-9)$$

6.3 The Carbon Dioxide System

The carbon dioxide laser system is the most efficient and powerful laser system known. It is an example of a molecular laser system, in which excitation takes place via vibrational and rotational transitions, while the electronic structure of the molecule remains in the ground state. The laser transitions have wavelengths in the far infra-red, with the strongest transition at λ = 10.6 μm. This system usually uses a mixture of carbon dioxide, nitrogen and helium. The upper laser level in carbon dioxide is nearly coincident with the first excited state of nitrogen (which is metastable), and it is this fact that accounts for the high efficiencies (> 25%) that are possible in practical devices: a nitrogen molecule that is excited via an electronic collision has a high probability of selectively populating the upper lase: level through a collisional energy transfer. Helium is often the majority gas in a typical mixture. Its effects include discharge cooling (helium has one of the highest thermal conductivities of the gases), collisional depopulation of the lower laser level, and providing a beneficial modification of the electron-energy distribution.

Traditionally, carbon dioxide lasers are excited via DC discharges. Recently, however, there has been a marked trend towards RF operation, particularly in sealed systems that incorporate a waveguiding structure within the optical resonator. Such systems offer several advantages over conventional DC-excited lasers, including higher extractable power density from the gas, longer device lifetimes, greater power stability, lower operating voltages and simplified laser-head construction. Investigation into all aspects of these systems is ongoing; see, for example, Gerasimchuk *et al* (1988), Hill *et al* (1987), Hochuli and Haldeman (1986) and Parazzoli and Chien (1986).

Furthermore, carbon dioxide lasers have been successfully pumped using microwaves, both in a pulsed mode (Handy and Brandelik, 1978) and CW (Freisinger *et al*, 1989). However, in the latter case, supersonic flow of the gas mixture is required to lengthen the discharge and to remove dissociation products (e.g., CO, O_2, N_xO, etc.) from the active medium. To date, CW operation of a sealed microwave-pumped carbon dioxide laser has not been reported. The difficulties associated with achieving such operation are made clear by the results of Section 6.5.

6.4 The Argon-Ion System

The argon-ion laser system is most often used as a CW source of coherent visible and near-UV radiation. For singly ionized argon (i.e., Ar^+), the major laser lines have wavelengths that range from 437.0 nm to 528.7 nm; two very strong transitions have wavelengths of 488.0 nm (blue) and 514.5 nm (green). This is an example of an ionic laser system, which is characterized by laser transitions that take place between the excited states of an ion (not those of a neutral atom). An advantage of this is that lower-level bottlenecking cannot occur because the argon ions have a high rate of recombination, and this causes the lower level to depopulate quickly. A significant disadvantage is the requirement of high levels of excitation to ionize atoms and populate the upper levels. Since the ionization

potential of argon is 15.8 eV, multiple collisions are required to excite the upper levels, and this requires high current densities. Furthermore, the quantum efficiency is low for the same reasons, making this a relatively inefficient system. Commercial lasers typically have efficiencies less than 0.1%.

All commercially-available ion lasers use DC or low-frequency discharge pumping. Typically, a high (> 0.5 Tesla) axial magnetic field is generated to help confine the current (increasing current density and gain) and protect the plasma-tube walls from erosion. The gas fill is usually pure argon at a pressure of several hundred milliTorr. This low pressure increases the electronic mean free path, thus allowing the free electrons to be accelerated to higher speeds before entering into a collision. A plasma power density of 5 kW/cm^3 is typical. The high current (hundreds of Amperes) causes ionic pumping of the gas fill, requiring the inclusion of a return path in the plasma-tube design to prevent a pressure differential from developing. Other design complications include the significant cooling requirements, not only to remove waste heat from the plasma, but also to cool the solenoid that generates the axial magnetic field. Together, these factors explain why a 5-W argon-ion laser typically requires a 208-V, 3-phase, 35-A power supply, weighs over 50 kg and requires 10 l/min of cooling water.

From the above discussion, the motivation to develop an improved excitation scheme is obvious. From this perspective, microwave excitation of an argon-ion laser appears to have potential, and is worthy of serious consideration. In fact, one of the first reported microwave-excited lasers achieved CW oscillation using the argon-ion system. Goldsborough (1966) employed a transverse magnetic field and 2.45-GHz microwave radiation to excite the gas through cyclotron resonance. This is similar to the technique that was used to pump the first microwave-excited gas laser, which was based on the helium-neon system (Ahmed and Kocher, 1964). By adjusting the magnetic field to tune the cyclotron frequency to the applied frequency, the absorption of the microwave radiation by the plasma

can be greatly enhanced. Goldsborough's apparatus made use of a "non-radiating meander line" to cause the electric field to be parallel to the laser axis. Using this configuration, oscillation was obtained on five visible Ar^+ lines, and the threshold power was measured to be 50 W. Microwave pumping of an Ar^+ laser has been demonstrated without an external DC magnetic field; Paik and Creedon (1968) achieved pulsed operation of this system using a modified transmit/receive (TR) tube. Since that time, surprisingly little research has been done to expand upon these encouraging results.

6.5 Experimental

The purpose of these investigations is to set upper limits for the small-signal gain of a microwave-excited discharge for the two laser systems discussed above. The required theory is outlined in the preceding sections. Table 6.5-1 summarizes the essential parameters for the optical resonator for both systems. Details of the diffraction-loss calculations are given individually for each system.

Carbon Dioxide System:

Investigations of this system are described for a number of gas pressures and flow rates. In all cases, the optical resonator has the configuration that is described below.

The total mirror (i.e., Mirror 1) is a front-surface gold reflector having a radius of curvature of 2 m and a usable diameter of 22 mm. Its reflectance is taken to be 99%. The output coupler (i.e., Mirror 2) is a germanium mirror having a 10-m radius of curvature and a usable diameter of 22 mm; its reflectance is measured to be 98% (i.e., ~2% transmission). Monocrystalline sodium chloride Brewster-angle windows (set at 56.0°) are employed to seal the discharge tube. Small (2-W) electric heaters are positioned below the windows in order to prevent damage that is caused by atmospheric moisture. The mirror separation is 130 cm. The essential beam parameters are calculated using Eqs. 6.2-2 to 6.2-5; these

Optical Resonator Data

	CO_2:N_2:He	Ar*
Usable Diameter of Total Reflector, $2a_m$	22 mm	15 mm
Radius of Curvature of Total Reflector, C_1	2 m	∞
Reflectance of Total Mirror, R_1	99%	99%
Usable Diameter of Output Coupler, $2a_m$	22 mm	15 mm
Radius of Curvature of Output Coupler, C_2	10 m	∞
Reflectance of Output Coupler, R_2	98%	97%
Window Material	Monocrystalline NaCl	Fused Silica
Window Aperture, a_w	15 mm	15 mm
Tube Aperture, a_t	6.5 mm	6.5 mm
Mirror Separation, L	130 cm	130 cm
Diffraction Losses[1], D	2%	1%
Effective Reflectance[2], R	98.5%	98.0%

[1]see text for calculation
[2]$R \equiv \sqrt{R_1 R_2}$

Table 6.5-1

parameters are summarized in Table 6.5-2. In this case, the limiting aperture is presented by the end of the discharge tube that is closest to Mirror 1. By (mathematically) moving this aperture to the plane of Mirror 1, it can be shown that the effective limiting aperture is 3.6 mm. This corresponds to a Fresnel number of 0.94. From the relationships that are given in Yariv (1985, p. 108), the round trip diffraction losses are estimated to be 2%.

Beam Parameters: Carbon Dioxide System

Operating Wavelength, λ	10.6 μm
Radius of Curvature of Total Reflector, C_1	2 m
Radius of Curvature of Output Coupler, C_2	10 m
Mirror Separation, L	130 cm
Total Mirror Location, z_1	120.3 cm
Output Coupler Location, z_2	9.7 cm
Beam Waist Diameter, w_0	1.82 mm
Propagation Parameter, z_0	979.13 mm
Limiting Aperture[1], a	3.6 mm
Fresnel Number, N_f	0.94
Diffraction Losses, D	2%

[1]due to end of discharge tube

Table 6.5-2

The mirrors are aligned roughly using the helium-neon laser. In order to facilitate fine tuning of the alignment, the apparatus is designed to be operated as a low-power (DC) CO_2 laser. The Brewster-angle window mounts are electrically insulated from the optical table and other grounded equipment. A high-voltage power supply (Universal Voltronics 60-kV, 20-mA Labtrol) is used (along with 600 kΩ in ballast resistance) to excite a discharge between the brass window assemblies. The duration of such operation is minimized in order to prevent thermal or sputtering damage to laser tube assembly. A CO_2 laser premixture is employed: the gas composition is 22:26:52 (CO_2:N_2:He). At a static pressure of 10 Torr, laser oscillation is observed (by charring paper) when 6 mA of current flows through the discharge; the corresponding discharge voltage is approximately 8 kV. The color of the discharge is dull purplish red under these conditions. With the DC discharge established, the mirror alignment is adjusted to optimize output and TEM_{00} beam quality.

If microwave excitation of the static laser mixture is attempted under conditions analogous to those outlined above, a uniform discharge can be obtained at pressures as high as 15 Torr. However, laser operation is not observed. An obvious difference is that the microwave discharge is a bright blue colour. If DC operation is attempted using the same gas fill, laser oscillation is not observed. Replenishing the gas mixture in the discharge tube allows DC operation of the laser to be repeated. Furthermore, if the gas mixture is allowed to flow through the microwave discharge, the discharge is seen to consist of two regions, a dull purplish red region (upstream) and a bright blue region (downstream). The relative lengths of these regions depend on gas pressure and flow rate. All of these observations indicate that the constituent gases of the laser mixture are permanently dissociated in the microwave discharge, and that the resulting mixture does not support laser operation at 10.6 μm under these conditions.

Because of this apparent impasse regarding operation of a microwave-excited static-fill CO_2 laser, consideration of a flowing system is appropriate: if the gas is replenished quickly enough, pernaps a long enough purplish-red (i.e., active) region can be created for laser oscillation to occur. In order to allow high gas speeds in the discharge tube, it is necessary to decrease the resistance to flow. Accordingly, all the connecting tubing is 3/8" OD (rather than the usual 1/4" OD) for these experiments. Pressure measurements are made using the piezo-resistive transducer that is described in Section 3.4. The transducer is located at the exit of the discharge tube; its readings are taken to represent average pressures within the discharge tube. The gas flow is controlled with a needle valve, and the flow rate is measured with a glass capillary flow meter (Matheson 7631-603). This meter is calibrated by measuring the time required to displace a known volume of water from an inverted flask and correcting the resulting flow rate using the ideal gas law. Average gas speeds are calculated by dividing these flow rates by the cross-sectional area of the discharge tube (i.e., 33.2 mm^2).

For the flowing-gas investigations, a discharge is established at an absorbed power level of 210 W. The total and active lengths of the discharge are measured for flow rates between 2.0 l/s and 3.5 l/s, at pressures ranging from 3 Torr to 25 Torr. The discharge could not be supported at higher flow rates. Oscillation is not reproducibly detectable under any of the investigated conditions. Based on the length of the active region and the gas speed, the time required for the gas to pass through the active region (termed residence time) is easily calculated. The residence time can be considered to be the time required for the gas in the discharge to reach a critical level of dissociation; it ranges from 0.33 ms to 0.84 ms. The power density within the discharge is also easily calculated using the given data; it varies between 16.7 W/cm^3 and 70.3 W/cm^3. Finally, an upper limit on the small-signal gain coefficient can be calculated using Eq. 6.2-9 (in which l is the active length). Under the conditions investigated, at no time did the gain exceed 1.26 %/cm (i.e., 126 %/m). The values for all of these parameters are given in Table 6.5-3.

Gain Investigation Results: Carbon Dioxide System

Gas Pressure (Torr)	3	6	10	15	20	25
Flow Rate (l/s)	2.00	2.00	2.10	2.50	3.38	3.54
Gas Speed (m/s)	60	60	63	75	101	106
Total Discharge Length (mm)	380	330	180	150	110	110
Active Discharge Length, l (mm)	20	25	40	55	90	90
Residence Time (μs)	332	415	632	730	885	844
Total Discharge Volume (cm^3)	12.6	11.0	6.0	5.0	3.7	3.0
Power Density (W/cm^3)	16.7	19.2	35.2	42.2	57.5	70.3
Maximum Small-Signal Gain, g (%/cm)	1.26	1.01	0.63	0.46	0.28	0.28

Table 6.5-3

Argon-Ion System:

In these investigations, dissociation is not a possibility, and so a flowing-gas system is not required. More details of the optical configuration are given below.

The total mirror (i.e., Mirror 1) is a multilayer dielectric reflector (Spectra Physics 020-15) having a reflectance of 99% over the wavelength range 476 nm to 568 nm. The output coupler (i.e., Mirror 2) is also a multilayer dielectric reflector (Spectra Physics 610-3) that has a reflectance of 97% (i.e., ~3% transmission) over the same wavelength range. Both mirrors have a usable diameter of 15 mm and are flat (i.e., have infinite radius of curvature). Fused-silica Brewster-angle windows, at an angle of 55.5°, are used to seal the discharge tube. The mirror separation is maintained at 130 cm. Using Eqs. 6.2-2 to 6.2-5, the beam propagation parameters are calculated. Because the reflectors are flat, the propagation parameter z_0 is infinite and the beam does not diverge (to first order). Thus the limiting aperture is presented by the discharge tube of radius 3.25 mm. Assuming operation is on the 514.5 nm transition, the Fresnel number is 15.8. Again referring to published data (Yariv, 1985, p. 119), the round-trip diffraction losses are found to be 1%. A summary of the beam parameters is given in Table 6.5-4.

Mirror alignment is made using a helium-neon laser. The multilayer dielectric mirrors used have significant transmission at 632.8 nm, and so the alignment procedure is simplified. The mirror angle is adjusted until the multiple reflections from both mirrors are coincident with the optic axis. Unfortunately, the large diameter of the discharge tube precluded DC operation using the window assemblies as electrodes; the currents required for such operation would damage or destroy the apparatus. A smaller discharge tube could not be used; sag in the bore would introduce intolerable optical losses (and the tube could not be properly supported within the microwave resonator). Furthermore, with the available

Beam Parameters: Argon-Ion System

Operating Wavelength, λ	514.5 nm
Radius of Curvature of Total Reflector, C_1	∞
Radius of Curvature of Output Coupler, C_2	∞
Mirror Separation, L	130 cm
Total Mirror Location, z_1	65 cm
Output Coupler Location, z_2	65 cm
Beam Waist Diameter, w_0	6.5 mm
Propagation Parameter, z_0	∞
Limiting Aperture[1], a	3.25 mm
Fresnel Number, N_f	15.8
Diffraction Losses, D	1%

[1]due to end of discharge tube

Table 6.5-4

optics the diffractions losses attendant to a smaller bore (even if it were perfectly aligned) would be too high. Thus the accuracy of the mirror alignment could not be confirmed prior to attempting microwave operation of the laser.

The discharge is established in argon, initially at an absorbed power level of 210 W. Over a range in pressures (from 250 mTorr to 4 Torr), the discharge extends the full length of the microwave gain resonator. Oscillation on either of the strong visible transitions (488.0 nm and 514.5 nm) is not observed under these conditions at any pressure in the above range. Increasing the power (to a maximum of 680 W) does not affect the discharge length, and laser operation is still not achieved. The discharge power densities are in the range 12 W/cm to 40 W/cm. Using Eq. 6.2-9 with the discharge length substituted for l, an upper limit on the small-signal gain is determined to be 4.96 %/m. These results are summarized

in Table 6.5-5.

Gain Investigation Results: Argon-Ion System

Anode Current	100	150	200	250	300[1]	350[1]
Microwave Power (W)	210	310	410	490	585[1]	680[1]
Discharge Length l (mm)	510[2]	510[2]	510[2]	510[2]	510[2]	510[2]
Total Discharge Volume (cm^3)	16.9	16.9	16.9	16.9	16.9	16.9
Power Density (W/cm^3)	12.4	18.3	24.3	29.0	34.6	40.2
Maximum Small-Signal Gain, g (%/m)	4.96	4.96	4.96	4.96	4.96	4.96

[1]above rated maximums for magnetron
[2]independent of discharge pressure over range 250 mTorr to 4 Torr

Table 6.5-5

Conclusions:

Although laser oscillation is not observed for either system, upper limits on the small-signal gain for each system have been determined. In the case of the carbon dioxide system, the major difficulties are the dissociation of the constituent gases and the reluctance of the gases to allow the formation of long discharges at higher pressures (i.e., with total pressures > 10 Torr). Therefore it is doubtful that microwave excitation of sealed carbon dioxide lasers is a viable process. However, in fast-flowing lasers, high-power operation has already been demonstrated (Freisinger *et al*), and research is ongoing to improve the performance of these systems.

Regarding argon-ion systems, it is probable that CW laser oscillation can be achieved without the application of an external magnetic field (to create a cyclotron resonance condition). For the investigations reported here, there is no doubt that the overwhelming deficiency is in the plasma power densities that are achieved. These densities are all less than 50 W/cm^3, whereas DC-excited Ar^+ lasers typically have densities of 5000 W/cm^3. Unfortunately, the author did not have the most suitable equipment (e.g.,

optics and plasma tube) at his disposal for the investigation of this system. However, this investigation has still yielded useful information. The design of the microwave gain resonator has been proven to be suitable for exciting long, uniform discharges at the appropriate pressures. Furthermore, the reported results assist in quantifying what is required for the operation of a CW microwave-excited argon-ion laser.

Chapter 7

Excimer Lamp Applications

This chapter puts the practical uses of excimer lamps in context by providing a brief survey of existing and emerging applications of incoherent UV light sources. Opening with a summary of "conventional" UV sources (i.e., those currently in use), this chapter presents a discussion of their advantages and disadvantages with respect to each other and to the novel microwave-excited excimer lamps. Following this, specific applications from the fields of medical photochemistry, industrial photochemistry, fluorescence diagnostics and microlithography are described. It is hoped that this brief overview will give the reader a sense of the wide-ranging scope and usefulness of excimer-lamp systems. These discussions show that excimer-lamp systems are excellent complements to (and in many cases direct substitutes for) existing UV sources. This chapter is necessarily brief, and a more detailed treatment of applications and sources of UV radiation can be found in the text by Phillips (1983) or that by Wayne (1988). A good reference for microlithography is the text by Elliot (1986).

7.1 Existing Sources of Ultraviolet Radiation

Ultraviolet radiation has long been used in a multitude of fields. Before discussing specific applications, it is instructive to discuss a few of the "conventional" sources of this useful radiation.

Xenon Lamps:

Pure xenon is used as the fill gas in many continuous and pulsed lamp systems. Compared to the other stable noble gases, xenon has the highest molecular weight, the lowest thermal conductivity, the lowest ionization potential (12.1 eV), the lowest first excitation potential (8.3 eV), the highest optical conversion efficiency, and is the most expensive. Because it is a noble gas, xenon does not enter into chemical reactions with either the electrodes or the envelope.

Because the first excitation potential is so high relative to other materials (e.g., mercury), any radiative transition to the ground state will emit in the VUV. Of course, transitions between two excited states are allowed, and they result in longer-wavelength radiation. In fact the most probable transitions are in the near infrared, between 800 nm and 1100 nm, and these transitions are dominant at fill pressures below a few atmospheres. Continuous-wave xenon lamps are usually operated at high pressures in order to produce a spectral continuum. Cold fill pressures near 15 atm are typical, resulting in gas pressures that may reach 60 atm during lamp operation. Lamps that are designed to operate at these pressures are easily recognized by the approximately spherical bulge in the discharge envelope. Typical lamp powers range from tens of watts to tens of kilowatts. In most cases, xenon lamps operate under conditions of high current (up to hundreds of Amperes) and relatively low voltage (tens of volts). In order to withstand the punishment of these conditions, tungsten or tungsten-alloy electrodes are employed.

Relative to other lamps, continuous-wave xenon lamps are fairly inefficient sources of UV and VUV radiation. Their usefulness is confined primarily to applications that require a broadband spectrum that extends into the UV (e.g., solar simulators). For some applications, a small amount of mercury is added to the fill in order to superimpose strong UV transitions on the broadband continuum. Such lamps provide greatly enhanced UV output. More detail about the use of mercury in UV sources is given in the following subsection.

Pulsed xenon sources (i.e., xenon flashlamps) are also popular, both as illumination sources for photography, and for optically pumping dye and solid-state lasers. Because of higher peak powers, the spectral output of such lamps can be significantly shifted towards shorter wavelengths compared to continuous lamps. Thus xenon flashlamps can be quite efficient sources of UV and VUV radiation. In general, a flashtube is filled with several hundred Torr of xenon. A fine wire helix is wound around the tube. To initiate operation, a 25-kV pulse is applied between the helix and one of the main electrodes. The resulting electric field inside the gas is sufficient to provide localized ionization and create free electrons. Simultaneously, a mid-voltage pulse (< 1 kV, from a capacitive storage bank) is applied to the main electrodes. The free electrons are accelerated by the main field, resulting in a self-sustained discharge. The short-wavelength composition of the spectrum is enhanced by shortening the current pulse (thus increasing peak powers) as much as possible. This is accomplished by minimizing the resistance and inductance that is in series with the main electrodes. Increasing this inductance or resistance drastically reduces the UV content of the output.

Mercury Lamps:

By far, the most common application of the mercury lamp is in the ubiquitous fluorescent lighting tube that is used for area illumination in commercial and residential locations. In this application, a low-pressure mercury discharge (with argon or neon buffer gases) is used to produce 253.7-nm radiation with reasonable efficiency. This radiation is converted to a

broad range of visible wavelengths by the fluorescence of inorganic compounds that coat the inside of the glass discharge envelope; any unconverted UV radiation is effectively absorbed by the glass.

As a UV source, the low-pressure mercury lamp is similar to the fluorescent lighting tube, except that the envelope material is fused silica (in order to transmit UV radiation), and the fluorescent coating is eliminated. A typical tube contains a few Torr of buffer gas (e.g., argon and/or neon) and a small quantity of liquid mercury. The vapour pressure of mercury is therefore determined by the operating temperature of the lamp, which is usually near 40° C. The cathode is designed to operate either hot or cold. In the case of a cold cathode, the cathode surface area is large enough that secondary electron emission due to positive ionic bombardment provides enough current to sustain the discharge. In contrast, a hot cathode consists of a tungsten helix (i.e., a heater) that is coated with rare earth oxides to lower the work function of the assembly. This configuration supplies current through thermionic emission. From an operational standpoint, the principle difference between lamps using the two different cathode designs is that the hot-cathode lamp is a high-current, low-voltage device, whereas the cold-cathode lamp is a low-current, high-voltage device.

The spectral output of the low-pressure mercury lamp is primarily radiation from the resonance transitions $6^1P_1 \rightarrow 6^1S_0$ and $6^3P_1 \rightarrow 6^1S_0$, at wavelengths of 185.0 nm and 253.7 nm. The former transition is truly VUV; if the envelope material does not absorb it, then any ambient oxygen outside the discharge envelope will. Typical ionization ratios (i.e., ions:atoms) in the discharge are near 0.1%. Operation with very high current densities and/or electron temperatures increases this ratio, and a ionic transition having wavelength 194.2 nm is observed under those conditions (Johnson, 1974).

An improvement in the performance of the mercury lamp can be obtained by raising the gas-fill pressure to create a medium-pressure mercury lamp. In terms of construction,

the medium-pressure lamp differs from the low-pressure version in many ways. In the former, the electrode assemblies are designed to withstand the formation of an cathode spot, with its attendant high temperatures and high current densities. Such a spot does not form in low-pressure lamps. The assembly usually consists of a thin tungsten wire wrapped around a thoriated tungsten rod, which is coated with rare-earth oxides to lower the work function of the electrode. Lamp operation is almost always AC, so the two electrode assemblies are usually identical.

The vapour pressure of mercury in medium-pressure lamps is determined by the amount of mercury present in the sealed tube, rather than by the operating temperature (i.e., there is no liquid mercury present when the lamp is operating). Typically, the pressure of the buffer gases (e.g., argon, neon, etc.) range from tens of Torr to a few hundred Torr). The operating temperature is much higher than that of the low-pressure lamp. Due to the higher pressure, the discharge does not usually fill the envelope. Instead, the discharge forms a column that is narrower than the tube, and tapers to the electrode spots at each end. The hot discharge has a lower density than the surrounding gas mixture, and so it is buoyant in the tube. This is particularly evident when the lamp is operated in a horizontal position.

Electrodeless Discharge Lamps:

The idea of using radio-frequency or microwave excitation to create a luminous gas discharge is not new to this thesis. Microwave-generated discharges date back to World War II, and RF-generated discharges are older still. However, it has only been since the mid-1950s that these techniques have been used to produce optical sources. Initially, electrodeless discharge lamps were used primarily as specialized analytical sources that had high spectral purity. Wilkinson (1955) describes VUV lamps that use microwave-excited discharges in krypton and xenon. Since that time there has been considerable interest and research in electrodeless discharge lamps, primarily for atomic spectroscopy applications (Dagnall and West, 1968; Mansfield *et al*, 1968), but also as VUV sources (Kikuchi, 1971). Aside from noble gases,

a number of metal vapours (notably mercury) have been used as the active gas. A good review of this technology is given by Haarsma *et al* (1971). High-power (> 300-W) electrodeless discharge lamps have also been available commercially since the mid-1970s. These lamps are obviously very similar to the excimer lamps that are the subject of these thesis, and almost all are excited using 2.45-GHz microwave radiation. Accordingly, they possess all the advantages of microwave-excited sources. Specifically, these advantages are:

(a) By keeping metal electrodes out of the discharge environment, major deterioration processes (e.g., gas clean-up, gas contamination, electrode sputtering) are eliminated completely. Accordingly, device lifetimes are sharply increased over lamps that employ electrodes. Furthermore, the absence of reactive components from the discharge environment means that corrosive or highly reactive gases and vapours can be used in the gas mixture (in order to take advantage of their specific spectral characteristics) while maintaining useful device lifetimes. This aspect is crucial in the case of lamps operating on excimer transitions in halogen-bearing mixtures.

(b) The choice of envelope materials is widened because no glass-to-metal seals are required to make connection to internal electrodes. Highly refractory optical materials, such as beryllia or alumina, can be employed more easily, offering improved performance in some situations due to lower heat capacity, lower susceptibility to chemical attack, higher VUV transmission, higher thermal conductivity and/or higher melting point.

(c) Because electrode connections (which would normally penetrate the discharge envelope) are not required, there is increased flexibility in the design of that envelope and related components (e.g., to provide cooling, to position lenses and reflectors, etc.), and the envelope can be made with thinner walls. Thus

the total thermal mass of "hot" components is lower than in a comparable lamp that employs internal electrodes, resulting in a reduced intensity of infrared radiation for the microwave lamp. This is important in applications for which heat generation is a problem (i.e., an application that involves heat-sensitive materials). The reduced thermal mass of the envelope also results in a much faster cool-off time, which is an advantage for some applications.

(d) For similar reasons as in (c), the warm-up period is faster than for other gas-discharge lamps. With gas mixtures that include metals or other solids that require vapourization, the warm-up period can be several tens of seconds. If the working mixture is entirely gaseous, then the warm-up period is limited by the time required for the magnetron filament to reach its operating temperature, which is usually less than ten seconds. By maintaining filament current when the lamp is off (i.e., providing a "standby mode"), the lamp turn-on time is virtually instantaneous for a purely gaseous fill.

(e) The use of microwaves to accelerate electrons can provide a very uniform discharge (i.e., no positive column or Faraday dark space) that makes efficient use of the space within the discharge envelope. The high-frequency reversal of the electron acceleration precludes processes such as cataphoresis and electrophoresis that can cause a spatial variation of the gas composition and hence discharge non-uniformities. In addition, the high-frequency of the applied field can result in higher electron temperatures and attendant increases in the excitation of higher-energy transitions.

Naturally, there are also a number of disadvantages. These include:

(a) For low-power lamps (< 10 W), the microwave excited systems are huge relative to other units. Even for mid- and high-power units, the microwave-excited systems are larger than comparable "conventional" lamps. In applications with limited space, this can be a significant problem.

(b) Considerable care has to be taken to prevent microwave leakage from the lamps. Typical measures involve a metal screen to shield against microwave leakage while still allowing reasonable optical transmission, or using a lens system to couple the UV radiation out through metal filter tubes, as are used in the author's apparatus.

(c) Magnetrons operate with efficiencies near 70%, and the magnetron power supply itself has an efficiency of approximately 80%. Therefore these components are responsible for a reduction in the wall-plug efficiency of a microwave-excited lamp by a factor of 2.

Other Sources:

The three broad classes of sources given above are the most popular for applications that use UV radiation. Of course, UV lasers (specifically, excimer lasers) are available commercially. However, they are much more expensive than incoherent sources. Regardless, some applications require a source that has high spectral brightness (i.e., high intensity per unit wavelength), high peak-power pulses, and/or coherence. Under these conditions, the increased cost of a laser is justified. However, when the application does not require a source that has these attributes, then an incoherent lamp is usually the most cost-effective option.

Incandescent lamps are also used occasionally as sources of UV radiation. Specific examples include carbon arcs and quartz/halogen lamps, both of which have been used in solar simulators. Other uses of incandescent sources are similar to those already described for the xenon lamps.

7.2 Medical Applications

Phototherapy:

In general terms, phototherapy is the use of light to provide beneficial effects directly to living tissue. Because of the efficient absorption of UV radiation by tissue, the area affected is almost always the skin. Ultraviolet radiation is germicidal, and so it can be used as a topical antibiotic to treat skin disorders that involve infection, such as acne vulgaris or eczema.

Photochemotherapy:

Photochemotherapy is a much more powerful and flexible technique than phototherapy. Rather than relying on the direct effect of the radiation, photochemotherapy uses the radiation to convert relatively inert compounds (precursors) to reactive compounds at the irradiation site. It is the products of these reactions that provide the beneficial effects, either at the irradiation site or at some other location. A good example is the natural process that is required to supply cholecalciferol (vitamin D_3) to the human body. In this case, the precursor is 7-dehydrocholesterol, which is brought to the skin and converted at that location into previtamin D_3 in a reaction that is driven by the local absorption of UV radiation. A subsequent reaction converts the previtamin D_3 into vitamin D_3, which in turn is redistributed throughout the body. In geographic locations where children do not receive enough exposure to sunlight, improper bone development (i.e., rickets) is often the result, unless a dietary source of vitamin D_3 is provided.

The effects of photochemotherapy do not have to be at a different location from the radiation site, nor does the precursor have to be provided naturally. In particular, psoriasis (a skin disorder) can be effectively treated using photochemotherapy. Either a topical or systemic precursor is used, and is activated using UV radiation. In the former, the precursor is dithranol, which is applied directly to the affected region before irradiation. The latter is more sophisticated technique. The precursor, usually a psoralen, is introduced orally. After allowing the drug to become distributed systemically, the affected area is irradiated, thus photoactivating the psoralen. Research is ongoing to develop new procedures for other disorders that may be effectively treated using a similar regime. The development of systemic photosensitive drugs in conjunction with surgical irradition methods could prove to be an effective treatment for internal disorders, such as some types of cancer.

7.3 Industrial Photochemistry

Ultraviolet radiation is also used to drive or initiate chemical reactions for industrial applications. These applications include the manufacture of chemicals and pharmaceuticals, polymerization, and photocuring of paints and resins. In addition, UV irradiation can be used for the sterilization of many substances (e.g., potable water production).

Large Scale (High Volume) Production:

Large scale production implies a large throughput, so that the marginal cost of the irradiation equipment is minimized. The photochemical reactors are most often designed for continuous (rather than batch) operation. The cost of the feedstock is low, and an efficient process is required. This type of process is shown in its best case by the exothermic photochlorination reactions that usually proceed via the following chain-reaction pathway:

$$h\nu + Cl_2 \rightarrow 2Cl \cdot$$

$$Cl \cdot + RH \rightarrow R \cdot + HCL$$

$$R \cdot + Cl_2 \rightarrow RCl + Cl \cdot$$

A single photon may result in up to 1000 reactions of this type (Wayne, 1988, p. 245), allowing a small source and reactor to have an appreciable output. The valuable chemicals benzyl chloride, benzylidene dichloride and benzotrichloride can be produced via the photochlorination of toluene. In these reactions, the methyl group undergoes a substitution of chlorine for hydrogen, while the aromatic ring is left unaffected. Other large scale processes that are similar to photochlorination include photohydrosulphonation, photosulphochlorination and photonitrosation. A brief discussion of each of these can be found in the text by Phillips (1983).

Polymers are structures that are formed as an assembly of monomers, which themselves are relatively simple molecules. There are two different ways that monomers are joined to create a polymer: linear and cross-linked. If the polymer largely consists of linear chains, then that polymer will have thermoplastic properties; that is the material can be physically distorted and moulded through the application of heat and/or pressure. Polyvinylchloride, polyethylene, polypropylene, polystyrene, nylon and acrylic are all examples of thermoplastic polymers. Because these materials can be moulded and remoulded, they are commonly produced as powders or grains that are subsequently shaped into final products. In spite of considerable academic interest, it appears that photopolymerization is not economically competitive with other methods for the manufacture of thermoplastic polymers. Because existing catalytic and thermal techniques are so efficient, the additional expense and complexity associated with the irradiation equipment is not warranted.

Photochemical Hardening:

In contrast to thermoplastic polymers, thermosetting (i.e., cross-linked) polymers do not soften when heat is applied. Instead, these polymers remain hard with increasing temperature until their chemical structure is ultimately destroyed. For this reason, thermosetting polymers must be cast or formed at the time they are fabricated. In the case of a thin layer upon a substrate (i.e., a coating), photochemical techniques are eminently practical to induce or accelerate polymerization.

Examples of these processes include UV "drying" (i.e., hardening) of inks, protective coatings, photoresists, and even dental resins. Conventional (i.e., thermal) drying or curing techniques have appreciable disadvantages. Excess solvents are normally required to reduce the viscosity of the coating compound to allow uniform application; the evaporation of these solvents is required to produce the finished surface, and the solvents are therefore unrecoverable. The thermal mass of the substrate is usually orders of magnitude larger than that of the coating, yet the entire substrate/coating assembly must be heated to the required temperature if purely thermal techniques are employed. Often, there are several coating layers, and the required temperature cycling adds to this energy expense. Photochemical curing alleviates both of these problems; the only solvents employed are those that are required to participate in the relevant polymerization reactions. Furthermore, the coating can be hardened efficiently because of its high absorption of UV radiation. If one considers a large scale process, such as the painting of automobiles, it is clear that photochemical techniques can offer significant advantages in terms of reducing environmental solvent emission, energy costs and processing time.

Small Scale (Specialized) Chemical Production:

Small scale production is most suitable for fine chemicals. Typically, the marginal cost of

the feedstock is considerably higher than for large scale production, whereas the costs of the irradiation equipment are relatively low. Thus the value of the final product must be high in order to justify this mode of production.

Pharmaceuticals and related chemicals are examples of the types of products that are synthesized on a relatively small scale. The exogenous synthesis of vitamin D_3, which is used as a veterinary nutrient, is typical of fine-chemical production. In this process, which is similar to its natural counterpart, cholesterol is first converted to 7-dehydrochlosterol. Upon UV irradiation, this latter compound experiences an "electrocyclic ring opening" (Wayne, 1988, p. 247), and forms pre-vitamin D_3. This precursor is subsequently converted to vitamin D_3 via a thermal process.

7.4 Fluorescence Diagnostics

Fluorescence-based techniques are usually more sensitive than other optical methods that are used to detect extremely small quantities of certain substances. This is so because much higher levels of contrast are possible than are available with absorption techniques; if the exciting radiation has a distinct spectral band from the emitted fluorescence, then the contrast is limited only by the detector. Detectors that are sensitive to single photons are available (e.g., photomultipliers, avalanche photodiodes, even the dark-adapted human eye), and the minimum detectable power levels are constrained by the noise levels due to fundamental processes. While these techniques are used for medical, dental and industrial diagnostic investigations, perhaps the most novel practical application is forensic.

Forensic Diagnostics and Identification:

Since the mid-1970s, short-wavelength visible lasers have come to be used to induce fluorescence in various substances from crime scenes in order to discover evidence that would otherwise go unnoticed. Typically, 488-nm radiation from a high-power argon-ion

laser is used to illuminate a sample. Simultaneously, the sample is viewed in order to detect yellow fluorescence from any residual substances that may be present. Most notably, untreated latent fingerprints have been reliably detected using such techniques. The argon-ion laser is favoured because of the high levels of contrast that it affords; it is a virtually monochromatic source, and so darkening the room is sufficient to make the weak yellow fluorescence detectable to the unaided eye. Treatment of the suspected articles with cyanoacrylate vapours increases the fluorescence efficiency and the success rate of the technique.

Due to the physical size of the argon-ion laser, these measurements cannot be performed *in situ*, rather the evidence must be small enough to transport to a suitably equipped forensic laboratory. While transportable argon-ion lasers (which have output powers of the order of 200 mW) do not provide satisfactory results, a portable filtered arc-lamp source has been developed (Watkin and Misner, 1990) that emits 15 W of blue light. This source has proved suitable for on-site forensic applications in many practical cases. While this source is not designed to emit appreciable levels of UV radiation, UV sources are of significant use for forensic applications. In their conclusions, Watkin and Misner (1990) indicate that "strong light sources of various wavelengths will be one of the primary tools of the specialist searching for crime scene evidence."

7.5 Microlithography

Integrated-circuit (IC) fabrication technology encompasses all aspects of creating controlled layers of various materials on a substrate wafer. These aspects include: production of the wafer itself (i.e., crystal growth, slicing and polishing), mask (i.e., pattern) creation, application of a photoresist to the wafer, transferal of the desired pattern to the photoresist, developing, etching, doping, evaporation (or other deposition processes) and packaging. Microlithography is the accurate reproduction and transferral of a pattern, usually from a

mask to a resist-coated wafer, that takes place on a small dimensional scale. In many ways, microlithography is the limiting process in achieving high feature densities (per chip) and high chip densities (per wafer). Thus improvement in the ability to accurately reproduce small features on a wafer (i.e., resolution) increases both the possible complexity of ICs and the chip production throughput.

Historically, the other aspects of IC fabrication technology have developed largely in response to the microlithographic capabilities that existed at the time. The current limitations on feature size stem from limitations in the imaging aspect of the microlithographic process. Resolution limits are inherent to the wave nature (i.e., diffraction) of the beams that are used to "write" the patterns. In order to improve resolution, it is necessary to decrease the wavelength of the beams.

Essentially, there are two general categories of microlithographic imaging, optical and non-optical. As the name implies, optical imaging relies on visible and UV radiation sources, whereas non-optical imaging employes particle beams and X-rays. While non-optical imaging has been demonstrated to offer the best resolution, the expense, complexity and slow speed of the method (on a per-wafer basis) limits its use in mainstream and volume IC production.

Only projection printing techniques are of interest here. Other techniques, such as contact or proximity printing, are of limited use for very large scale integration (VLSI) production. Projection printing allows the image of the surface features to be projected onto the substrate, which can be located centimeters from the mask. A measure of the resolution of the system is given by the minimum width of a feature (l_{min}) that can be successfully imaged. which is

$$l_{min} \approx \frac{\lambda}{NA}, \qquad (7.5-1)$$

mask to a resist-coated wafer, that takes place on a small dimensional scale. In many ways, microlithography is the limiting process in achieving high feature densities (per chip) and high chip densities (per wafer). Thus improvement in the ability to accurately reproduce small features on a wafer (i.e., resolution) increases both the possible complexity of ICs and the chip production throughput.

Historically, the other aspects of IC fabrication technology have developed largely in response to the microlithographic capabilities that existed at the time. The current limitations on feature size stem from limitations in the imaging aspect of the microlithographic process. Resolution limits are inherent to the wave nature (i.e., diffraction) of the beams that are used to "write" the patterns. In order to improve resolution, it is necessary to decrease the wavelength of the beams.

Essentially, there are two general categories of microlithographic imaging, optical and non-optical. As the name implies, optical imaging relies on visible and UV radiation sources, whereas non-optical imaging employes particle beams and X-rays. While non-optical imaging has been demonstrated to offer the best resolution, the expense, complexity and slow speed of the method (on a per-wafer basis) limits its use in mainstream and volume IC production.

Only projection printing techniques are of interest here. Other techniques, such as contact or proximity printing, are of limited use for very large scale integration (VLSI) production. Projection printing allows the image of the surface features to be projected onto the substrate, which can be located centimeters from the mask. A measure of the resolution of the system is given by the minimum width of a feature (l_{min}) that can be successfully imaged, which is

$$l_{min} \approx \frac{\lambda}{NA}, \qquad (7.5-1)$$

where λ is the optical wavelength and NA is the numerical aperture. If air is the medium between the substrate and the lens, the numerical aperture is

$$NA = \sin\theta, \tag{7.5-2}$$

where θ is the half-angle of the cone of light that is formed by the lens. Another important quantity is the depth of field

$$\Delta z = \pm\frac{\lambda}{2(NA)^2}. \tag{7.5-3}$$

Practically, the depth of field is a measure of the required accuracy in the positioning of the wafer and mask from the lens. In order to allow greater tolerances in positioning, the depth of field should be maximized.

As an example, consider the case of a lens with a numerical aperture of 0.49 (i.e., a full vertex angle of 59°). If the optical wavelength is 500 nm, then Eq. 7.5-1 indicates that the resolution is 1.02 μm and the depth of field is (by Eq. 7.5-3) 1.04 μm. The resolution can be improved by a factor of two (i.e., $l_{min} = 0.501\mu m$) by either doubling the numerical aperture or halving the optical wavelength. The former approach leads to the requirement of a lens that has a full vertex angle of 157°. Such a lens is difficult and expensive to construct, and the reflection losses towards the edges of the lens would become excessive (the rays are near grazing incidence). Furthermore, the depth of field has been reduced to a value of 0.26 nm. However if the numerical aperture is kept at 0.49 and the optical wavelength is reduced to 250 nm, the problems with the lens are avoided. Moreover, the depth of field is only reduced to 0.52 μm. It is clear from this example that the best way to reduce feature size is to maintain a reasonable numerical aperture and decrease the optical wavelength as much as possible.

To this point, the optical source that is used for the lithography has been implicitly assumed to be monochromatic. In the case of single-line laser sources (e.g., 488-nm Ar^+),

this is a good assumption. However, if the source is a lamp that is either broadband or multi-line then an additional complication can result. Chromatic aberrations are focussing defects that occur in optical systems that employ refractive optics. These aberrations are due to the fact the refractive index of a dielectric varies with wavelength, and therefore a lens will have a focal length that varies with wavelength. Actual calculations are quite involved and cannot be made without referring to a specific lens design, and so they are not attempted here. If the range of wavelengths is large enough, chromatic aberrations can impose a limit upon feature size that is greater than that due to diffraction alone. One approach to avoid this situation involves using pass-band filters in order to narrow the transmitted spectrum of the source. In practice, this results in a compromise between power and bandwidth; lower transmitted power levels mean that exposure time is lengthened and the required levels of mechanical stability are increased accordingly. From these considerations, it is clear that the best incoherent sources will have relatively narrow linewidths so that the use of a pass-band filter will not excessively reduce the absolute transmitted power.

Chapter 8

Conclusions and Suggestions for Further Research

In this concluding chapter, the results that are described in previous chapters are re-iterated and summarized. All of the objectives that are given in Chapter 1 have been attained. These four objectives are repeated here, and brief descriptions of the corresponding results are given for each. There remains an enormous amount of research to be undertaken in this field; many of these potential studies extend directly from the work completed in this thesis. Ideas regarding expansions upon this research are put forth in Section 8.2.

8.1 Summary of Results

1) *To investigate and develop novel ways of coupling microwave power to a gas discharge so as to produce extractable optical power.*

Closed resonant structures are of the most interest in order to control microwave leakage. Characterization of the final design(s) is also required.

Two different microwave resonators have been designed, constructed and characterized. The lamp resonator operates in the TE_{102} mode and its operating parameters (e.g., resonant frequency) are relatively insensitive to dimensional tolerances. This resonator has a measured quality factor of 620, and provides a coupling efficiency in excess of 93% under the investigated experimental conditions. The design allows ample optical and physical access to the cavity through filter tubes and end-wall sliders (the latter of which are also used to adjust the resonant frequency). These design techniques have been proven, both experimentally and theoretically, to keep microwave leakage to acceptable (and usually undetectable) levels.

The gain resonator operates in the TE_{101} mode. Because operation is so close to cutoff, the resonator is actually several free-space wavelengths long. The operating parameters of this design are extremely sensitive to dimensional tolerances, but this only presents a difficulty in the theoretical characterization of the structure; experimentally, the electrical behaviour of this design is reliable and reproducible. Using this structure, 0.5-m long plasma columns can be easily generated in argon at total pressures that are appropriate for laser operation; the resulting plasmas are spatially uniform along all three axes. Due to its operation near cutoff, the gain resonator has a quality factor of nearly 1000, and provides a coupling efficiency of ~93%. An extensive array of 1/16" holes in the side wall of the resonator allow a good view of the discharge. As before, end-wall sliders are used, both to allow physical access to the interior of the resonator, and to tune the resonant frequency.

2) *To characterize a microwave-excited gas discharge in terms of observable parameters.*

In order to be of practical use, characterization must be in terms of parameters that are either directly observable or readily calculable. In cases in which these conditions are not fulfilled but a reasonable estimate can be made, the characterization may be made based on the estimated parameters.

Microwave discharges in the five noble gases were characterized using techniques that require little sophisticated equipment. The primary observable parameter is the sheath thickness in the plasma; this quantity is directly related to skin depth. Starting largely from first principles, the propagation of microwaves through a plasma was considered in order to develop the required specialized theory. Specifically, relationships for the electron density and plasma frequency as a function of collision frequency were developed in terms of applied frequency and skin depth. The collision frequency was calculated from known or measured parameters. Using these techniques, the following parameters were measured or deduced as a function of pressure for each of the gases: skin depth, electron density, ionization coefficient, peak electric-field intensity and the collisionless electron energy.

3) *To investigate continuous-wave excimer fluorescence from microwave-excited gas mixtures that contain halogens and rare gases.*

Three distinct types of excimer transitions are of interest: rare-gas/halide, homonuclear halogen, and heteronuclear halogen.

Truly continuous excimer fluorescence can be achieved by exciting binary- and single-gas mixtures with 2.54-GHz microwaves. In the case of the binary mixtures, such fluorescence was conclusively identified from the 207-nm B→X and 222-nm C→A transitions of KrBr; the 222-nm B→X transition in KrCl; and the 308-nm B→X and 236-nm D→X transitions of XeCl. In addition, strong homonuclear excimer emission can be obtained from molecular Cl_2 at 258 nm and from molecular Br_2 at 293 nm. Excimer transitions due to heteronuclear species, such as BrCl, were not detected in discharges consisting of binary halogen mixtures.

Additional investigations were completed for those gases that produced exceptional excimer emission. The effect of gas composition on excimer fluorescence was examined for KrCl and XeCl. Furthermore, the effect of total gas pressure on excimer fluorescence was investigated for KrCl, XeCl and Cl_2 over the pressure range 0 Torr to 100 Torr.

The optimum composition and pressure for 308-nm (B→X) fluorescence was determined to be 40:60 ($Xe:Cl_2$) at 40 Torr. From the spectra, the B→X transition is considerably stronger than the D→X transition. The B→X transition has a FWHM of 8 nm, while that of the D→X is 6 nm. In addition, a 258-nm molecular chlorine transition (FWHM 8 nm) was observed in all spectra.

For $Kr:Cl_2$ mixtures having ratios of 80:20, 60:40, 40:60 and 20:80, the pressures for maximum B→X KrCl fluorescence were found to be near 50 Torr, 30 Torr, 10 Torr and 30 Torr, respectively. In all four cases, spectra were presented over the wavelength range 200 nm to 360 nm. The 222-nm KrCl B→X excimer fluorescence was always evident, as was the 258-nm molecular chlorine transition. The FWHM is 3 nm and 5 nm for the B→X KrCl and molecular Cl_2 transitions, respectively. Both the center frequencies and widths of these transitions were constant over the tested conditions.

The effect of total pressure on the molecular Cl_2 emission was investigated for pure chlorine. It was evident that the optimum pressure for 258-nm excimer fluorescence is near 35 Torr. The corresponding spectrum is dominated by a single strong peak at 258 nm that has a FWHM of ~8 nm, although there is some broad fluorescence between 220 nm and this peak.

Because of the relatively strong emission and narrow linewidths, a lamp based on any of the above transitions could be useful as a high-power UV source.

4) *To investigate the possibility of pumping a gas laser with microwaves.* Although laser operation was not reproducibly demonstrated during this research, experiments into the creation of a microwave-pumped gas laser allow upper limits on gain in a microwave discharge to be deduced. The carbon dioxide and argon-ion systems are of particular interest.

The gain resonator (which is described above) was used to investigate the production of gain in a carbon dioxide laser-mixture discharge and in an argon discharge. In the case of the carbon dioxide investigations, an optical resonator was constructed to minimize optical losses. Alignment was confirmed by operating a DC carbon dioxide laser using the Brewster-angle window assemblies as electrodes. A CO_2 laser premixture having a 22:26:52 (CO_2:N_2:He) gas composition was employed. It was noted that the microwave discharge causes permanent dissociation of the constituent gases. Therefore, a fast-flowing system was constructed and investigated with flow rates ranging from 2.0 l/s to 3.5 l/s and with total pressures ranging from 3 Torr to 25 Torr. The active length (i.e., the length of the discharge that produces useful gain) was determined from the colour change between the upstream (i.e., dull red) and downstream (i.e., bright blue) portions of the discharge. Based on this information, an upper limit on the small-signal gain was determined to be 1.26 %/cm under the investigated conditions. Furthermore, the time required for the dissociation of the gas mixture to reach a critical level was determined to range from 0.33 ms to 0.84 ms.

The argon-ion system was investigated under static conditions using pure argon. A low-loss optical resonator was again constructed using multilayer dielectric reflectors. Using the gain resonator, a full-length discharge (i.e., 0.5 m) was obtained over the pressure range 250 mTorr to 4 Torr. The power densities achieved in the discharge ranged from 12 W/cm^3 to 40 W/cm^3. Under these conditions, the upper limit for the small-signal gain was found to be 4.96 %/m. It is clear that laser operation was not observed for this system because of the low power densities obtained; commercial argon-ion lasers typically have plasma power densities of the order of 5000 W/cm^3.

8.2 Suggestions for Further Research

In spite of its long history, the research area of microwave-excited optical sources is not yet mature. Many possibilities exist for future studies, and a few of these are outlined below. The more recent advances, such as the observation of microwave-excited CW excimer fluorescence that was first observed by the author, will probably be those that develop most quickly. For clarity, the suggestions are given in the same order and format as the original four objectives.

1) Coupling microwaves to gas discharges: specialized resonator design.

In this course of this thesis, two viable microwave resonator designs were developed. The quality factor with no discharge present was measured reliably, but the measurement of the quality factor with a discharge was not so reliable. These measurements were used to calculate the coupling efficiency and the DC coupling efficiency for the device. A superior method of determining these two values involves using a length of transmission line or waveguide to separate the magnetron from the resonator. Directional couplers in the connecting structure would allow the incident and reflected power to be measured directly. The coupling efficiency could be determined easily from the measured values. This type of apparatus could be calibrated, for example, by heating a known quantity of water. Following calibration, absolute power measurements could be made and the DC coupling efficiency could be calculated accurately.

For laser and lamp applications, acceptable performance can be achieved using resonator designs similar to those that were described in this thesis. Because the required cavity dimensions are now known, construction of these resonators is simplified because the waveguide width can be fixed. In addition, some improvements can be incorporated, such as including a separate micrometer-based tuning adjustment, and electroplating the

resonator to decrease Ohmic losses. Given well-defined performance criteria, it is possible to design a microwave resonator that is so insensitive to dimensional tolerances that no tuning is required, even in the case of operation near cutoff.

2) Characterization of a microwave-excited discharge.

Almost all recommended improvements to this aspect of the research require the use of sophisticated equipment. There are many techniques that the author could not employ due to limitations in the instrumentation available. For example, a spatially dependent spectroscopic analysis of emission from known atomic transitions in the discharge could be used to map the discharge temperature as a function of position (in three dimensions). Average electron densities could be measured using a Twyman-Green or Mach-Zehnder interferometer. With a high-power network analyzer, phase-shift measurements could be made that provide a basis for calculating the real part of the wavenumber, k'. In addition, the attenuation due to the plasma could be measured directly in order to verify the skin depth measurements reported in this thesis. Finally, there are a number of similar microwave techniques that can be used to better characterize the discharge. A good overview of some of these methods is given in the text by Heald and Wharton (1965).

3) Microwave-excited excimer lamps.

There remains much work to be done on these systems. From a basic physics perspective, tremendous opportunities exist. The low-pressure formation of excimer species allows an examination of their physical properties in a regime in which collisions are relatively infrequent. Linewidths, lifetimes, transition probabilities, cross-sections and other basic parameters should be determined for these new conditions. The continuous nature of the fluorescence means that the resolution, reproducibility and accuracy of these types of measurements are enhanced.

From an engineering perspective, there are again great research opportunities. Development of a commercially-viable UV lamp system is a definite possibility. However, several fundamental measurements must be completed first. In particular, overall conversion efficiencies should be measured for the various transitions. These measurements require calibrating the monochromator and other optical components so that the absolute power can be determined. Also, device lifetime measurements need to be performed, both for sealed and quasi-sealed systems. Optimization of the device lifetime will require extensive investigations to determine the best envelope material, gas composition and envelope volume for a given system. In sealed systems, there is the added complexity of developing a reliable ignition system, since lowering the total pressure to establish the discharge is not a possibility.

4) Microwave-excited gas lasers.

This is another exciting research field that is directly related to this thesis. Given the required optics and a smaller volume discharge tube, the prospects for successfully pumping a CW atomic-ion laser (e.g., Ar+ or Kr+) are excellent. It is quite possible that such systems could be commercially viable, since the complexity associated with a solenoid is eliminated because a DC magnetic field is not required. Other laser systems could also use a microwave-excited discharge as the gain medium. In particular, systems with relatively low quantum efficiencies are attractive (e.g., helium-cadmium and other CW metal-vapour lasers) because of the enhanced electric fields and electron energies that are present in a low-pressure microwave discharge. Although a great deal of research and development is required to make such devices a practical reality, it is the belief of the author that these efforts are well justified by the benefits that microwave excitation offers.

References

Ahmed S.A. and R. Kocher; "Microwave Electron Cyclotron Resonance Pumping of a Gas Laser" *Proc. IEEE* **52**, pp. 1737-1738, 1964.

Ault, E.R.; R.S. Bradford and M.L. Bhaumik; "High-power xenon fluoride laser" *Appl. Phys. Lett.* **27**(7), pp. 413-415, 1975.

Ballik, E.A.; *Experiments with Coherent Radiation.* Doctor of Philosophy Thesis. Oxford: Oxford University, 1964.

Brandelik J.E. and G.A. Smith; "Br, C, Cl, S, and Si Laser Action Using a Pulsed Microwave Discharge" *IEEE J. Quantum Electron.* **QE-16**(1), pp. 7-8, 1980.

Brau, C.A. and J.J. Ewing; "354-nm laser action on XeF" *Appl. Phys. Lett.* **27**(8), pp. 435-437, October 1975.

Brau, C.A. and J.J. Ewing; "Emission spectra of XeBr, XeCl, XeF, and KrF" *J. Chem. Phys.* **63**(11), pp. 4640-4647, December 1975.

Brown, R.G.; R.A. Sharpe; W.L. Hughes and R.E. Post; *Lines, Waves and Antennas: The Transmission of Electric Energy.* Second Edition. New York: John Wiley & Sons. 1973.

Busch, K.W. and T.J. Vickers; "Fundamental properties characterizing low-pressure microwave-induced plasmas as excitation sources for spectroanalytical chemistry" *Spectrochimica Acta*, **28B**, pp. 85-104, 1973.

Christensen, C.P. and R.W. Waynant "200-MHz electrodeless discharge excitation of an XeF laser" *Appl. Phys. Lett.* **41**(9), pp. 794-796, 1982.

Christensen, C.P. and R.W. Waynant and B.J. Feldman "High efficiency microwave discharge XeCl laser" *Appl. Phys. Lett.* **46**(4), pp. 321-323, 1985.

Dagnall, R.M. and T.S. West; "Some Applications of Microwave-Excited Electrodeless Discharge Tubes in Atomic Spectroscopy" *Appl. Opt.* **7**(7), pp. 1287-1294, 1968.

Edminster, J.A.; *Theory and Problems of Electromagnetics.* Schaum's Outline Series in Engineering. New York: McGraw-Hill Book Company, 1979.

Elliot, D.; *Microlithography: Process Technology for IC Fabrication.* New York: McGraw-Hill Book Company, 1986.

Ewing, J.J. and C.A. Brau; "Laser action on the $\Sigma^{2+}_{1/2} \rightarrow \Sigma^{2+}_{1/2}$ bands of KrF and XeCl" *Appl. Phys. Lett.* **27**(6), pp. 350-352, September 1975.

Ewing, J.J. and C.A. Brau; "Laser action on the 342-nm molecular iodine band" *Appl. Phys. Lett.* **27**(10), pp. 557-559, November 1975.

Fraga, S.; J. Karwowski and K.M.S. Saxena; *Handbook of Atomic Data.* Amsterdam: Elsevier Scientific Publishing Company, 1976.

Freisinger, B.; J.H. Schaffer; J. Uhlenbusch and Z.B. Zhang; "Investigation of a 1-kW CO_2 laser excited by microwaves" *Summaries of Papers Presented at the Conference on Lasers and Electro-Optics.* Piscataway, NJ: IEEE Service Center, 1989.

Gerasimchuk, A.; S. Kornilov and I. Protsenko; "Nearly 1 GHz Frequency Tuning Range RF Excited Waveguide CO_2 Laser" *Opt. Comm.* **66**(2,3), pp. 149-151, 1988.

Goldsborough, J.P. "Cyclotron Resonance Excitation of Gas-Ion Laser Transitions" *Appl. Phys. Lett.* **8**(9), pp. 218-219, 1966.

Haarsma, J.P.S.; G.J. De Jong and J. Agterdenbos; "The preparation and operation of electrodeless discharge lamps--A critical review" *Spectrochimica Acta*, **29B**, pp. 1-18, 1974.

Handy, K.G. and J.E. Brandelik; "Laser Generation by pulsed 2.45-GHz microwave excitation of CO_2" *J. Appl. Phys.* **49**(7), pp. 3753-3756, 1978.

Hassal, S.B.; *Considerations in the Design and Operation of a Triggered, Three-Electrode Spark Gap.* Master of Engineering Thesis. Hamilton: McMaster University, 1988.

Hassal, S.B. and E.A. Ballik; "Observation of Continuous D→X and B→X XeCl Excimer Fluorescence in a Binary-Gas Microwave Discharge" *J. Appl. Phys.* Manuscript Submitted November, 1990. Accepted for Publication.

Hassal, S.B. and E.A. Ballik; "Observation of Continuous KrCl Excimer Fluorescence in Microwave Discharges Employing Binary Mixtures of Kr and Cl_2" *Can. J. Phys.* Manuscript Submitted January, 1991. Accepted for Publication.

Hays, A.K.; J.M. Hoffman and G.C. Tisone; "Molecular-Iodine Laser" *Chem. Phys. Lett.* **39**(2), pp. 353-357, 1976.

Heald, M.A. and C.B. Wharton *Plasma Diagnostics with Microwaves.* New York: John Wiley and Sons Inc. 1965.

Hill C.A.; P. Monk and D.R. Hall; "Tunable RF-Excited CO_2 Waveguide Laser with Variable Guide Width" *IEEE J. Quantum Electron.* **QE-23**(11), pp. 1968-1973, November 1987.

Hochuli, U.E. and P.R Haldemann: "Life problems of dc and rf-excited low-power cw CO_2 waveguide lasers" *Rev. Sci. Instrum.* **57**(9), pp. 2238-2241, 1986.

Johnson, P.D.; "Excitation of Hg^+ 1942 A in the High-Current-Low-Pressure Discharge" *Appl. Phys. Lett.* **18**, pp. 381-382, 1971.

Kikuchi, T.T. "Description and Analysis of a Vacuum Ultraviolet Atomic Line Source" *Appl. Opt.* **10**(6), pp. 1288-1295, 1971.

Kravchenko, V.F.; V.S. Mikhalevskii; S.P. Chubar and A.P. Shelepo; "Ion laser utilizing microwave-excited strontium vapor" *Sov. J. Quantum Electron.* **14**(6), pp. 725, 1984.

Kumagai, H. and M. Obara; "A High-Efficiency, High-Repetition-Rate KrF(B-X) excimer lamp excited by microwave discharge" *Japan. J. Appl. Phys.* **28**(12), p. 2228-2231, July 1989.

Kumagai, H. and M. Obara; "New high-efficiency quasi-continuous operation of a KrF(B-X) excimer lamp excited by microwave discharge" *Appl. Phys. Lett.* **54**(26), p. 2619-2621, June 1989.

Kumagai, H. and M. Obara; "New high-efficiency quasi-continuous operation of a ArF(B-X) excimer lamp excited by microwave discharge" *Appl. Phys. Lett.* **55**(15), p. 1583-1584, October 1989.

Kumagai, H. and M. Obara; "Theoretical and Experimental Study of KrF Fluorescence in a Multimicrosecond Longitudinal Discharge" *IEEE Trans. Plasma Sci.* **PS-16**(4), p. 453, 1988.

MacDonald, A.D.; *Microwave Breakdown in Gases.* New York: John Wiley & Sons, 1966.

Mangano, J.A. and J.H. Jacob; "Electron-beam controlled discharge pumping of the KrF laser" *Appl. Phys. Lett.* **27**(9). pp. 495-498, 1975.

Mansfeild, J.M.; M.P. Bratzel; H.O. Norgordon; D.O. Knapp, K.E. Zacha and J.D. Winefordner; "Experimental investigation of electrodeless discharge lamps as excitation sources for atomic fluorescence flame spectroscopy" *Spectrochimica Acta*, **23B**, pp. 389-402, 1968.

McDaniel, E.W. *Atomic collisions: Electron and Photon Projectiles.* New York: John Wiley & Sons, 1989.

Mikhkel'soo, V.T.; A.B. Treshchalov; V.E. Peet; E.Kh. Yalviste; A.A. Belokon'; B.I. Brainin and K.M. Khritov; "Formation of XeCl excimer molecules as a result of mixing gas streams excited by a continuous discharge" *Sov. J. Quantum Electron.* **17**(7), pp. 890-892, 1987.

Moisan, M.; C. Beaudrya and P. Leprince; "A Small Microwave Plasma Source for Long Column Production without Magnetic Field" *IEEE Trans. Plasma Sci.* **PS-3**(2), pp. 55-59, 1975.

Paik, S.F. and J.E. Creedon; "Microwave-Excited Ionized Argon Laser" *Proc. IEEE* **56**, pp. 2086-2087, 1968.

Parazzoli, C.G. and K. Chien; "Numerical Analysis of a CW RF Pumped CO_2 Waveguide Laser" *IEEE J. Quantum Electron.* **QE-12**(3), pp. 479-488, 1986.

Phillips, R.; *Sources and Applications of Ultraviolet Radiation*. London: Academic Press Inc. (London) Ltd, 1983.

Reintjes, J.F. and G.T. Coate *Principles of Radar*. Third Edition. New York: McGraw-Hill Book Company, 1952.

Rhodes, Ch.K. (Editor) *Excimer Lasers (Topics in Applied Physics, Volume 30)*. Second Edition. Berlin: Springer-Verlag, 1982.

Searles, S.K. and G.A. Hart; "Stimulated emission at 281.8 nm from XeBr" *Appl. Phys. Lett.* **27**(4), pp. 243-245, 1975.

Taylor, R.S. and K.E. Leopold; "Microsecond optical pulses from a UV-preionized XeCl Laser" *Appl. Phys. Lett.* **47**(2) pp. 81-83, 1985.

Vaulin, V.A.; V.I. Derzhiev; V.M. Lapin; V.N. Slinko; S.S. Sulakshin; S.I. Yakovlenko and A.M. Yancharina; "Neon-hydrogen plasma laser pumped by a microwave discharge" *Sov. J. Quantum Electron.* **19**(3), pp. 323-324, 1989.

Vaulin, V.A.; V.N. Slinko and S.S. Sulakshin; "Nitrogen laser excited by microwave pulses" *Sov. J. Quantum Electron.* **18**(1), pp. 38-39, 1988.

Verdeyen, J.T.; *Laser Electronics*. Englewood Cliffs, NJ: Prentice-Hall, 1981.

Watkin, J.E. and A.H. Misner; "Fluorescence and Crime Scenes in the 90s" *RCMP Gazette* **52**(9), pp. 1-5, 1990.

Wayne, R.P.; *Principles and Applications of Photochemistry*. Oxford: Oxford University Press, 1988.

Weast, R.C. (Editor-in-Chief); *CRC Handbook of Chemistry and Physics*. Boca Raton, FLA: CRC Press, 1986.

Webb, C; Private Communication, June 1990.

Wilkinson, P.G.; "New Krypton Light Source for the Vacuum Ultraviolet" *J. Opt. Soc. Am.* **45**(12), pp. 1044-1046, 1955.

Wilkinson, P.G. and Y. Tanaka: "New Xenon-Light Source for the Vacuum Ultraviolet" *J. Opt. Soc. Am.* **45**(5), pp. 344-349, 1955.

Wisoff, P.J.K.; A.J. Mendelsohn; S.E. Harris and J.F. Young; "Improved Performance of the Microwave-Pumped XeCl Laser" *IEEE J. Quantum Electron.* **QE-18**(11), pp. 1839-1840, 1982.

Wisoff, P.J.K.; and J.F. Young; "Active Mode Locking of the Microwave-Pumped XeCl Laser" *IEEE J. Quantum Electron.* **QE-20**(3), pp. 195-197, 1984.

Witteman, W.J.: *The CO_2 Laser*. Springer Series in Optical Science. Berlin: Springer-Verlag, 1987.

Yariv, A. *Optical Electronics*. Third Edition. New York: CBS College Publishing, 1985.